ERROR ANALYSIS AND CHARACTERIZATION OF PIEZORESISTIVE ARRAY TOUCH SENSORS

A Thesis Submitted to
the Graduate School of Engineering and Sciences of
İzmir Institute of Technology
in Partial Fulfillment of the Requirements for the Degree of

MASTER OF SCIENCE

in Mechanical Engineering

by
Mehmet Ogün SARP

September 2022
İZMİR

ACKNOWLEDGEMENTS

First of all, I would like to express my sincere appreciation and thanks to my academic advisor Assistant Professor Kerem ALTUN, who has always supported me through this challenging project. He is a distinguished advisor, mentor, and educator. He has helped me make decisions and navigate my research process with encouragements, and powerful suggestions. In addition, the information, and topics we learned in his ME591 course played a huge role in making this project happen.

I would also like to thank Prof. Serhan ÖZDEMİR. Throughout this long and arduous scientific journey, he was a pillar of great support. The information in the ME587 course I received from him has been another important milestone in the realization of this project. Additionally, he accepted this thesis project as a term project for ME578, another course I took from him, and in a short amount of time made a significant contribution to my master's thesis.

I would also like to thank the other instructors with whom I took classes during my master's degree. I would also like to thank the workshop supervisors, Murat MİRZA and Sedat ÇELİK, for their support of equipment and assistance in making the desired and necessary components for my project.

I would like to extend my special thanks to Irmak EGE, who helped me in learning "Python" and "MATLAB" softwares and contributed a lot to my thesis thanks to his analytical thinking ability. His willingness to share his knowledge and experience is massive. I would also like to express my gratitude to Muhammed Emin ÖZDEMİR for his friendship and creative ideas during this difficult and challenging period.

Finally, I would like to express my gratitude to my wife, Buse, and my 10-month-old son, Kayra, whom I left alone a lot during this process and could not take care of much. They consistently provided emotional support and avoided showing me the challenges they were suffering. I hope that this work will provide our family with much greater opportunities in the future.

To my beloved wife and son

ABSTRACT

ERROR ANALYSIS AND CHARACTERIZATION OF PIEZORESISTIVE ARRAY TOUCH SENSORS

Numerous investigations and academic studies employ piezoresistive types of sensors. One of the main foundations of this thesis is to contribute to the literature by making a detailed error analysis and by proposing a new error reduction. In this thesis, piezoresistive touch sensors are designed and manufactured from scratch in accordance with the working principle of commercially available sensors. This thesis examines two different sensor configurations for single-touch applications. On these sensors, three different loads are tested statically with the same 61 test points located on the sensor, a single load at a time, and their Center of Pressure results are examined and compared to each other. As a result, it is observed that the 7x7 sensor array gives more successful results than the 5x5 sensor array at the same test points. Kadane's algorithm is introduced and implemented in experiments aimed to reduce the error values. As a result, success is achieved. Furthermore, with another proposed method, circle fitting, the centers of the theoretical circle formed by measurements are found, and it is examined whether the sensor measurements were considered as homogeneous. In other words, in each case, the levels of decentralization did not vary much. Finally, the multivariate linear regression method is examined through the system equations obtained from the randomly selected measurement points. It is seen that both the sensor outputs of the other points on the system can be predicted and the error metrics on the system can be reduced.

Keywords: *Center Of Pressure; Pressure Sensor Array; Velostat™; Piezoresistive Sensors; Tactile Sensors; Error Measurement; Error Reduction*

ÖZET

PİEZODİRENÇLİ SIRA DİZİLİMLİ DOKUNMA ALGILAYICILARININ HATA ANALİZİ VE KARAKTERİZASYONU

Çok sayıda araştırma ve akademik çalışma, piezorezistif sensör türlerini içermektedir. Bu tezin temel dayanaklarından biri, detaylı bir hata analizi yaparak ve yeni bir hata azaltma önerisinde bulunarak literatüre katkıda bulunmaktır. Bu tezde, piezorezistif dokunmatik sensörler, piyasada bulunan sensörlerin çalışma prensibine uygun olarak sıfırdan tasarlanmış ve üretilmiştir. Bu tez, tek dokunuşlu uygulamalar için iki farklı sensör konfigürasyonunu incelemektedir. Bu sensörlerde, sensör üzerinde bulunan aynı 61 test noktası, bir seferde tek bir yük olmak üzere toplamda üç farklı yük altında statik olarak test edilmiş, bu noktaların basınç merkezi sonuçları incelenmiş ve birbirleriyle karşılaştırılmıştır. Sonuç olarak 7x7 sensör dizisinin aynı test noktalarında 5x5 sensör dizisinden daha başarılı sonuçlar verdiği gözlemlenmektedir. Kadane algoritması, sensörlerdeki hata değerlerini azaltma amacıyla deney verilerine uygulanmıştır. Sonuç olarak, başarı elde edilmiştir ve hataların azaldığı gözlemlenmiştir. Ayrıca önerilen bir başka yöntem olan daire uydurma ile ölçümlerle oluşan teorik çemberin merkezleri bulunarak sensör ölçümlerinin homojen olarak kabul edilip edilmediği incelenir. Başka bir deyişle, her durumda, merkezden kaçıklık seviyelerinin çok fazla değişmediği deneyimlenmiştir. Son olarak, rastgele seçilen ölçüm noktalarından elde edilen sistem denklemleri üzerinden çok değişkenli doğrusal regresyon yöntemi incelenmiştir. Hem sistem üzerindeki diğer noktaların sensör çıkışlarının tahmin edilebildiği hem de sistem üzerindeki hata metriklerinin azaltılabildiği görülmektedir.

Anahtar Kelimeler: *Basınç Merkezi; Basınç Sensör Dizisi; Velostat™; Piezorezistif Sensörler; Dokunsal Sensörler; Hata Ölçümü; Hata Azaltma*

LIST OF ABBREVIATIONS

PRTS	–	Piezoresistive tactile/touch Sensor
Sensel	–	One of the pressure sensors in a matrix shaped sensor
COP_x	–	Center of pressure in x direction
COP_y	–	Center of pressure in y direction
RMSE	–	Root mean square error
MLR	–	Multivariate linear regression
FSR	–	Force sensitive resistor
ADC	–	Analog to digital converter
MCU	–	Microcontroller unit
PVDF	–	Polyvinylidene fluoride
UI	–	User interface
Std Dev	–	Standart deviation
PPI	–	Pixels per inch

TABLE OF CONTENTS

LIST OF FIGURES

Figure **Page**

Figure **Page**

Figure **Page**

Figure **Page**

LIST OF TABLES

Table **Page**

CHAPTER 1

INTRODUCTION

A tactile sensor (aka touch sensor) is an electronic device that measures information received from physically interacting with its environment [1] as shown in Figure 1.1. There are tactile sensors in robots, computer hardware, security systems and medical measurement sector. Touchscreen devices on mobile phones and computers are a frequent application of tactile sensors. The design of these sensors is based on the biological sense of cutaneous touch, which can detect stimuli from mechanical stimulation, temperature, and pain. A tactile sensor will detect and respond to a force or physical contact signal. It should be a single-point contact, but the sensing area can be any size; if the sensor is small, it can be utilized in a variety of locations. Generally, pressure sensors fall into two categories: active and passive. Piezoresistive type tactile sensors were utilized in this thesis. Unlike passive piezoelectric sensors, which generate electrical signals when mechanically stimulated, piezoresistive sensors are active sensors and need to be supplied with an external voltage [2]. When a force is applied to a force detecting resistor, it doesn't provide any signal on its own, but by attaching it to an electrical circuit, resistance variations can be measured.

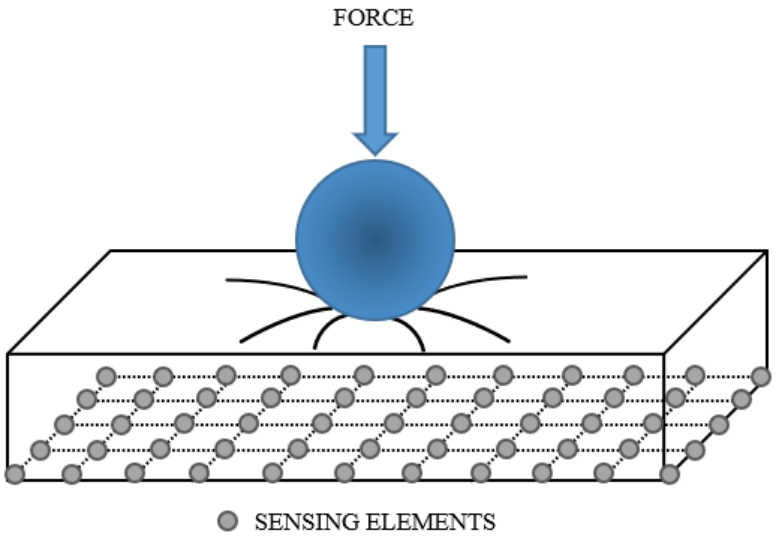

Figure 1.1. General tactile interaction [1]

In this thesis, the types of touch sensors are mentioned in Chapter 1, and brief information is given about the studies using different types of sensors in the literature. The advantages and disadvantages of sensors of different types and technologies compared to each other are shared. Then, detailed information about the studies on piezoresistive sensors, which is the subject of study of this thesis, is presented. In addition to these, the scope of this thesis and the motivation that led to the study are explained. In Chapter 2, the working principles of "Piezoresistive Touch Sensors" are explained in detail. Comprehensive information about the design of the sensors, the materials used for the construction of the sensors, the electronic circuit characteristics of the sensors, and the data communication of the sensors are provided. In Chapter 3, the methods used in the thesis are presented comprehensively with examples. First, information is given about how and through which programs the data received from the sensor and the analysis to be applied to this data are performed. Then, the approach in this thesis is shared based on the studies in the literature on the magnitude of the force applied by the human finger and the determination of the application area. After the force type and weight are determined, sensor design information, dimensions, etc. specific to this force are presented in detail. Then, the selection of the bias resistor, one of the most important issues in sensor design, is also determined by means of experimental measurements. After the sensor design and manufacturing, information is given about the COP calculations to be used in sensor analysis and the various error reduction algorithms presented in this thesis. In this thesis and study, a new error reduction method that is unique in the literature and are very simple to apply are proposed. Moreover, in this section, multivariate linear regression and circular regression methods applied to the data obtained from the sensor are mentioned in detail. In Chapter 4, the results of all the analysis and tests of two different meshed sensors under three different weights in this thesis are presented in detail. Detailed comparison results of sensor arrays with two different configurations (with different numbers of sensors(sensels) in the same area) in terms of performance are also shared. In addition, the results of the a new error reduction method proposed in the thesis are presented comparatively. Finally, in Chapter 5, topics such as the achievements related to the thesis, the experiences gained, and what kind of studies can be done in the future are discussed.

1.1. Literature Review

Tactile sensors are transducers or data-collecting devices designed to detect a variety of qualities by direct physical contact [3]. Various technologies, some of which are directly influenced by studies on biological touch, are utilized in the creation of tactile sensors. The expansion of robotic applications in healthcare, agriculture, social support, autonomous systems, and unstructured environments has led to the development of very sensitive touch sensors. Their deployment plays a crucial role in enabling the detection, measurement, and conversion of information gained via physical interaction with objects into a form suitable for processing and analysis by higher-level modules within an intelligent system [4]. Although tactile sensor technology has made significant design and capability improvements in recent decades, tactile sensing systems are still relatively immature in comparison to the sophisticated technology achieved in vision [5]. It is likely that the inherent complexity of the sense of touch has contributed to the comparatively modest evolution thus far [6]. Another restriction is that tactile sensors, by their very nature, require direct contact with surfaces and objects, making them more susceptible to wear and damage than other sensor categories.

Sensors in human tactile sensing systems are classified by the type of measured data recorded and the method by which they are obtained. For instance, tactile sensors can respond to static or dynamic forces and could be used for both proprioception or exteroception [7]. Proprioceptive sensors measure the internal state of a system, such as joint angles, limb locations, velocity, and motor torque. Exteroceptive sensors assess the physical contact features of objects in the environment, including sensor surface deformation, contact area, and pressure readings [6]. Classification of tactile sensor technologies is based on the transduction mechanism used to turn external sensations into a suitable form for an efficient system [8]. Following are descriptions of the most extensively used touch sensor technologies in robotics, which are based on capacitive, piezoresistive, optical, magnetic, and piezoelectric transduction methods.

1.1.1. Tactile Sensor Types

In this section, the types of touch sensors are mentioned and brief information is given about the studies using different types of sensors in the literature.

1.1.1.1. Capacitive Sensors

Tactile sensors based on capacitive transduction measure the changes in capacitance caused by an applied load over a parallel plate capacitor (Figure 1.2). The capacitance is proportional to the spacing and volume of the parallel plate capacitor, which incorporates a flexible elastomeric separator. While Harmon has emphasized that capacitive sensors are susceptible to external fields [9], this sensor technology has gained popularity in robotics for the construction of "taxels" that replicate parts of human fingers' mechanoreception [10, 11]. Capacitive sensors can be manufactured in extremely small dimensions, enabling their creation and integration into dense arrays in confined areas, such as palms and fingertips [12]. These features, as well as the low temperature sensitivity, low power consumption, and the ability to detect normal or tangential forces presented by this technology, make it an excellent choice for many different types of applications [13]. Hysteresis is considered to be a serious limitation in these types of sensors.

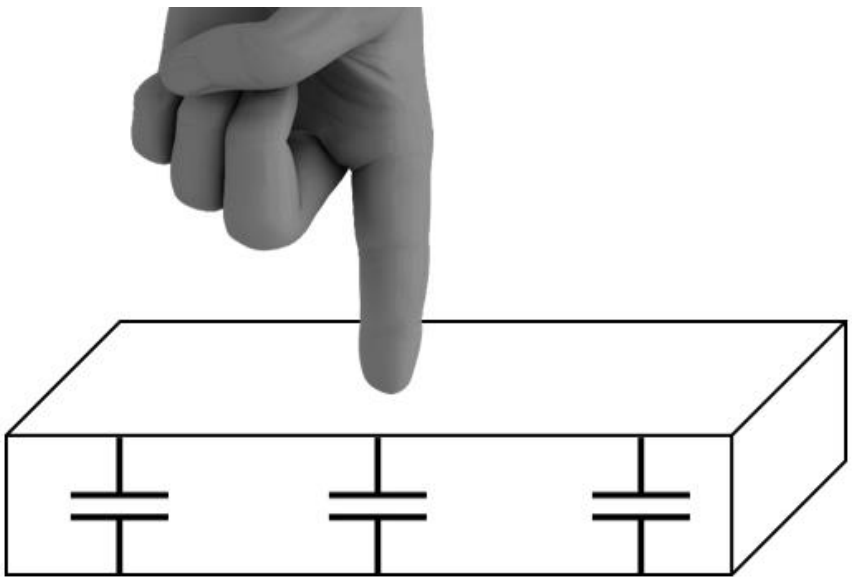

Figure 1.2. Capacitive interaction

1.1.1.2. Piezoresistive Sensors

This method of transduction monitors changes in the contact's resistance when load is exerted (Figure 1.3). Typically, piezoresistive sensors are constructed from conductive rubber or piezoresistive ink and stamped with a pattern. When no contact or tension is applied to the sensor, its resistance reaches its maximum value. In contrast, as contact pressure or stress increases, resistance decreases [14]. [15, 16], and Russell were the first to illustrate the advantages of this transduction technique for sensor array integration [17]. This technology's benefits include a large dynamic range, durability, good overload tolerance, low cost, and the ability to be manufactured in extremely small sizes. Limited spatial resolution, the difficulty of independently connecting many sensor units, drift and hysteresis are disadvantages. Fabric-based piezoresistive sensors have been created as an alternate material to increase endurance and decrease hysteresis thanks to research and development [6]. Numerous robotic applications have employed piezoresistive tactile sensors, particularly where high precision is not a design requirement [18-20]. In comparison to touch sensors based on other physical effects (such as piezoelectric, capacitive, optical, and magnetic), piezoresistive tactile sensors offer high sensitivity, planar device design, outstanding versatility, and simple circuitry.

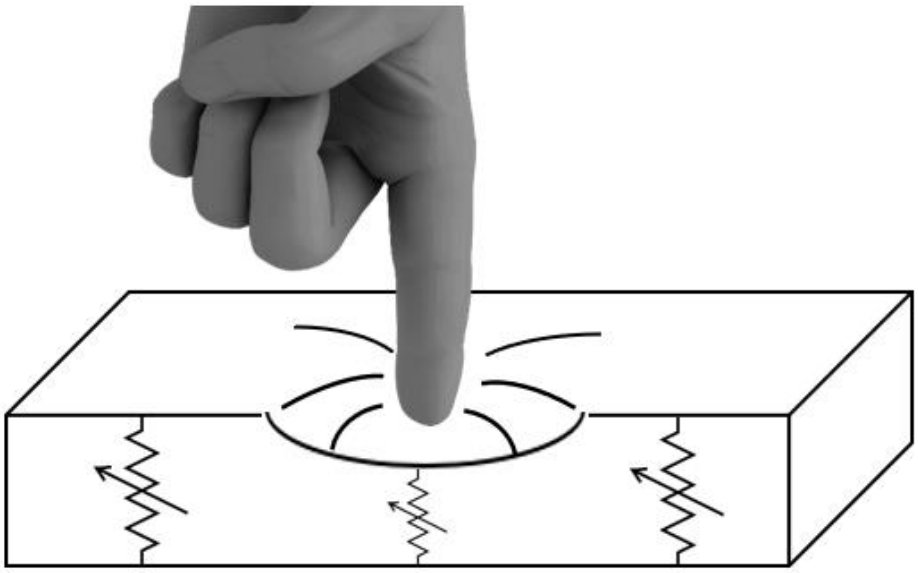

Figure 1.3. Piezoresistive interaction

1.1.1.3. Optical Sensors

Optical sensors function by converting mechanical contact, pressure, or directional motion into alterations in light intensity or refractive index that are subsequently detected by cutting-edge vision sensors (Figure 1.4). The requirement to include light emitters and detectors (such as CCD arrays) results in greater size. Optical sensors, on the other hand, are appealing because of their potential for high spatial resolution, resistance to electrical interference, light weight, and ability to alleviate the wiring complexity issue posed by other sensor types, such as capacitive and piezoresistive [3, 21]. Consequently, optical tactile sensors have been integrated into many robotic systems. Begej [22] presented a robotic system for examining dexterous item manipulation that incorporated two 32x32 flat sensor arrays constructed from optical fibers. Using an optical fingertip that measures the intensity and direction of reflected light, Yamada [23] describes sub-millimeter resolution for object contact and location identification. Heo et al. discuss the construction of optical taxels that are able to monitor normal forces [24]. This optical system utilizes an LED emitter in conjunction with a CCD array to measure changes in light intensity caused by force. As a last illustration, Hsiao et al. [25] present an optical system for dependable sensing of body touch and gripping in a three-fingered robot hand.

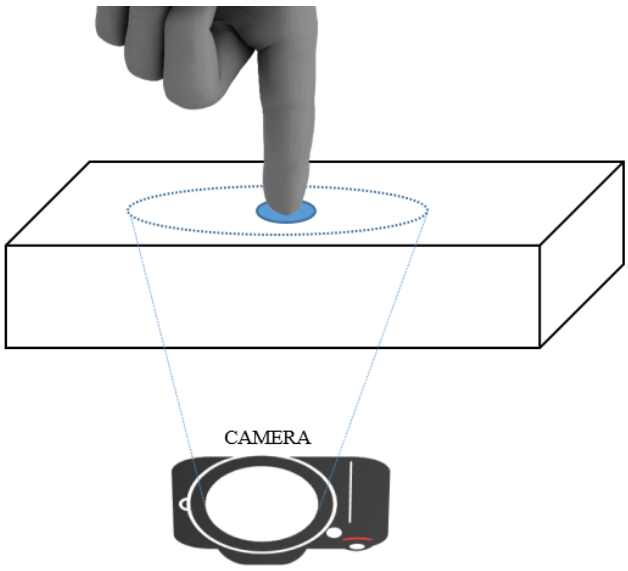

Figure 1.4. Optical sensor functioning

1.1.1.4. Magnetic Sensors

This technique operates by using Hall effect, magnetoresistive, or magnetoelastic sensors to detect changes in magnetic flux generated by an applied force (Figure 1.5). Hall effect sensors measure fluctuations in the voltage produced by an electric current traveling through a conductive substance submerged in a magnetic field [4]. In Kinoshita et al. [26], a robot gripper utilizing this sensing technique was coupled with twenty sensing elements to enable the robot to conduct an experiment on object tracking. Nowlin researched touch recognition and fingertip deformation using a 4x4 array of Hall effect sensors affixed to a stiff platform [27]. Hall effect sensors have been proven efficient for sensing the multidirectional deformations of an artificial whisker [28, 29]. Magnetoresistive and magnetoelastic sensors can detect differences in magnetic fields resulting from the application of mechanical stress. In the 1970s, a robot tactile sensor employing this magnetic method was created for contour-based classification of objects [30]. Despite the comparatively high number of magnetic sensing devices, Jayawant [31] was able to recognize 2D images utilizing a 256-element magnetic sensor array. The benefits of magnetic sensing devices include high sensitivity, a broad dynamic range, very low hysteresis, linear response, and overall resilience. They, however, are prone to magnetic noise and interference. Applications are constrained by the sensor device's physical size and its inability to work in magnetic settings [32].

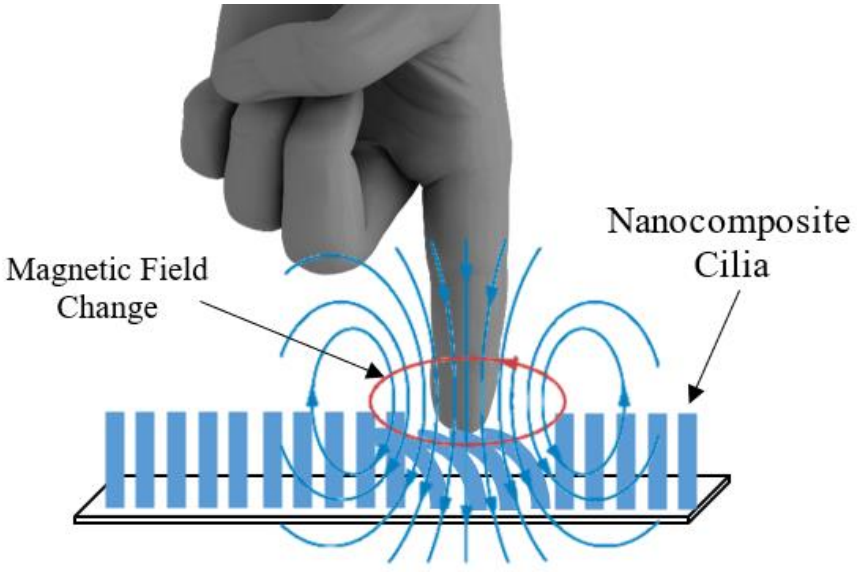

Figure 1.5. Magnetic sensor functioning

1.1.1.5. Piezoelectric Sensors

Piezoelectric sensors generate an electric charge according to the force, deformation, or pressure applied (Figure 1.6). This sensor technology's primary limitations are its restriction to dynamic measurements and sensitivity to temperature. Due to their sensitivity, high frequency response, and availability in a variety of materials, such as plastics, crystals, ceramics, and polyvinylidene fluoride (PVDF), however, they are well-suited for measuring vibrations and are commonly employed [5, 10]. Grahn and Astle [33] accomplished robust object detection by covering a touch sensor with a piezoelectric material based on a sheet of silicon rubber. In this instance, the electric charge employed for object classification was created by touching and deforming a silicon layer. Yamada and Cutkosky [34] created an artificial skin that was sensitive to force, vibration, and sliding using piezoelectric technology. Due to its flexibility and high chemical stability, PVDF is the piezoelectric material most typically used in the manufacture of touch sensors [32]. Dario and De Rossi [35] discuss the use of polyvinylidene fluoride (PVDF) in the construction and integration of touch sensors in a robotic hand.

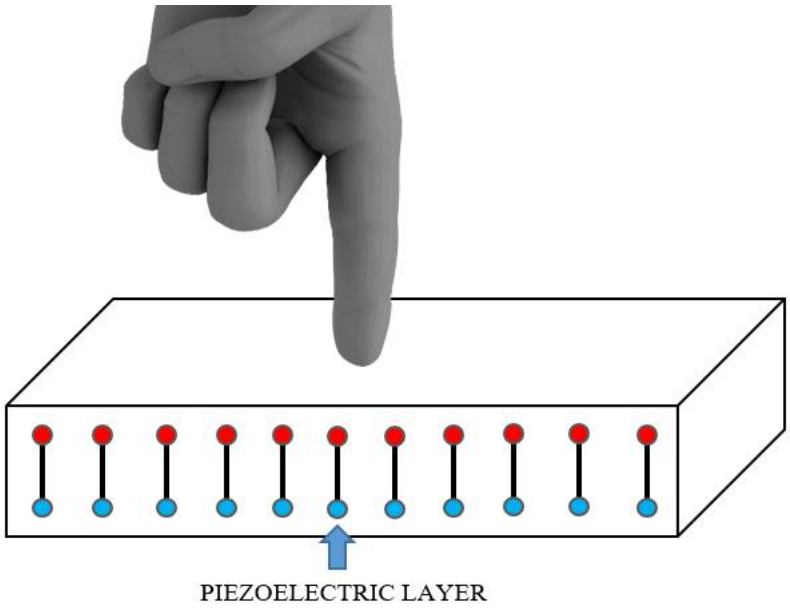

Figure 1.6. Piezoelectric sensor functioning

1.1.2. Comparison of Tactile Sensor Types

Sensors in human tactile sensing systems are categorized based on the type of measured data acquired and the manner of data collection. Different tactile sensor types have their own pros and cons as mentioned in Sections 1.1.1.1-5. In summary, the advantages and disadvantages of tactile sensors with different technologies are presented in Table 1.1.

Table 1.1. Comparison of different tactile sensor technologies

Sensor Type	Advantages	Disadvantages
Capacitive Sensors	Limited hysteresis High stability High sensitivity Low power consumption	High cost Complex circuitry Poor flexibility
Piezoresistive Sensors	Low cost Easy fabrication Excellent flexibility Highly scalable Easy circuitry	Hysteresis Lower resolution Signal drift Material ageing
Optical Sensors	No hysteresis High sensitivity Multi-directional sensing	Susceptible to misalignment Limited flexibility
Magnetic Sensors	Wireless operation Low power consumption Simple fabrication	Sensitive to environment Limited materials Magnetic noise
Piezoelectric Sensors	High bandwidth High power density No additional power supply	Temperature dependent Charge leakages Signal drift in static forces

1.1.3. Piezoresistive Sensor Studies

In comparison to other types of sensors, the greatest advantages of piezoresistive sensors are their low production cost, simplicity of interfacing circuits, and straightforward data collecting method. Consequently, numerous investigations and academic studies employ this type of sensors. Bibliographical sources of such researches and comparing studies based on piezoresistive sensors for different sensing needs are provided kronologically in the Table 1.2. In this table, summary information about the year, materials used, sensor design and purpose of the study is given.

Table 1.2. Researches using pizeoresistive sensors

Year	Piezoresistive Material	Conductive Electrode Material	Sensor Design	Study Purpose	Reference
2022	Velostat™	Copper	Matrix 5 × 5 & 7 x 7 sensel	Position Accuracy	This thesis
2021	Velostat™	Copper	Matrix 16 × 9 sensel	Posture recognition	[36]
2021	Velostat™	Copper	Matrix 4 × 4 sensel	Position Accuracy	[37]
2020	Velostat™	Copper	Single point	Force measurement (0–3 N)	[38]
2019	Polyurethane film	Aluminum foil	Single point	Pressure measurement (0–650 kPa)	[39]
2019	Resistive ink	Conductive fabric	Matrix 17 × 10 sensel	Pressure measurement (2.5–640 kPa)	[40]
2019	Velostat™	Copper	Matrix 64× 64 sensel	Force measurement (0–3 N)	[41]
2018	Polyethylene Terapthalate	Conductive fabric	Single point	Pressure measurement (1–10 kPa)	[42]
2018	Velostat™	Conductive fabric	Single point	Force measurement (2–210 N)	[43]
2018	Resistive ink	Silver	Matrix 4 × 4 sensel	Pressure measurement (2.5–640 kPa)	[44]
2017	Velostat™	Copper	Matrix 16 × 10 sensel	Force measurement (0–500 N)	[45]

(cont. on next page)

Table 1.2. (cont.)

2017	Polyethylene Terapthalate	Silver	Matrix 16 sensels	Force measurement (0–53 N)	[46]
2017	Velostat™	Conductive fabric	Matrix 32 × 32 sensel	Force measurement (0–16 N)	[47]
2017	Resistive ink	Conductive fabric	Matrix 20 × 20 sensel	Gesture recognition	[48]
2016	Velostat™	Copper	Single point	Pressure measurement (0–2.7 kPa)	[49]
2015	Velostat™	Silver-covered material	Single point	Pressure measurement (0–1000 kPa)	[50]
2015	Velostat™	Aluminum foil	Matrix 2 × 8 sensel	Posture recognition, (0–3.9 kPa)	[51]
2015	Velostat™	Copper	Matrix 3 × 3 sensel	Posture analysis	[52]
2015	Velostat™	Conductive fabric	Single point	Compressive and stretching forces	[53]
2014	Velostat™	Copper	Matrix 48 × 48 sensel	Gesture recognition	[54]
2014	Velostat™	Copper	Single point	Pressure measurement (0–250 kPa)	[55]
2014	Velostat™	Conductive fabric	Matrix 4 × 4 sensel	Force measurement (4–60 N)	[56]
2014	Graphene nanoplatelets and carbon nanotubes	Silver	Matrix	Pressure measurement (0–100000 kPa)	[57]
2013	Velostat™	Conductive fabric	Single point	Force measurement (0–20 N)	[58]
2012	Velostat™	Copper	Single point	Force measurement (0–5 N)	[59]
2011	Velostat™	Conductive fabric	Matrix 64 sensel	Pressure measurement map	[60]
2011	Velostat™	Conductive fabric	Single point	Event (impact) detection	[61]
2011	Velostat™	Conductive fabric	Matrix	Gesture recognition	[62]
2001	Velostat™	Copper	Matrix 8 × 8 sensel	Pressure measurement (0–500 kPa)	[63]

1.2. Motivation and Objectives

Everything we use in our daily lives becomes intelligent as technology improves. Furthermore, there are numerous ways to interact with these intelligent devices today. Work is also underway on artificial skin applications to interact with machines and robots. With the progress of robotics research, it is anticipated that more intelligent robots will replace humans in a variety of complex tasks. In unstructured situations, robots are liable to interact with objects or humans. A tactile sensor is capable of detecting changes in the environment and can receive real-time contact information, allowing robots to avoid collisions or communicate with humans in the environment. In addition, thanks to the constant improvement of technological components, touch control is now possible on all types of materials, including fabrics and other flexible materials. Therefore, in recent years, tactile sensors have attracted the interest of numerous researchers throughout the world. There are also very expensive, complex, and various sensor products available on the market used for many applications, such as medical measurements of various human parts. For example, balance deficits and postural instability induced by impairments such as stroke or diseases such as Parkinson's disease have been examined using these types of sensors. They can also be used to assess the efficacy of treatments, such as osteoarthritis surgery. Other applications of piezoresistive sensor measurements include assessing the postural and balance control of amputees. In each of these applications, measurement accuracy is essential since the data is utilized to diagnose or treat patients.

As can be seen in Section 1.1.3, such sensors are the subject of many studies in the literature. In addition, piezoresistive sensor studies have gained momentum in recent years with the developing technology and their number is increasing day by day. When the studies in the literature using such sensors were examined, it was seen that many studies were with force measurement, pressure measurement, gesture recognition, and posture recognition. There have been only one study measuring the position sensitivity of such sensors and performing error analysis [37]. One of the main foundations of this thesis is to contribute to the literature by making a more detailed analysis than the analyzes in this study and by proposing a simple new error reduction method that is unique in the literature.

This thesis mainly comprises the following goals:

- Design and build a tactile sensor suitable for detecting forces similar to those applied by human fingers and fingertip sizes.
- Measure and test the performance characteristics of the sensor on a flat surface for static position accuracy.
- Compare the performance of different meshed sensors.
- Check for the methods for the improvement of process and error reduction.
- Check for the methods for error prediction in the sensor system.

1.3. Scope

In this thesis, piezoresistive touch sensors are designed and manufactured from scratch in accordance with the working principle of commercially available piezoresistive touch sensors. Position sensitivities are measured, and improvement methods are examined. Also, a new and simple improvement method is introduced compared to the complex solutions that are present in the literature studies. In the sensor designs, 10 mm copper bands are used, and electrodes are formed by lining up in a certain pattern on acetate paper covering a planar area of 60 mm x 60 mm. 50 g, 100 g, and 150 g are selected as loads similar to those exerted by human fingertips. These three different loads are tested statically with the same 61 points located on the sensor, a single load at a time, and their results are examined. The sensor contact area (diameter) of the loads is selected as 9 mm, again related to the touch target studies in the literature. This thesis is limited to two different configurations for single-touch applications. The first sensor used in these experiments has a 5x5 (25 sensels) sensor array and the other has a 7x7 (49 sensels) sensor array. Every parameter is the same except the sensel numbers, so that the effect of the number or sensels can be examined. A sensel is a single sensor element of an array of sensors.

CHAPTER 2

PIEZORESISTIVE SENSOR PROPERTIES

The functioning principles of "Piezoresistive Touch Sensors" are explained in detail in this chapter. Morover, comprehensive information is supplied regarding the design of the sensors, the materials necessary for their construction, the electronic circuit characteristics, and the data communication of the sensors.

2.1. Force Sensitive Resistor (FSR) Principles

In this section , the features of the piezoresistive tactile sensors (PRTS) to be used in the experiments are explained. Sensor construction with the same working principle as piezoresistive sensors sold as commercial products in the market is shared with all its details. This chapter and the next discuss design processes, required materials, and the operation of the design, explaining why certain components were chosen and how they contribute to the design as a whole. This section also details the necessary instrumentation for powering and operating PRTSs.

First of all, it is very important to know the method of operation and characteristics of the sensors "FSR". Piezoresistive sensors and sensor arrays operate on "FSR" logic. The technology used in FSRs has been patented by Interlink Electronics, which has been in operation since 1985. Force-sensitive resistors (FSRs) are variable resistors with two legs whose resistance decreases as the applied force increases. FSRs can vary in size, shape, and sensitivity to force sensing. There are numerous shape variations, including square and circular (the active sensor area). FSRs are sensors that allow you to detect physical pressure, squeezing, and weight. They are simple to use and have a low cost. Between two thin substrates, force sensing resistors include a semi-conductive substance, or semi-conductive ink. As depicted in Figure 2.1, there are two distinct technologies for force sensing resistors: Shunt Mode and Thru Mode [94]. Shunt mode force sensing resistors are thick-film polymer devices with two membranes separated by a narrow air gap. The first membrane has two sets of interdigitated traces that are electrically isolated

from one another, while the second membrane is coated with a particular textured, resistive ink. Through mode force sensing resistors are flexible printed circuits whose two outer substrates are polyester film. Above and below a pressure-sensitive layer are silver circles with traces, followed by a conductive polymer. A layer of glue is utilized to laminate the two substrate layers together.

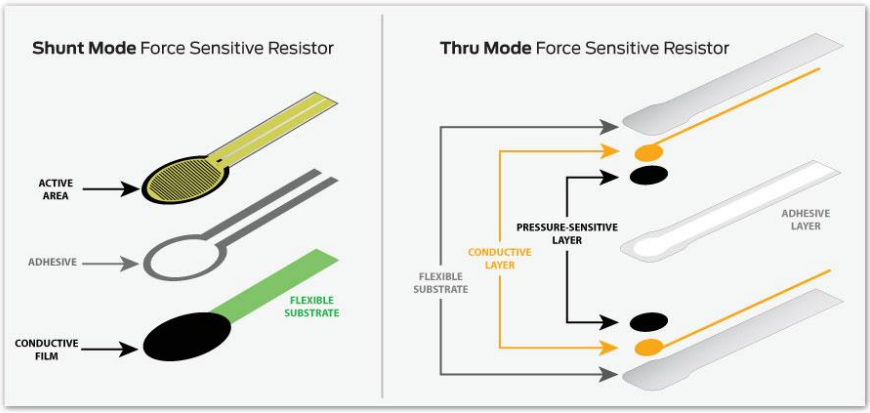

Figure 2.1. FSR types [94]

FSRs are essentially resistors whose resistance value (in Ohms) varies with the amount of pressure applied. These sensors are relatively inexpensive and simple to operate, but they are rarely precise. They vary somewhat from sensor to sensor, perhaps 10%. Consequently, while using FSRs, you should only anticipate response ranges. Although FSRs can sense weight, they are not ideal for determining the actual loads carried and they are not precision measuring equipment like load cells or strain gauges.

2.1.1. FSR Applications

FSRs can be used various number of example applications, including:

- Detecting human interaction. Sense whether a touch is accidental or intentional by a reading force (or other signal processing)
- Using force for UI feedback. Detect user's touch force to make a more intuitive interface
- Finding centroid of force. Use multiple sensors to determine centroid of force
- Detecting presence, position, or motion. Sense a person/patient in a bed, chair, or medical device

2.1.2. How a FSR Works

The FSR's resistance changes as more pressure is applied. When there is no pressure, the sensor looks like an infinite resistor (open circuit). As the pressure increases, the resistance goes down (Figure 2.2).

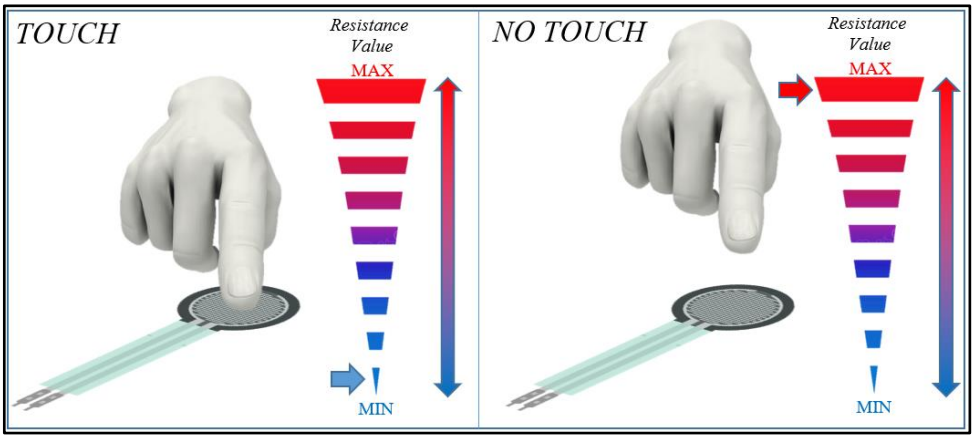

Figure 2.2. FSR working principle

Figure 2.3 displays the resistance vs force curve for the FSR 402 sensor [95]. Note that the data is plotted on logarithmic scales. It can be seen that the response is not linear. As you can see, there is a huge drop in resistance when a small amount of pressure is applied. After that, the resistance is inversely proportional to the applied force. At around 10 kg (not shown in the graph), the sensor is saturated and an increase in force yields little to no decrease in resistance.

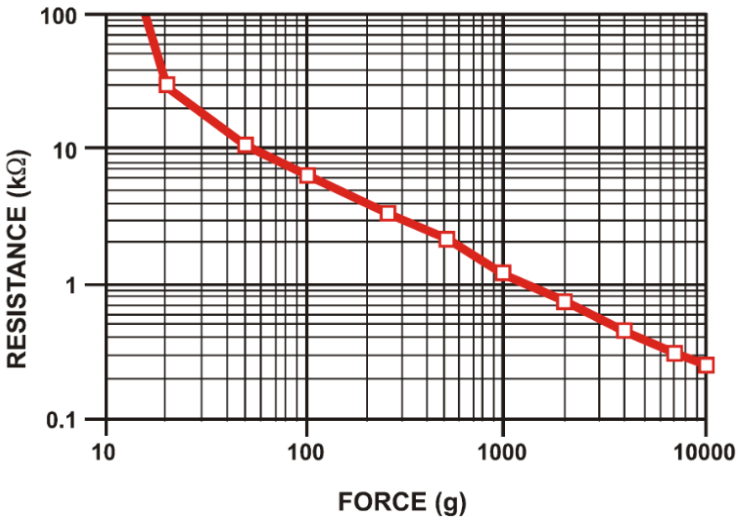

Figure 2.3. FSR resistance change [95]

2.1.3. Reading a FSR Sensor

As has been said before, FSRs are just variable resistors, so they are easy to use and only need simple circuitry to support them. The easiest way to read the FSR is to connect the FSR with a fixed value resistor or bias resistor (usually 10 kΩ) to create a voltage divider (Figure 2.4). This value should chosen in accordance with the internal resistance value of the FSR. To do this, one should connect one end of the FSR to power and the other to a pull-down resistor. Then the point between the fixed value pull-down resistor and the variable FSR resistor is connected to the ADC input of a microcontroller. Vcc is usually either 3.3 V or 5 V, depending on how much voltage the microcontroller can send out.

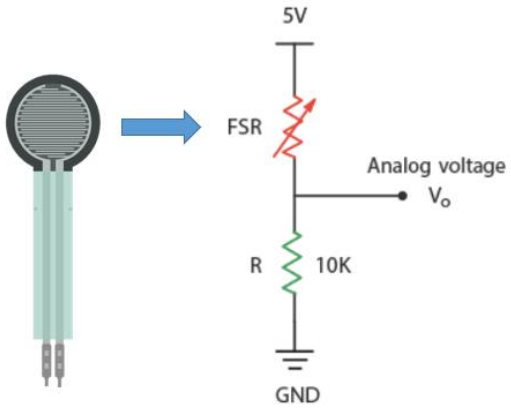

Figure 2.4. Voltage divider schema

It should be noted that the measured output voltage represents the voltage drop throughout the pull-down resistor and not across the FSR. The following equation describes the output of the voltage divider arrangement:

$$V_o = V_{cc}\, x\, \frac{R}{R + R_{FSR}} \tag{2.1}$$

When no pressure is present, the FSR resistance is quite high (about 10 MOhm). This yields the resulting output voltage:

$$V_o = 5\, x\, \frac{10kOhm}{10kOhm + 10MOhm} = 0.005V \approx 0V$$

Inversely, when pressure is present, the FSR resistance starts to decrease. If one presses too hard, the resistance of the FSR will be approximately 250 Ohm. This will yield the resulting output voltage:

$$V_o = 5\ x\ \frac{10kOhm}{10kOhm + 250Ohm} = 4.9V\ \approx 5V$$

As can be seen in the Table 2.1, the output voltage ranges from 0 to 5V based on the load exerted on the sensor. The table below illustrates the approximate analog voltage depending on the force/resistance of the sensor with a 5 V supply and a 10 K pulldown resistor.

Table 2.1. Resistance change based on the load [95]

Force (g)	**Force (N)**	**FSR Resistance**	**Voltage Output**
None	None	Infinitely High	0V
20.4	0.2	30KΩ	1.3V
50.9	0.5	12KΩ	2.5V
101.2	1	6KΩ	3.1V
1019.7	10	1KΩ	4.5V
10197	100	250Ω	4.9V
Infinitely High	Infinitely High	0Ω	5V

Circuitry for a single FSR sensor can be seen in Figure 2.5. Because a single FSR sensor has two connection legs, it takes up two pins in the MCU.

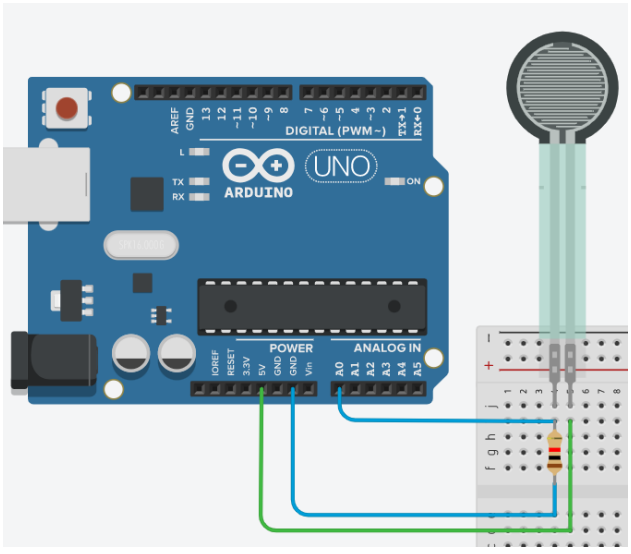

Figure 2.5. FSR connection to a MCU

FSR sensors come in a wide range of shapes and sizes, as can be seen in Figure 2.6.

Figure 2.6. Different shapes of FSRs

If more FSRs are needed for special tasks or applications, more can be used than a single sensor as depicted in Figure 2.7. In other words, since a single FSR sensor is not capable of detecting multi-inputs, an array of sensors is a must for multi-touch applications.

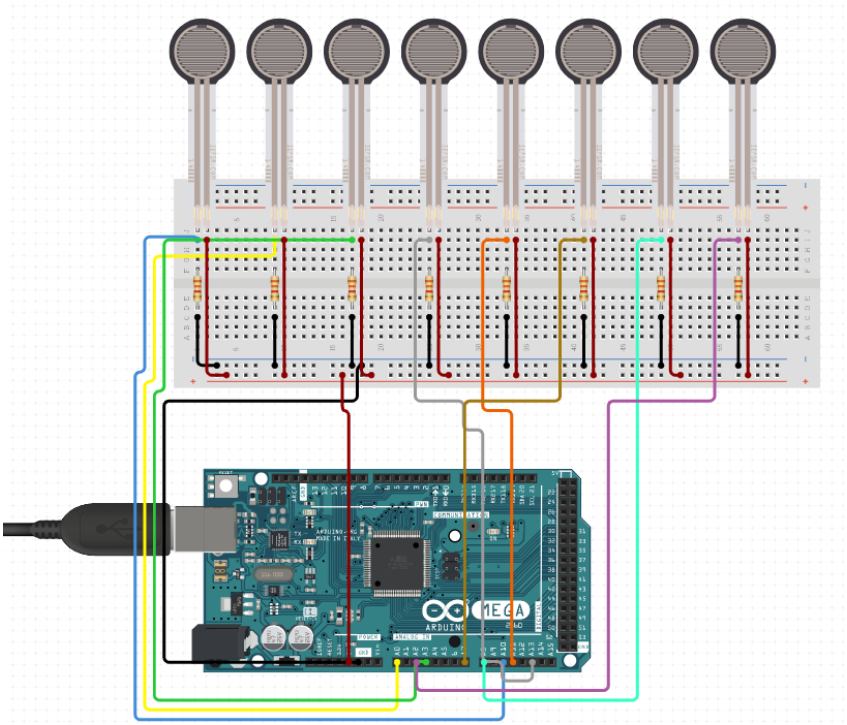

Figure 2.7. Multiple FSRs for sensor arrays

2.2. Sensor Structure and Materials

A FSR sensor array is a set of pressure sensors, often arranged in a certain geometric pattern, that are used to record pressure signals in a region. A FSR sensor array has the advantage over a single sensor in that it may offer pressure information for a region with a greater resolution and pressure sensor arrays are frequently utilized today.

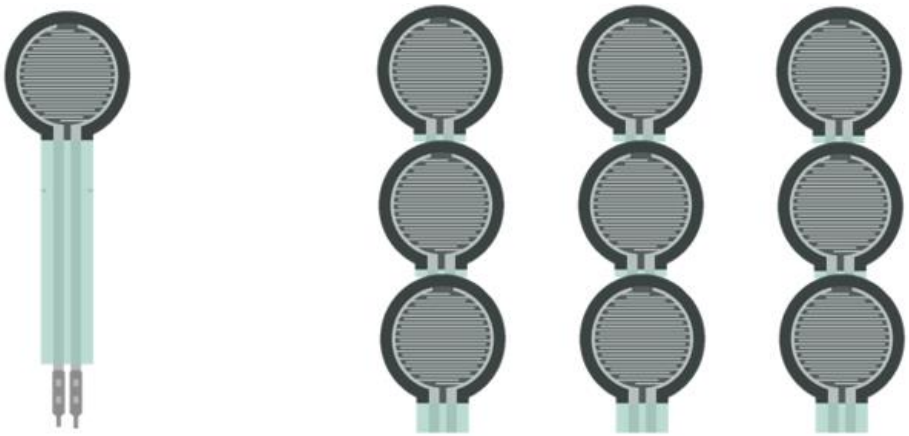

(a) (b)

Figure 2.8. (a) Single sensor and (b) multi-input sensor array

Multiple identical resistive sensing components, when joined (often in two-dimensional array configurations), form patterns based on the parameter variation detected over the array. This pattern design is used in numerous applications. By increasing the size of the array, the resolution of this data is improved. Accessing all array items for data collection and signal processing places size constraints on arrays. In general, access to all sensing devices requires two physical connections from each sensor, for a total of two NM connections in NxM style arrays, where N is the number of rows and M is the number of columns. When required on-chip linking metal lines and the number of bonding/probing pads are accounted for, this figure becomes significant for even a modest array. With the row–column configuration of these technologies' 2-D networked resistive circuits, the interconnect line count of NxM resistive sensor arrays was decreased to N + M from 2NM by key matrix methodology [63, 69]. Nonetheless, the reduced hardware attained by this type of arrangement results in crosstalk effects, i.e., inaccuracies in measuring the resistance values of a sensor due to the influence of other sensors, which is out of the scope of this thesis.

A single FSR sensor can be achieved with a sandwich-like structure as can be seen in Figure 2.9. Commercially available FSR sensors are famous for their basic circuitry and simplicity in use. However, it is possible to obtain a more basic structure using a piezoresistive material mounted between conductive strips.

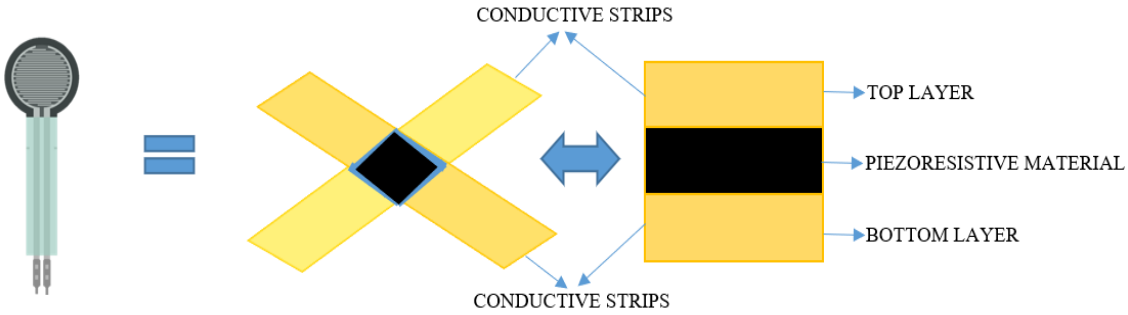

Figure 2.9. Sandwich-like structure for obtaining a FSR

A FSR sensor array could also be replaced by a series of conductive strips, resulting in every intersection of strips acting as an independent pressure sensor in key-matrix circuit as shown in Figure 2.10. Also, as stated before, one of the biggest advantages of this design is that it reduces the number of connections by half for N=M systems.

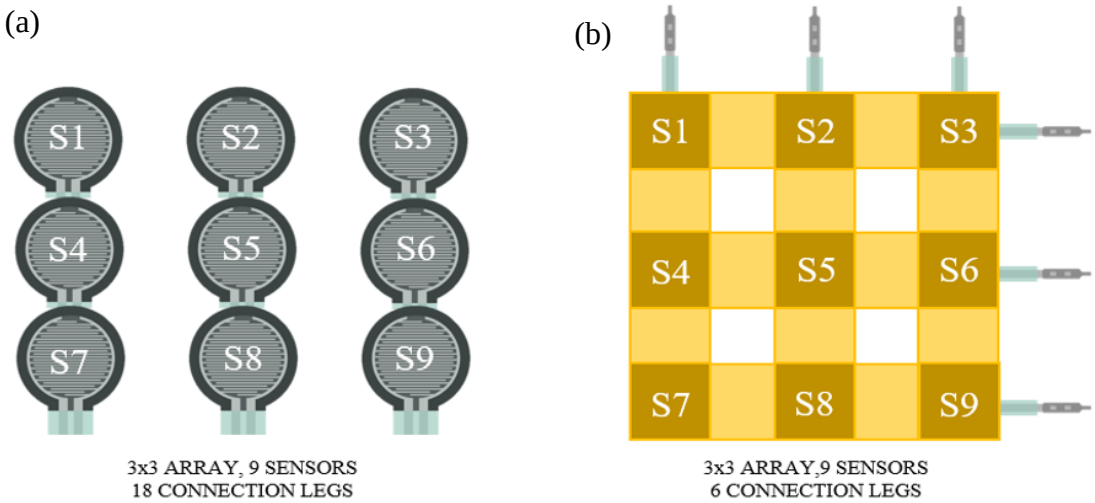

Figure 2.10. (a) FSR array and (b) key-matrix circuit

This sandwich sensor array operates like a key-matrix circuit. So, the way this circuit works is very important and necessary for multi-input applications.

2.2.1. How a Key Matrix Works

Actually, key matrices are an interaction technology. The majority of musical keyboards and computer keyboards employ a key matrix circuit in which the key switches are interconnected by an array of wires, similar to a diode matrix. A keyboard controller can tell which keys are currently depressed by scanning these crossings. According to this method, I/O is separated into two sections: columns and rows. In Figure 2.11, 3-by-3 matrix is presented.

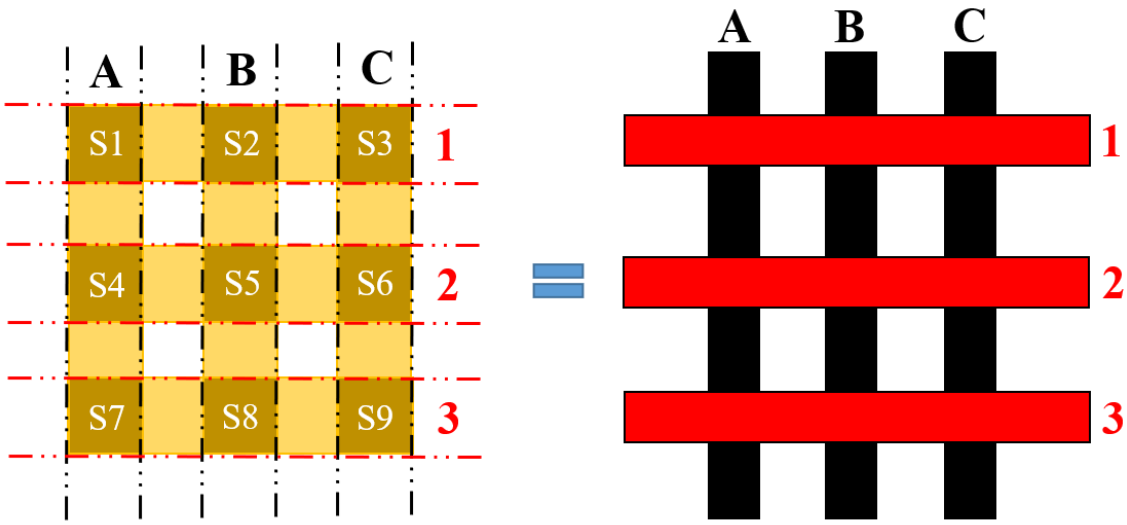

Figure 2.11. 3 x 3 key-matrix example

The black lines represent columns, while the red lines represent rows. There are 9 intersection points between rows and columns. The columns and rows have no connection. Suppose one wishes to construct a key matrix, to accomplish this, one must attach a button (pressure sensors in our case) to each knot. The buttons will make contact when pressed. When the operator presses this button, the corresponding column and row will be connected. Same phenomena stands for our sensor array. When there is no pressure, the intersection point behaves like an infinite resistor (open circuit), as the pressure increases, the resistance goes down and the contact occurs.

The intersection points (pressure sensor points) are named with the Column:Row name that they connect. For instance, the top-left button is named A1 (S1), and the bottom right is named C3 (S9).

In real life applications, these kind of matrix structured sensor arrays are controlled with microcontrollers. For the 9-button 3x3 matrix, 6 pins of the micro controller are used as depicted in Figure 2.12. The first 3 pins will be OUTPUTS and will be connected to the COLUMN wires, while the other 3 pins will be INPUTS and will be connected to the ROW wires. The OUTPUTS of the microcontroller will not have power at the same time. The outputs will go high one by one in cycle. This happens many times per second as a cyclic process.

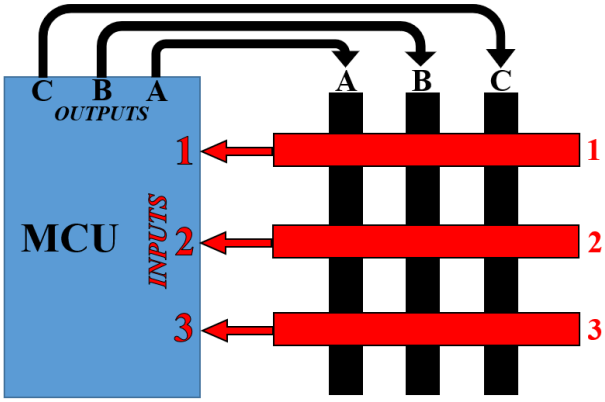

Figure 2.12. MCU connections of a key-matrix

Consider the case where one presses button B2. The outputs of the microcontroller are looped regularly. The B2 button has been pressed by the operator. This button connects column B of the matrix to row 2 of the matrix array. As the output B of the microcontroller becomes HIGH, the signal also arrives via the pressed button at the input 2 of the microcontroller. The MCU monitors the three inputs and identifies a HIGH signal at input 2 when the specific output (B) is high. Therefore, this indicates that input B2 is pressed as can be seen in Figure 2.13. This process is very efficient and simple.

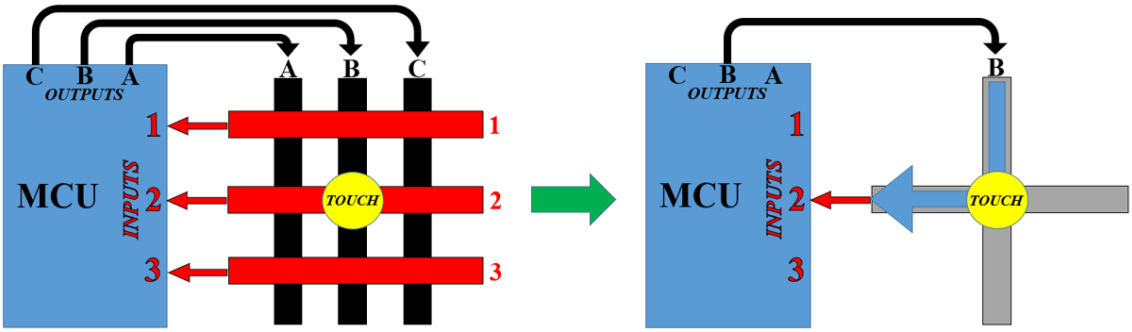

Figure 2.13. Key-matrix functioning

2.2.2. Key Matrix Designs

Another of the great benefit of the key-matrix design is that it allows an infinite number of configurations. For the intended purpose, sensors can be designed in any style and size as can be seen in Figure 2.14. However, in this thesis, as in most commercially sold products, conductive strips of equal thickness are used to make the sensels identical to each other, and the strips are symmetrically aligned relative to each other (Figure 2.14a). Moreover, the thickness of the conductive strips used in the lower and upper electrodes can be selected differently as desired. By the same logic, the distance between the conductive strips can be easily determined according to the intended application. Some examples for different design options to be used in various application areas can also be seen in Figure 2.14.

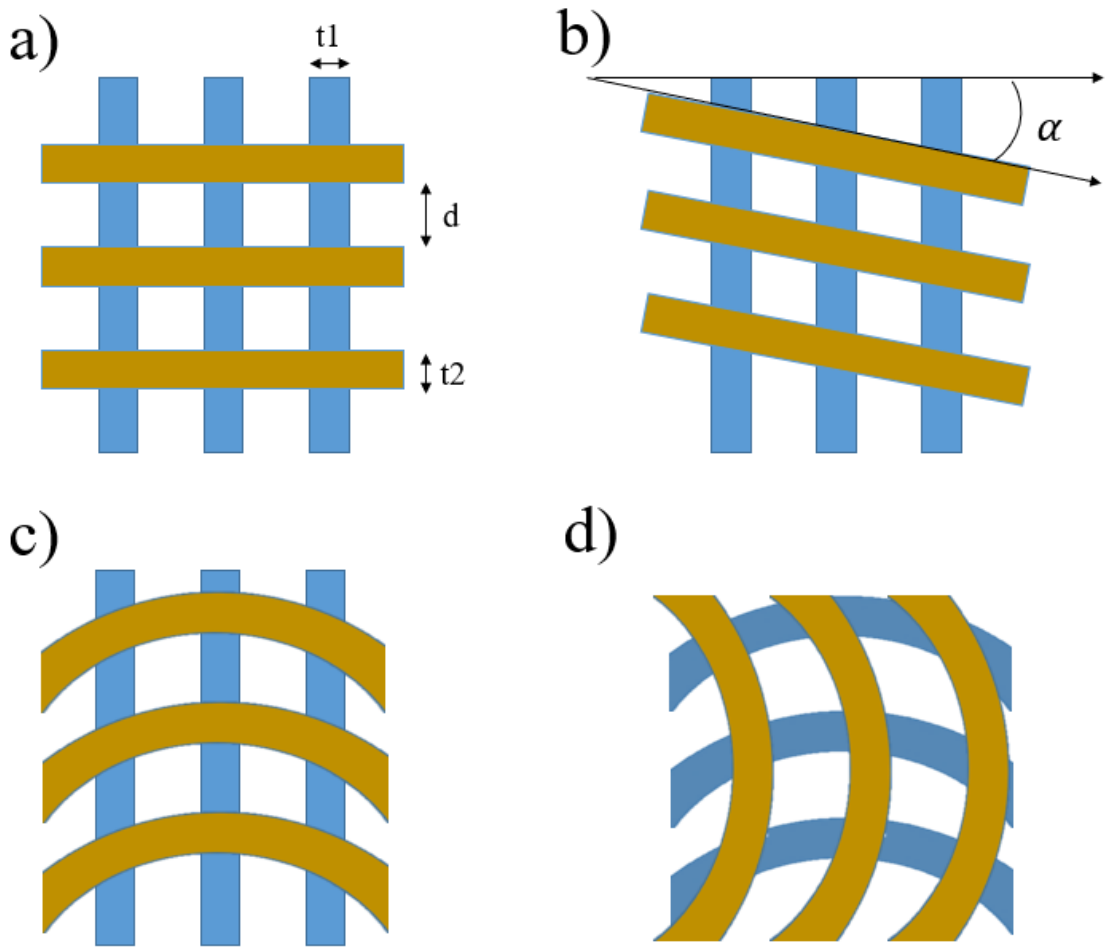

Figure 2.14. Key-matrix designs (a) matrix orientation, (b) angular orientation, (c) one-sided curved elements and (d) two-sided curved elements

2.2.3. Materials Used

As can be seen from the topics mentioned so far in Chapter 2, one doesn't need a lot of material to build a piezoresistive tactile sensor (PRTS). The full list of materials are shared in this section, and information about the most important ones are given in detail.

Materials List:

1) A piezoresistive material such as Velostat™
2) Conductive strips such as copper tape
3) A flexible top and bottom layer such as fabric, acetate film
4) A couple of bias resistors for voltage divider circuit
5) A MCU for powering and operating the system
6) Jumper wires and a breadboard

The structure of the suggested PRTS is simple and distinctive. As seen in Figure 2.15, the two 100-micrometer-thick exterior sheets are composed of a polymeric substance called "acetate." On the inner surface of the acetate sheets, the conductive rows and columns of the matrix are placed. Between the two acetate sheets is a resistive polymer sheet called "Velostat™" with a thickness of 100 micrometers and a specific resistance of 31k Ohm/cm^2. Thus, the entire thickness of the sensor is around 0.3 millimeters. By arranging the two external acetate layers with the conductive strips, placing the Velostat™ and each other orthogonally, the rows and columns of the matrix are created. The intersection points of row I with column J generate the pressure-sensitive active element. The conductive lines on this prototype were 10 mm wide and 2.5 mm apart, and the active area, which is a single active sensor, was 100 mm^2.

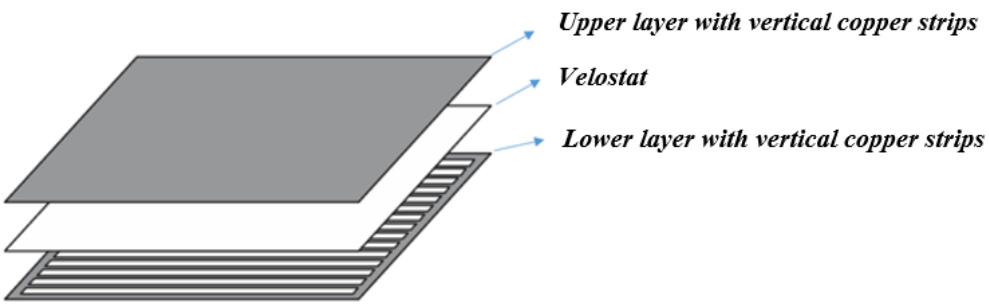

Figure 2.15. PRTS structure

2.2.3.1. Piezoresistive Material

One of the most important components in a PRTS is the piezoresive material. As can be seen in Section 1.1.3, various materials are volleyed, but Velostat™ (Figure 2.16) stands out in terms of its many advantages. Therefore, it is preferred in most of the studies in the literature. Velostat™, also known as Linqstat, is one of the most stable, dependable, and therefore most attractive polymeric composite materials for the creation of touch sensors [51]. The primary benefits of this material are its versatile range of diameters, its mechanical and chemical stability, and its comparatively low cost [49]. Additionally, Velostat™ is very resistant to noise, which negates the need for signal filtering [62]. Velostat™ is a carbon-impregnated anti-static polyethylene sheet as thin as paper [64]. Being infused with carbon offers it higher strength than conventional polymers [65]. Since Velostat™ is a piezoresistive material, its size and shape are adaptable for usage in a variety of applications. For stronger and lighter touch needs, thicker and thinner materials can be utilized, respectively. Velostat™ is also capable of conforming to any object's geometry. Therefore, Velostat™ is selected as the piezoresistive material for the piezoresistive sensor arrays in this thesis.

Figure 2.16. Velostat™

Technical Details

- Dimensions: 11" x 11" (280mm x 280mm)
- 4 mil / 0.1mm thick
- Weight: 18.66g
- Temperature Limits : -45°C to 65°C (-50°F to 150°F)
- Volume Resistivity : <500 Ohm-cm
- Surface Resistivity : < 31,000 Ohms/sq.cm

Velostat™ is a pressure-sensitive conductive sheet and operates like a FSR. Velostat™ changes its electrical resistance due to mechanical effects, such as bending, tension, or pressure. the. The more pressure is applied on it, the less resistant to electricity it becomes. When sandwiched between two conductive layers, it offers a great range of electrical resistance and this is examined through experiments (Figure 2.17). This property makes Velostat™ a superb variable resistor.

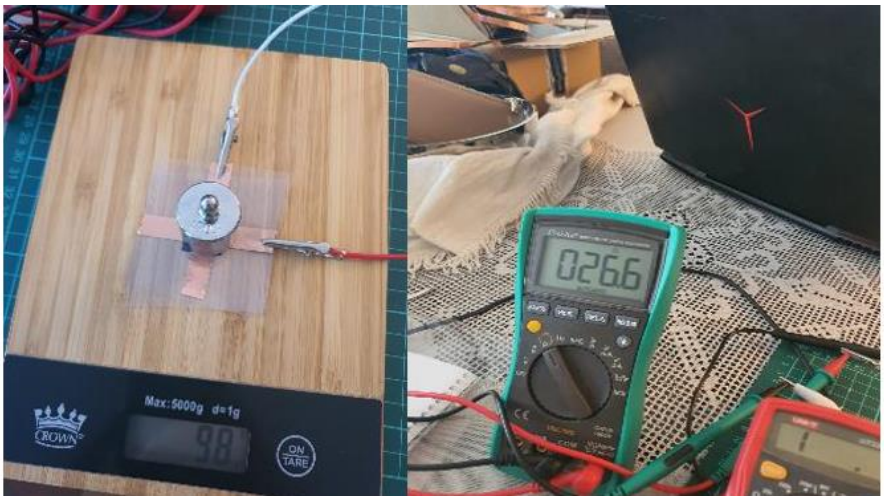

Figure 2.17. Velostat™ resistance measurements

In Figure 2.18, the results of the pre-experiment in which the force-dependent change of Velostat™ resistance is presented.

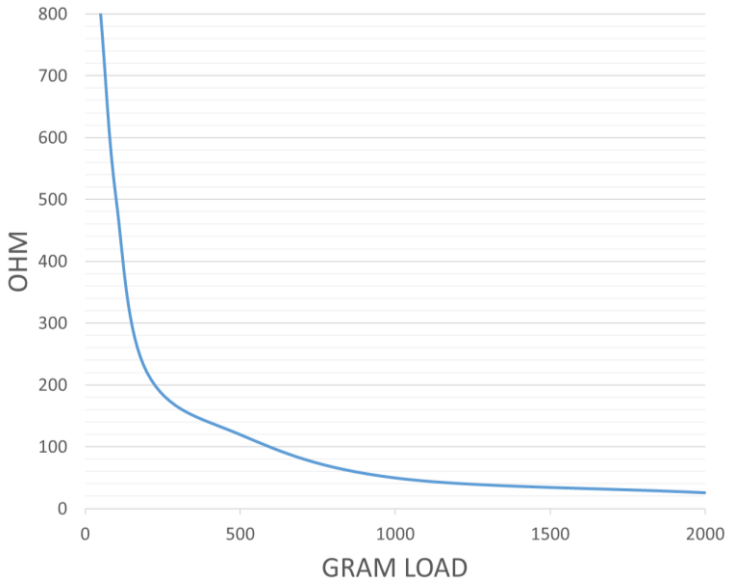

Figure 2.18. Resistance (Ohms) vs load values (grams)

2.2.3.2. Conductive Strips

Many conductive materials can be used in the sensors (see Section 1.1.3), but copper is a reasonable choice because it is both cheap and very easy to supply. Copper tapes (Figure 2.19) have acrylic adhesive properties and have copper foil carriers that conduct electricity. It has a flexible structure made of fine pure copper. Copper takes the form of the surface to which it adheres. It can carry as much current as a conductive cable on which solder can be made. There is protective silicone paper under the adhesive. The ability to solder on it increases the areas of use and has many uses in the electric and electronics sector, industrial sector, construction sector, sanitary installation sector, industrial sector, automobile sector, and defense industry. On the back of the tape is a conductive adhesive. This ensures that both sides of the tape are conductive. Although the adhesive part cannot carry high currents, it can be used in applications such as touch sensors.

Figure 2.19. Copper tapes

Technical Details

- Material: 99,98% Copper
- Adhesive Paper type: Conductive Acrylic Adhesive
- Acrylic Thickness: 0.035 mm
- Copper Thickness: 0.025 mm
- Tensile Strength: 4.5-4.8kg/mm
- Elongation Rate: 3-7%
- Heat Resistance: -10C to 120C

2.2.3.3. Microcontroller Unit

The Arduino Mega 2560 is an ATmega2560-based microcontroller board (Figure 2.20). It contains 54 digital input/output pins, 15 of which are PWM outputs; 16 analog inputs; 4 UARTs (hardware serial ports), a 16 MHz crystal oscillator, a USB connection, a power jack, an ICSP header, and a reset button. It includes everything necessary to support the microcontroller; simply connect it to a computer through USB or power it with an AC-to-DC adapter or battery to get started. The Arduino Mega 2560 is a programmable microcontroller and data acquisition instrument proven reliable for its use in recent studies [66-68]. 16 analog inputs allow you to build up to a 16x16 (256 sensels) sensor system without any extra circuit elements.

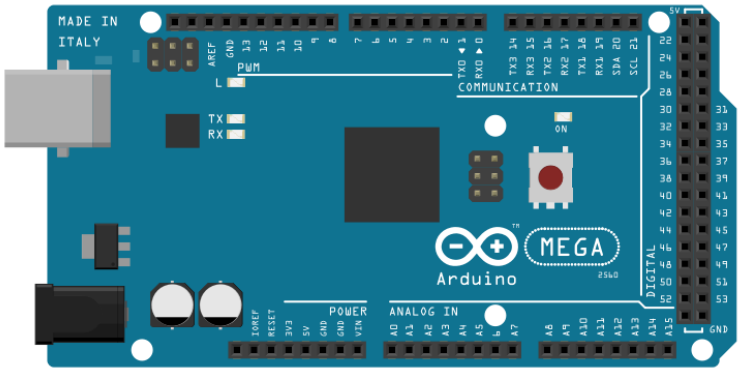

Figure 2.20. The Arduino Mega 2560 MCU

Technical Details

- Operating voltage: 5V
- Input voltage (recommended): 7-12V
- Input voltage (limit): 6-20V
- Dıgıtal i/o pıns: 54 (of which 15 provide pwm output)
- Analog input pins: 16
- Dc current per i/o pin: 20 mA
- Flash memory: 256 kb of which 8 kb used by bootloader
- Clock speed: 16 Mhz
- Length: 101.52 mm
- Width: 53.3 mm
- Weight: 37 g

2.3. Sensor Circuitry

In Figure 2.21 are the connections of the sandwiched 5x5 sensor array to be used in the preliminary experiments. The distance between the copper strips can be chosen or easily adjusted according to the desired study. The links of the 5 columns and 5 rows are indicated in the same color. The 5 rows are connected to the 5 digital pins of the Arduino MCU. Similarly, 5 columns are connected to the 5 analog read pins of the Arduino MCU. As mentioned in the previous sections, a total of 10 (M+N) connection pins were used for a 5x5, i.e., 25-element sensor.

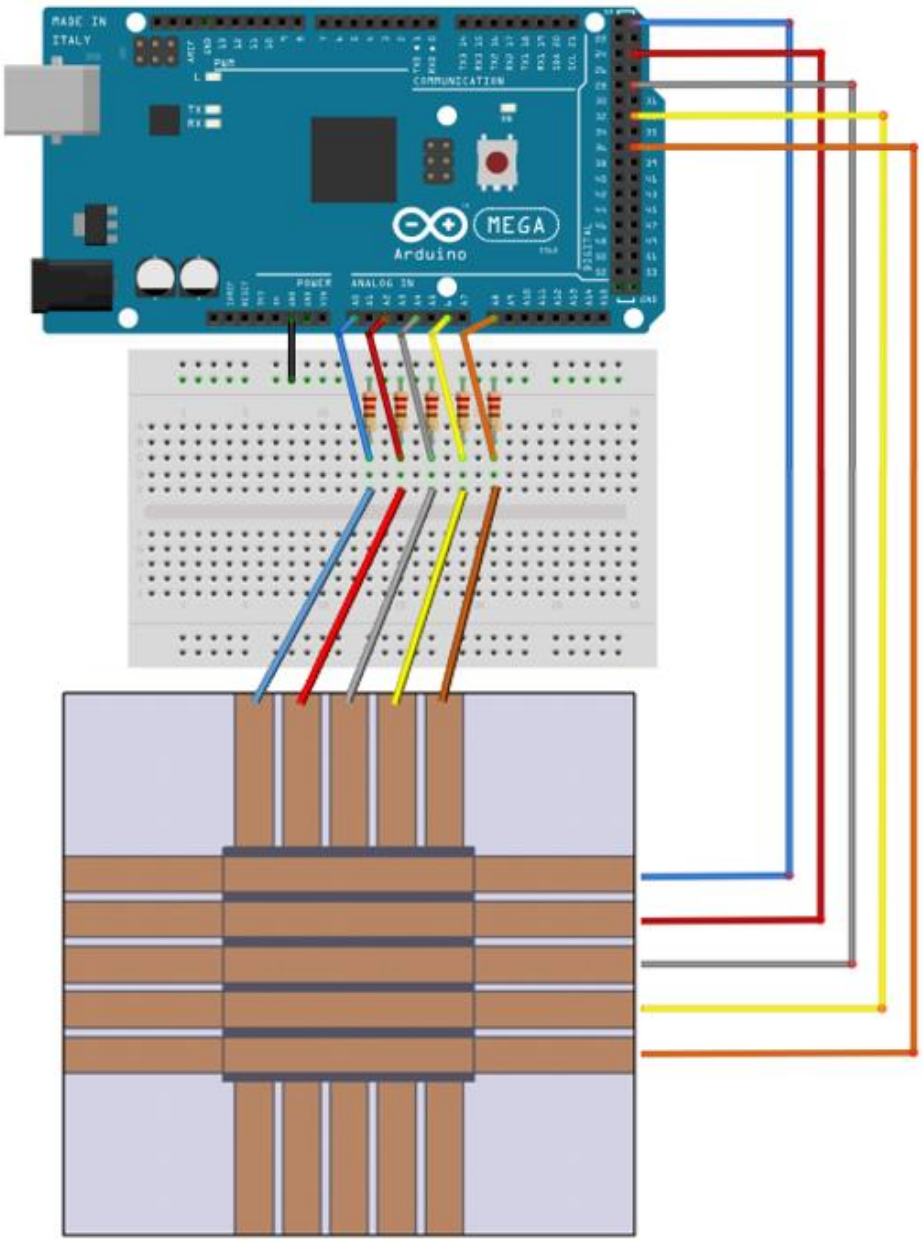

Figure 2.21. 5x5 sensor array circuit diagram

For the following 25 sensels 5x5 matrix, 10 pins of the micro controller are used. The first 5 digital pins will be OUTPUTS and will be connected to the ROW wires, while the other 5 analog pins will be INPUTS and will be connected to the COLUMN wires. The OUTPUTS of the microcontroller will not have power at the same time. The outputs will go high one by one in the cycle. This happens many times per second as a cyclic process. Analog voltage read locations can be seen in Figure 2.22.

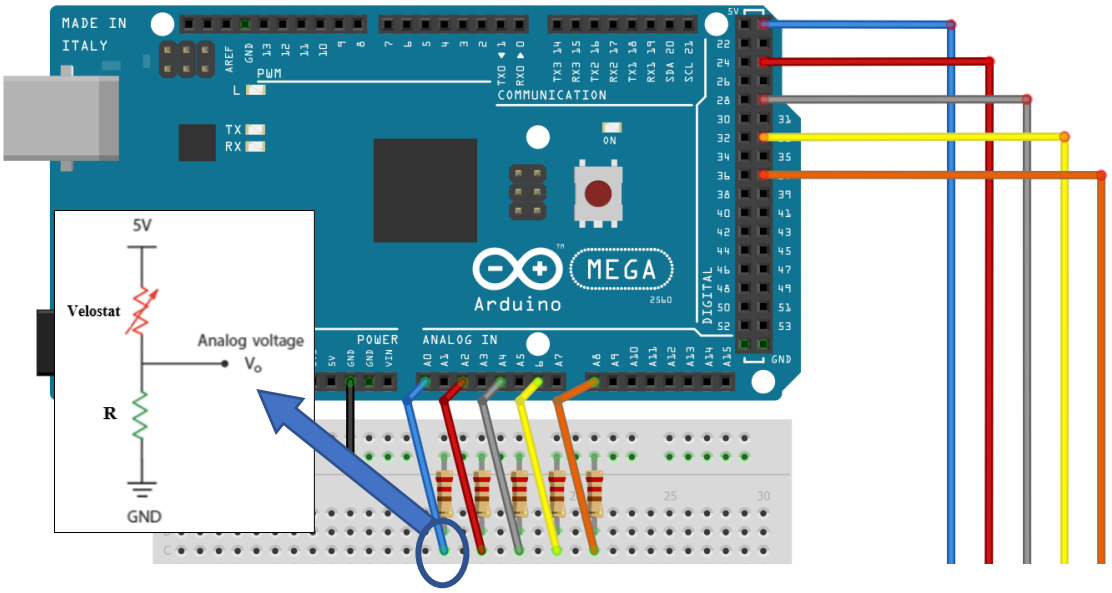

Figure 2.22. Analog voltage read locations

The real sensor matrix constructed can be seen as in Figure 2.23. Black circles are templates for the experiments, which are discussed in detail in Chapter 3.

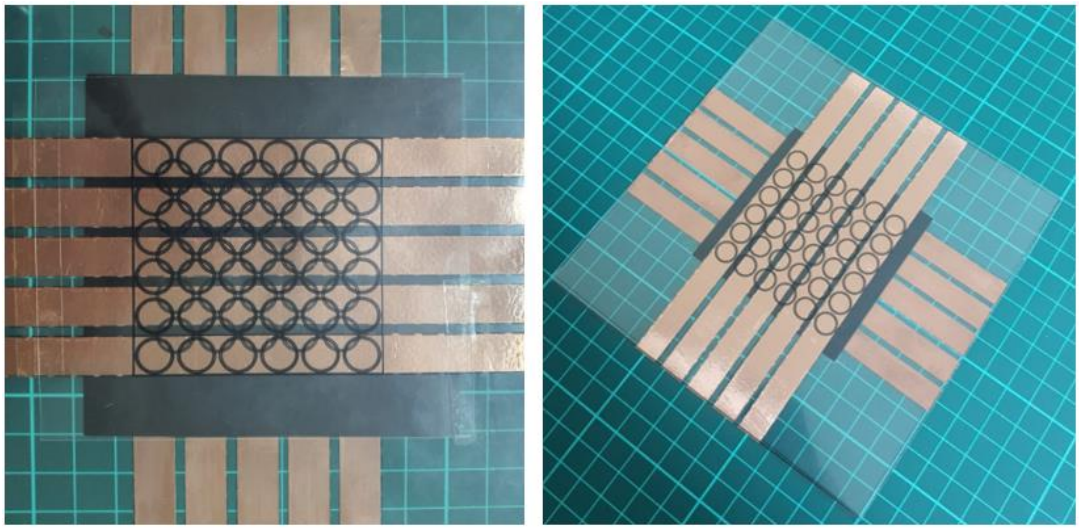

Figure 2.23. 5x5 Sensor array

The completed 5x5 sensor array system created for the preliminary experiments can be seen in Figure 2.24.

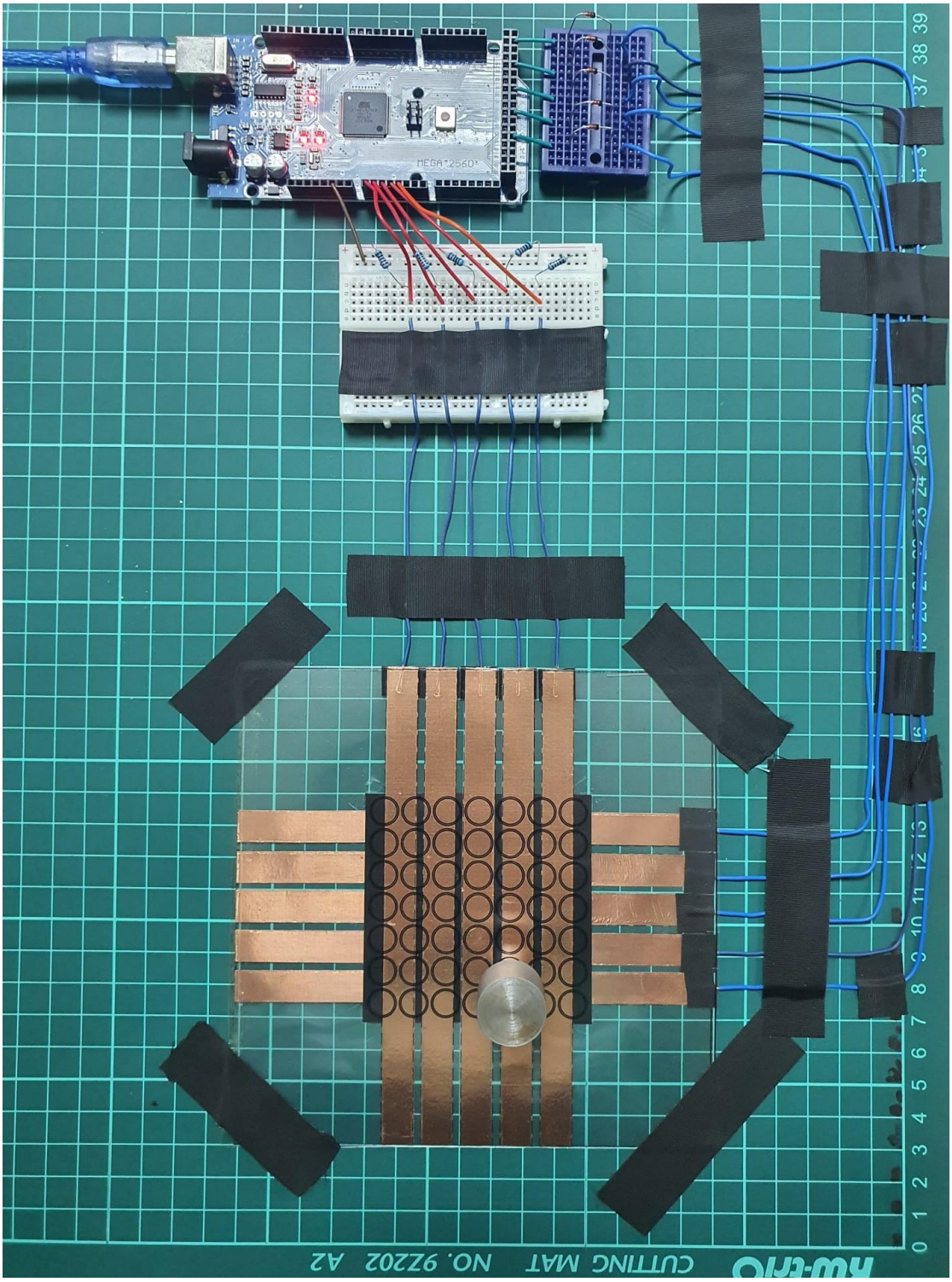

Figure 2.24. Completed 5x5 sensor array for preliminary experiments

2.4. Data Acquisition System

Analog sensor signals are read using analog input pins on the Arduino Mega 260 board. The microcontroller is programmed to read the analog values and transmit the values to a serial-connected computer. The microcontroller that is used, the Arduino Mega 260, has the ability to convert analog to digital, so it does not need an external ADC (up to 16 analog inputs). Each vertical line is implemented as a potential divider with a bias resistor. The methods for selecting the optimal bias resistor are discussed in Chapter 4 via experimental results. On the Arduino Mega 260 board, the outputs of potential dividers are directly connected to five analog inputs and each horizontal line is connected to an Arduino digital output as depicted in Figure 2.25. The program toggles each digital output to high and reads the corresponding analog readings. This technique cycles through all of the matrix's rows and columns.

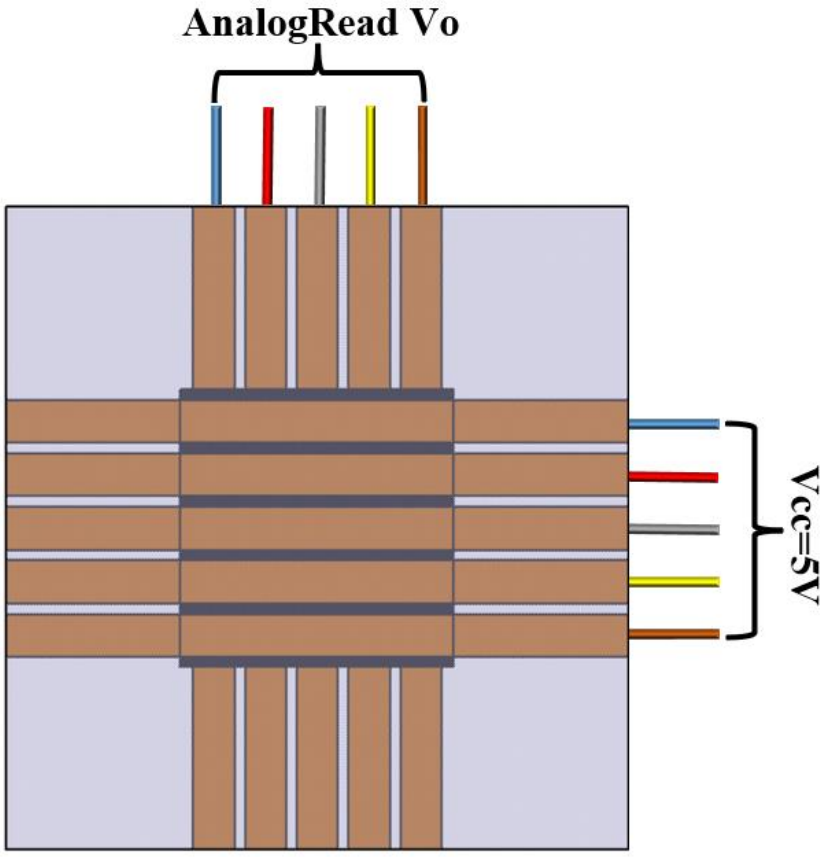

Figure 2.25. Voltage input and output connections

At first, the first row is powered, and starting from the first column, the AnalogRead command is executed until the fifth column AnalogRead command. This

process continues until all rows and columns are covered. This is called a "complete cycle" in the sensor array. A complete single cycle can be seen as in Figure 2.26.

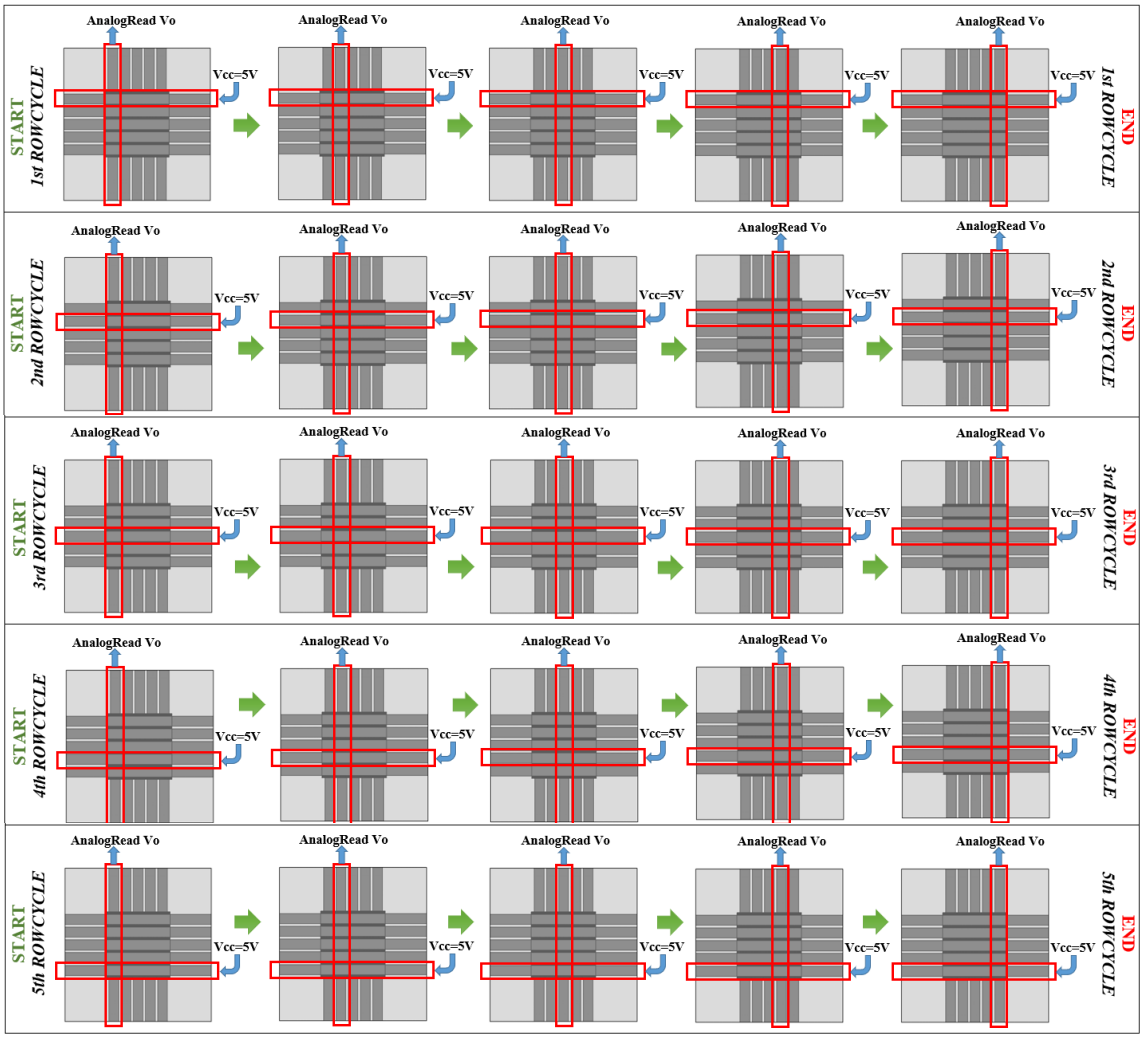

Figure 2.26. A complete single cycle of a 5x5 sensor array

2.4.1. AnalogRead() Procedure

This function reads an analog value from a 10-bit analog-to-digital converter linked to an analog pin. This means that when sensor values are printed to a serial window, the range will be 0 to 1023. The Arduino Mega 2560 contains a 10-bit analog-to-digital converter built-in. Hence, it means that input voltages between 0 and 5 volts will be converted to integer numbers between 0 and 1023. This results in a reading resolution of 5 V per 1024 units, or.0049 volts (4.9 mV) per unit.

2.4.2. Arduino IDE Setup

After completing the required hardware connections, it is necessary to upload the required code to the MCU in order for our sensor to function. To activate Arduino MCUs, the Arduino IDE, which is its own software interface, must be utilized. Through this application, we may compile and upload functional code to the Arduino MCU. In this thesis's sensor production, version 1.8.13 of the Arduino IDE is utilized. In addition, under the "Tools" tab of the IDE, the kind and model of the MCU to be used must be selected in the "Board" section as can be seen in Figure 2.27.

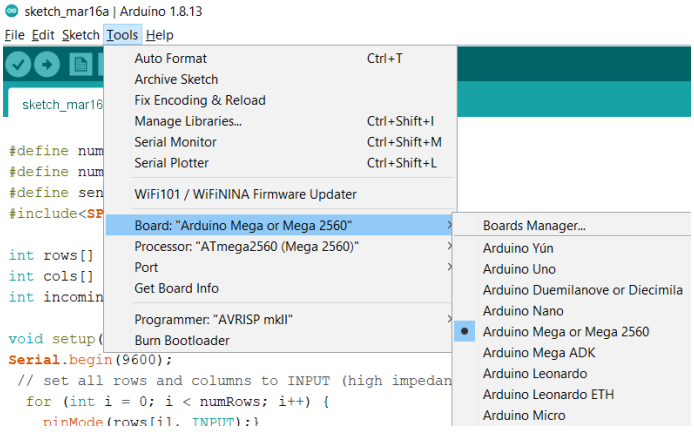

Figure 2.27. Arduino IDE board selection menu

Then, in the "Port" section of the "Tools" tab, one must correctly select the port where the MCU is installed on the computer in order to do our activities appropriately (Figure 2.28). Following these procedures, the sensor code can be uploaded into the MCU without issue. Complete sensor code is provided in Appendix A.

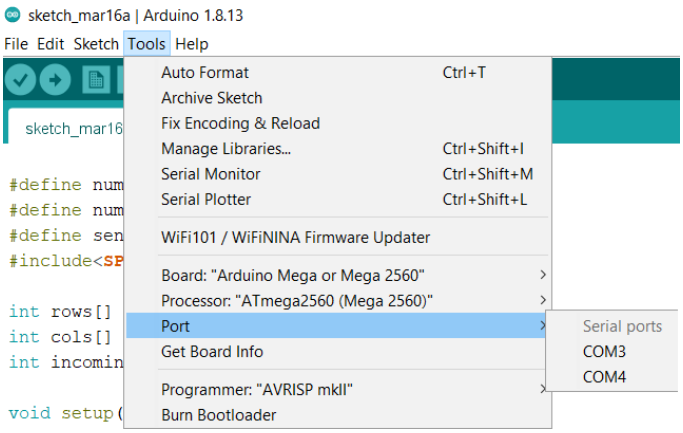

Figure 2.28. Arduino IDE port selection menu

CHAPTER 3

METHODS

3.1. Data Recording and Processing

As mentioned in the previous chapter, Arduino's own IDE is used to program and upload the code into the MCU, which is utilized in the sensors made and tested in this thesis. In addition to this, it is possible to transfer the data information obtained from Arduino MCUs through its own IDE to other programs (Matlab, Phyton, etc.) via serial communication. Since Python or Matlab can be used in many different fields, like data science and machine learning, it becomes much easier to process the transferred data or do statistical analyses. Another area where one can use this type of software is external hardware control, which could be a light or a sensor array. In this thesis, several different softwares are used for different purposes (Table 3.1). The data information in the touch sensors manufactured and used in this thesis is obtained by the means of the "Pyhton 3.10" program, and the data information is processed through this program and the proposed analyses were realized. Moreover, "Data Analysis Tools" in "Microsoft Excel" are preferred for regression analysis due to their ease of use. The green-indicated items in the Table 3.1 are the new method that this thesis suggests as a low-cost error reduction method. In this thesis, by implementing Kadane's algorithm, it is attempted to achieve a low-cost error reduction method without the use of additional hardware elements.

Table 3.1. Softwares used in the thesis

#	Name	Software Tool
1	3D sensor array design	Catia v5
2	Data stream recording	Arduino IDE & Python 3.10
3	COP calculations with "Raw Data" & "Kadane Algorithm"	Python 3.10
4	Least squares circle fit with "Raw Data" & "Kadane Algorithm"	Python 3.10
5	Multivariate linear regression with "Raw Data" & "Kadane Algorithm"	MS Excel
6	Plottings of the results	Python 3.10 & MS Excel

3.2. Sensor Setup and Load Properties

The most difficult and essential aspects of this study and thesis are determining the sensor design and the size of the touch/force contact area. Since the sensor design in this thesis employs 10 mm copper strips, which are commonly favored in commercial products, each sensor has a 1 cm^2 measuring area and is capable of measuring in this region. Therefore, the question of how far apart to position each sensor is one of the most challenging topics in sensor arrays. Due to the usage of plantar sensor structures, as indicated in section 3.3 of the COP calculations, each sensor is typically positioned as far apart as its own width. This design approach is not problematic in applications with a large force field, such as human foot (Figure 3.1a). However, because the force employed in this thesis would be the human fingertip, the design issue becomes much more crucial. In other words, designs for commercially available sensor arrays or those developed from scratch, as in this work, must be chosen and/or designed specifically based on the pressure area and the applied force. Otherwise, there would be some dead zones in the sensor array (Figure 3.1b). The best thing about key matrix design is how easy it is to solve these kinds of problems since these designs can be made in any size and scaled up or down depending on how they will be used.

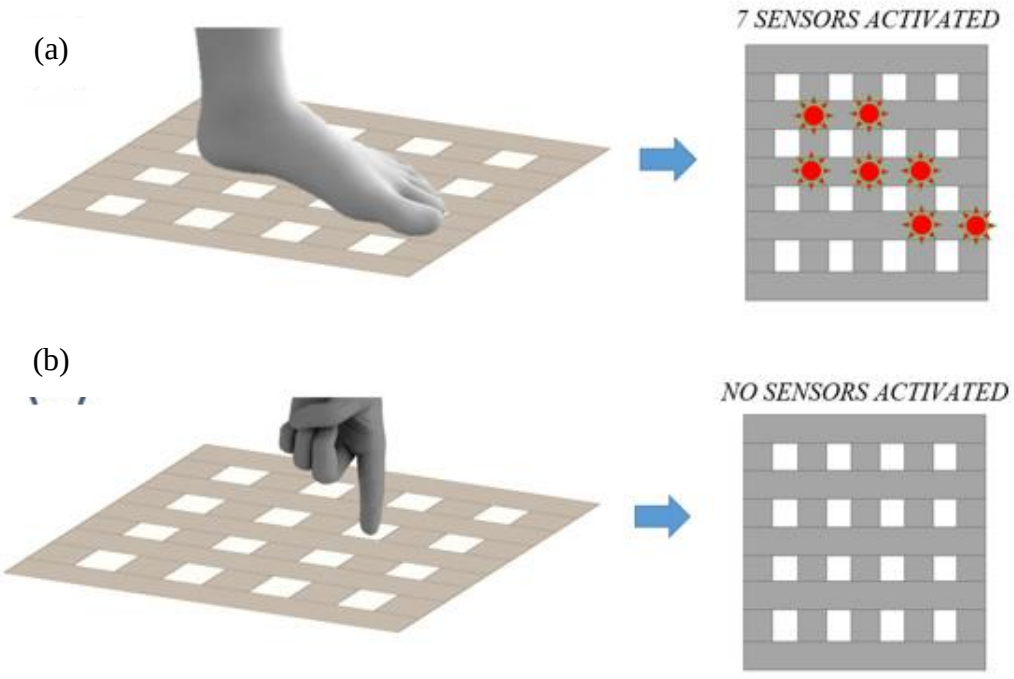

Figure 3.1. (a) Large force field and (b) small force field

3.2.1. Load Contact Area Determination

As it has been stated before, the main goals of this study and thesis were to find the optimal sensor design and the size of the touch/force contact area according to the human fingertip. In the literature on this subject, the term "Touch Target" is included, and this criterion is taken into account in touch-controlled devices. People find it more difficult to strike smaller touch targets than larger ones. When designing mobile interfaces, it's ideal to make tap targets large so that users can easily interact with them. Small touch targets are more difficult to hit since they demand more precision. The user must realign their finger from the pad to the tip in order to contact the target with clear visual feedback. Users hit little touch targets with their fingertips because it provides them with the necessary visual input to ensure they are striking the target accurately. When users must realign their fingers, however, their movement is slowed, and they must exert more effort to hit their target. Moreover, the size of a target should not cause them to commit touch errors. In a study conducted by the MIT Touch Lab to investigate the Mechanics of Tactile Sense, the typical width of an adult's index finger was determined to be between 16 and 20 millimeters [78]. A target size study for one-handed thumb use on small touchscreen devices discovered that as the target size increased, user mistakes decreased [79] as depicted in Figure 3.2. 7–10 mm is the suggested touch target for touchscreen elements. Larger touch targets may be necessary to accommodate a broader range of users, such as children with growing motor abilities. Therefore, in this thesis, a 9 mm load/touch area is selected due to the studies in the literature.

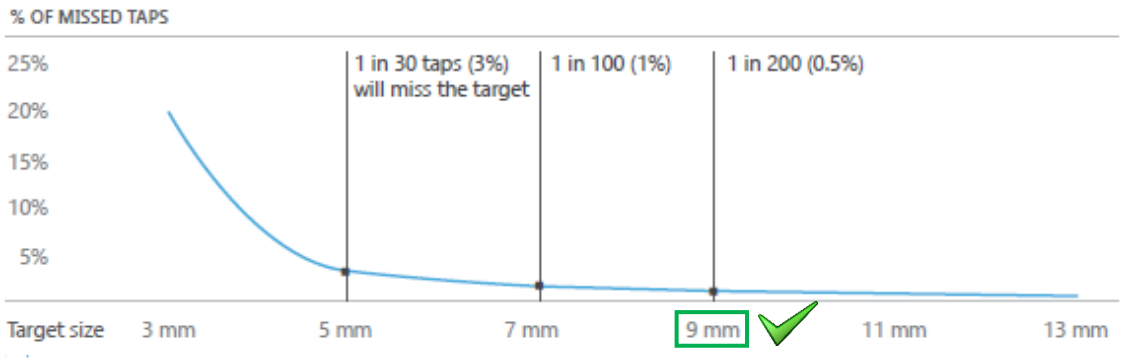

Figure 3.2. % of missed tap vs touch target size [79]

3.2.2. Load Magnitude Determination

Once the load contact area is determined, the next step is to choose the load magnitude. Again, there are various studies about this topic in the literature. Touchscreen interaction often involves many types of touch gestures, such as tapping, swiping, and pinching. The minimum of the mean fingertip resultant force measured among seven different gestures in a study about these interactions and their force measurements [80] is about 0.5 N (≈50 g) as depicted in Figure 3.3.

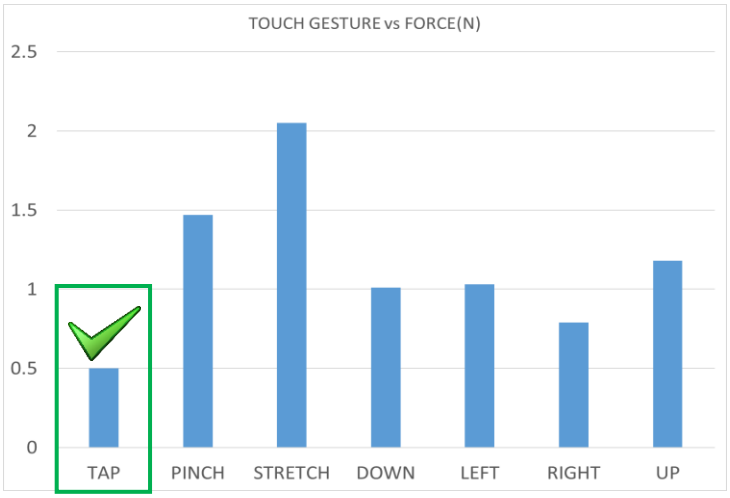

Figure 3.3. Forces of different touch gestures [80]

According to the results of this study, the minimum value in terms of force sensitivity is selected for the touch test to be performed on the sensors in this thesis. As a result, for the experiments in this thesis, a load is determined with a 9mm contact area and 50 g weight for the minimum force case. In Catia v5® software, such a load is designed and manufactured in the workshop to simulate human fingertip touch force (Figure 3.4).

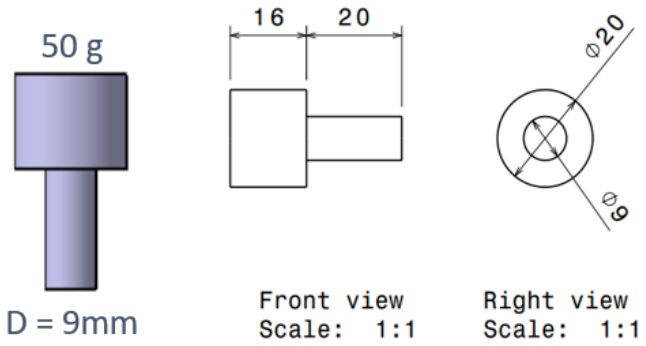

Figure 3.4. 50 g weight's technical drawings

3.2.3. Sensor Configuration and Dimensions

After determining the force and dimensions to be used in the position tests of the sensor, it is necessary to design a sensor array suitable for these specifications. For a healthy application, it should be possible to move freely on the system so that this force touches at least 1 entire measuring point on the sensor array as much as possible. That's why the distance between copper strips is so critical. If the distance between the copper strips is greater than the contact diameter of the force to be applied, there will be blind spots on the sensor array that cannot be measured. Therefore, the distance between the copper strips should be maximum 9 mm so that no information is lost as a measurement in any area of the sensor array. Therefore, during the design phase of this study, 10 mm wide copper strips lined up simultaneously within an area of 60 mm x 60 mm were arranged symmetrically (Figure 3.5a and b). The Catia v5® CAD program is used for these design studies. As mentioned in the previous sections, since it is a 5x5 system, there are 25 separate sensor points in this system. The most important point to be considered in this design is that when the test load with a diameter of 9 mm is placed in any desired area in an area of 60 mm x 60 mm, this weight touches at least 1 and at most 4 sensor points (Figure 3.6). This shows that this design is healthy and sufficient in terms of this study's tests.

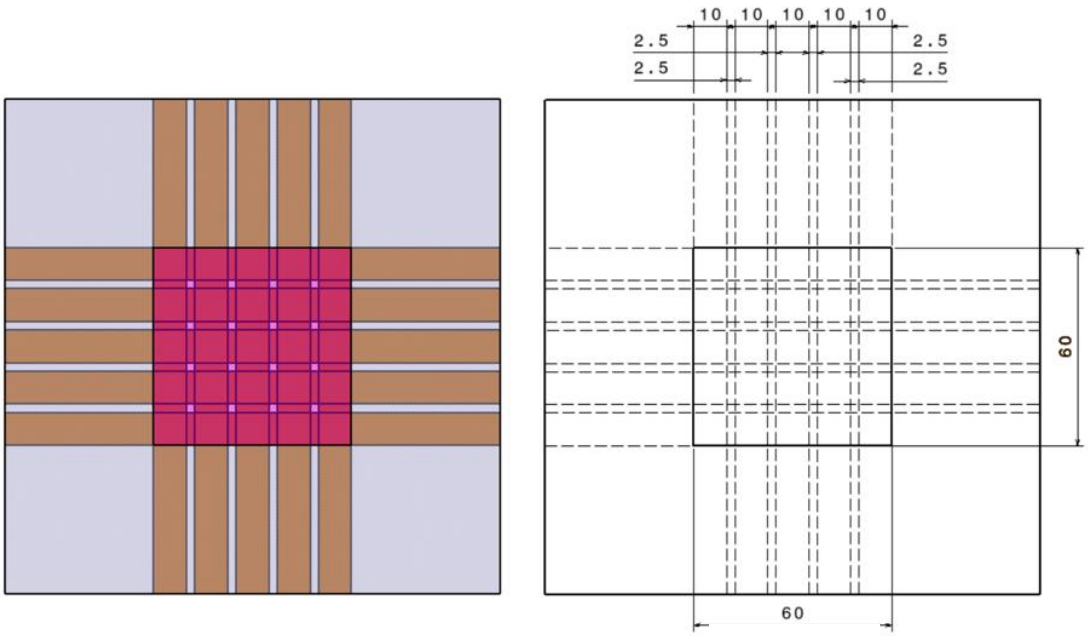

(a) (b)

Figure 3.5. (a) 5x5 sensor design and (b) dimensions

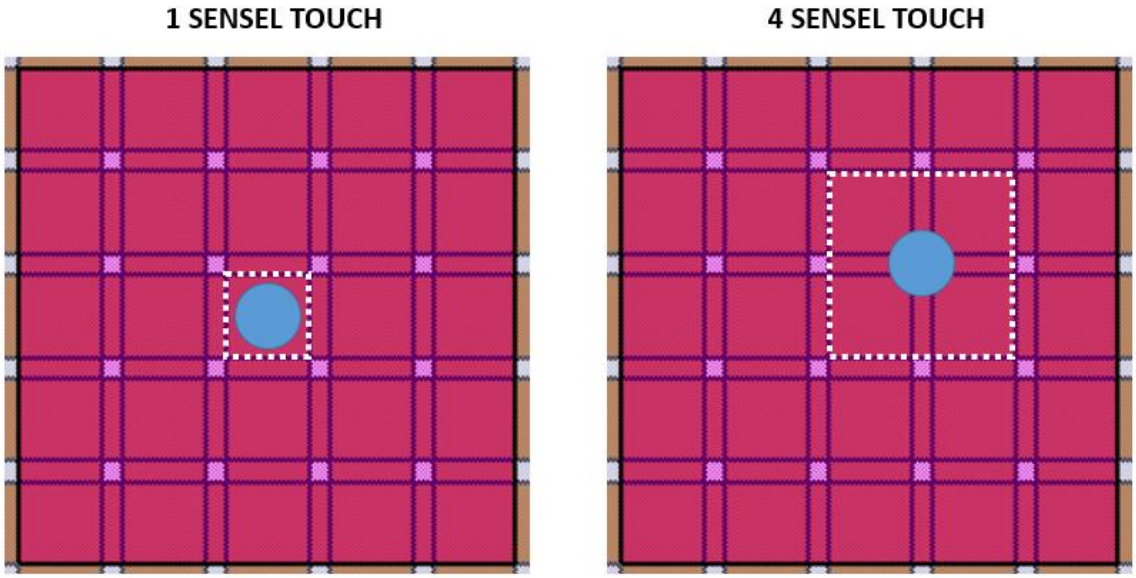

(a) (b)

Figure 3.6. (a) one sensel touch and (b) four sensel touch

After deciding on the sensor dimensions, another important issue was the test points where the load could be placed on the sensor and in the desired position in the same way every time. In order to carry out as many tests as possible, 61 test points were identified on the sensor, and these points were marked on the sensor by means of a special template (Figure 3.7). Thus, possible positioning errors were prevented while performing the tests. Finally, according to selected parameters, the sensor array going to be used in sensor tests is produced. Coordinates of these points are provided in Appendix D.

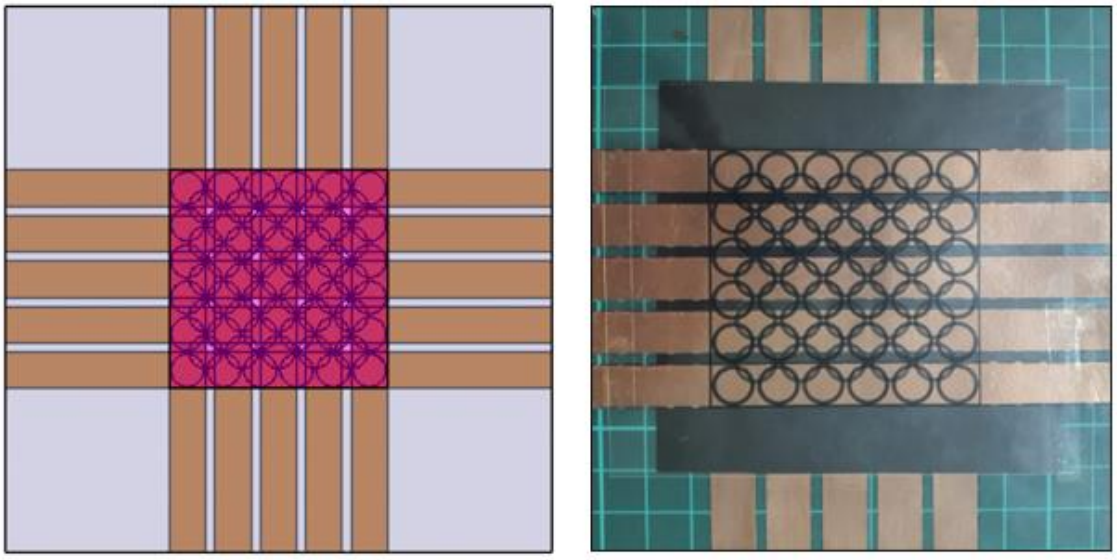

Figure 3.7. Template markings for load tests

3.2.3.1. Contact Areas of the 61 Test Points

According to the design of the sensor array, test points don't have the same contact area on the system and sensels. Grey areas are the non-contact (dead) sections of test points as can be seen in Figure 3.8.

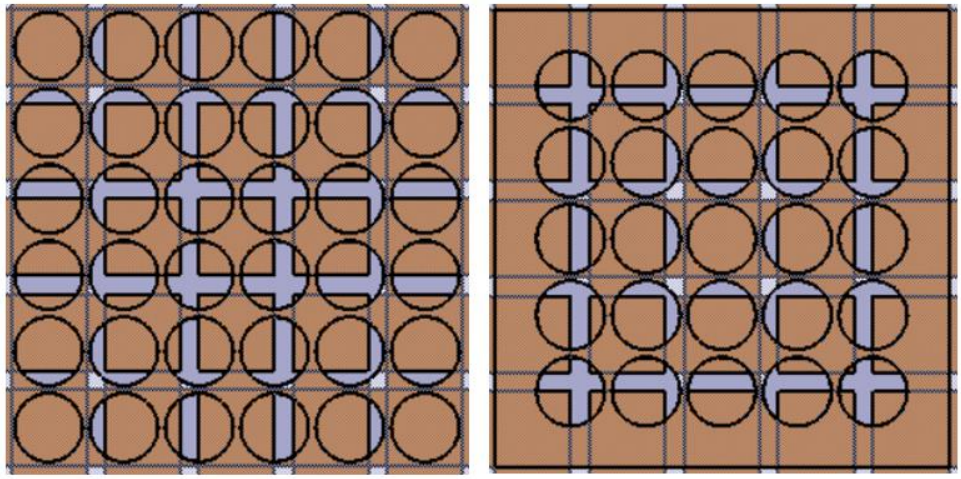

Figure 3.8. Non-contact zones of the 61 test points

Considering these grey areas, the contact area ratios of each test point to the sensels on the sensor are presented in Figure 3.9. These data are extracted so that they can be used to examine the relationship between errors and the load contact area in Section 4.6.

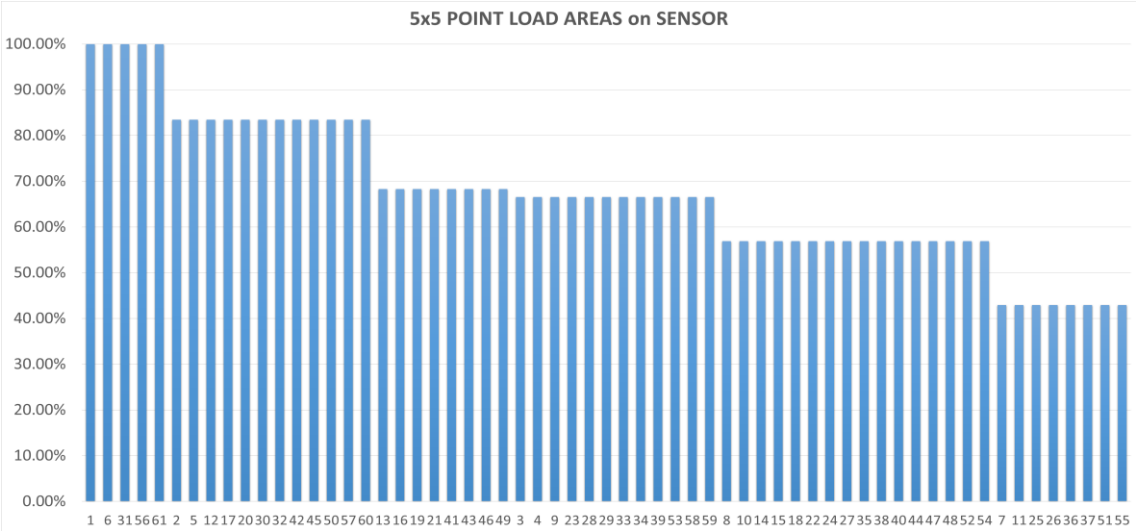

Figure 3.9. Contact areas of the test points

3.3. Center of Pressure (COP) Calculations

The center of pressure (COP) is the place where the whole force of a pressure field acts on a body, causing a force to act via that point. Using COP measures, balance deficits and postural instability caused by conditions like clubfoot [70] and stroke [71] or diseases like Parkinson's disease [72] and diabetic neuropathy [73] have been studied. They can also be used to evaluate the efficacy of therapies such as surgery for hip osteoarthritis [74]. Other applications of COP measures include the evaluation of amputees' postural and balance control [75]. COP characteristics are also used in prosthetic design [76]. In each of these applications, measurement precision is crucial since the data is used to diagnose and treat patients. Current COP measurement devices include force platforms, pressure pads, and pressure insoles [77]. Furthermore, in this thesis, COP estimations are used to identify finger contact locations, such as those of stroke patients [37]. The first sensor assembly with 25 sensels and the origin point used in the COP calculations are shown in Figure 3.10.

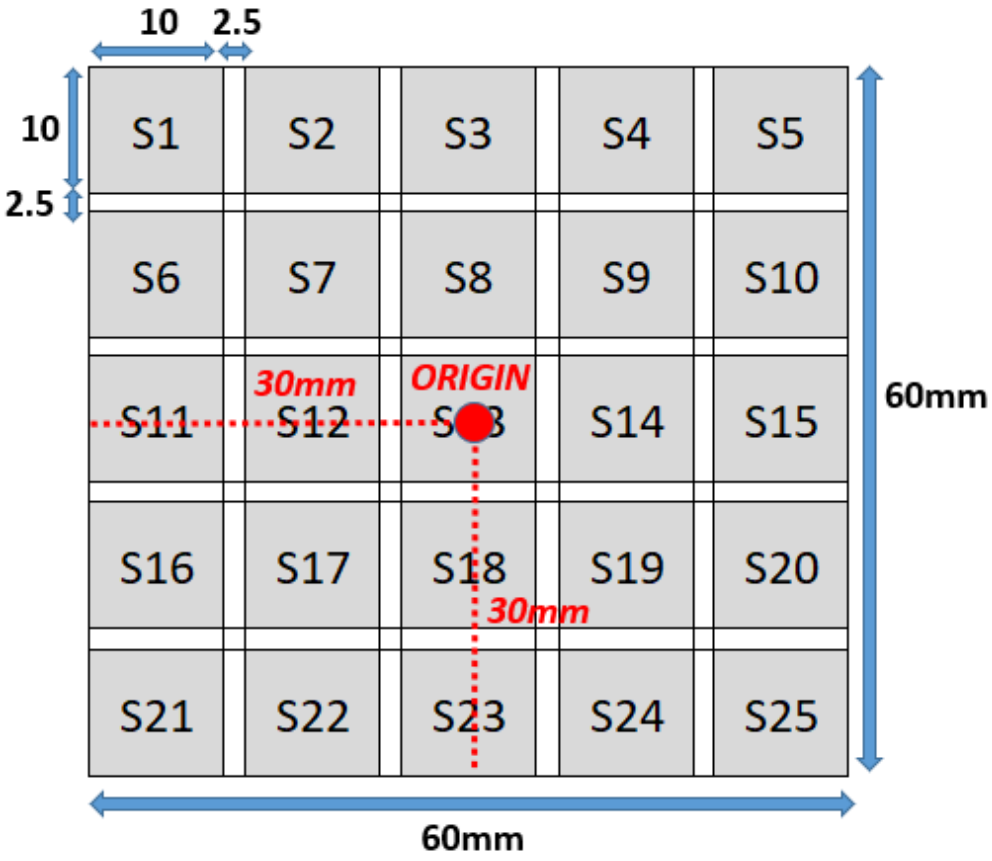

Figure 3.10. 25 sensels with the origin point

There are 25 sensels in the 5x5 sensor matrix system, each located 2.5 mm away from each other. Therefore, a 60 mm x 60 mm area is covered by 25 sensor points. Due to the width of the conductive copper strips, each sensel area has 1 cm^2. Assuming there is a load perfectly located at origin point (0,0) or the point 31, each sensel will read a value between 0 and 1023, as shown in Figure 3.11.

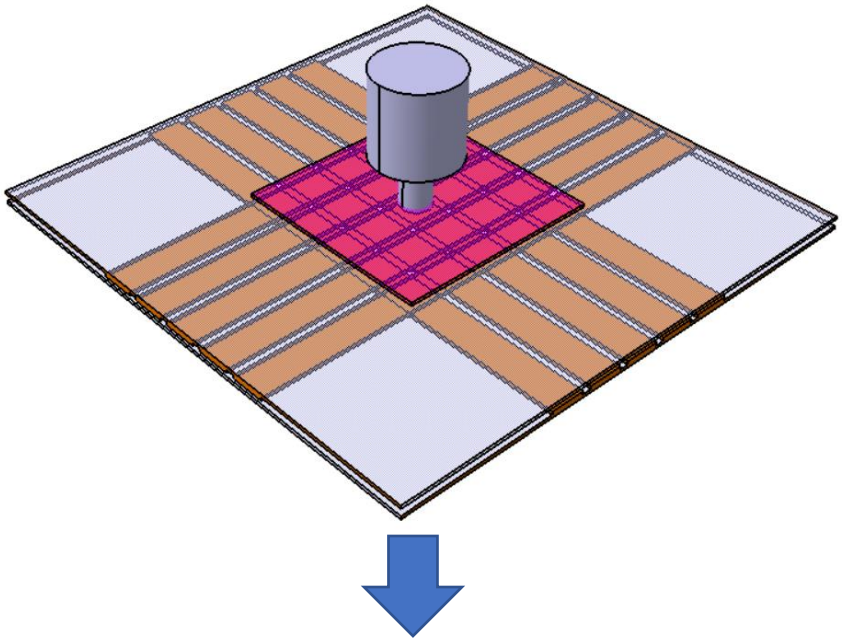

LOADED

2	5	15	1	0
1	5	31	6	2
18	28	501	41	10
3	2	8	0	1
0	1	8	4	0

Figure 3.11. Test load at point 31 and corresponding sensor readings

Now, using basic math, one can calculate the COP of the system by considering all 25 sensing blocks (sensels). However, one should consider the idle readings in the system.

Sensors using this type of piezoresistive material operate very precisely. Although the sensor is completely planar on a flat surface and there is no load on the system, the sensor values differ from zero. Therefore, in such position locating applications, the difference between the loaded state of the system (Figure 3.12) and the unloaded state (Figure 3.13) is taken, and the net change created by the force is found. And then, COP calculations can be made. This method should be applied for all test points at every measurement. Unloaded readings also depend on the bias resistor used in the system, which are discussed in Section 3.4.

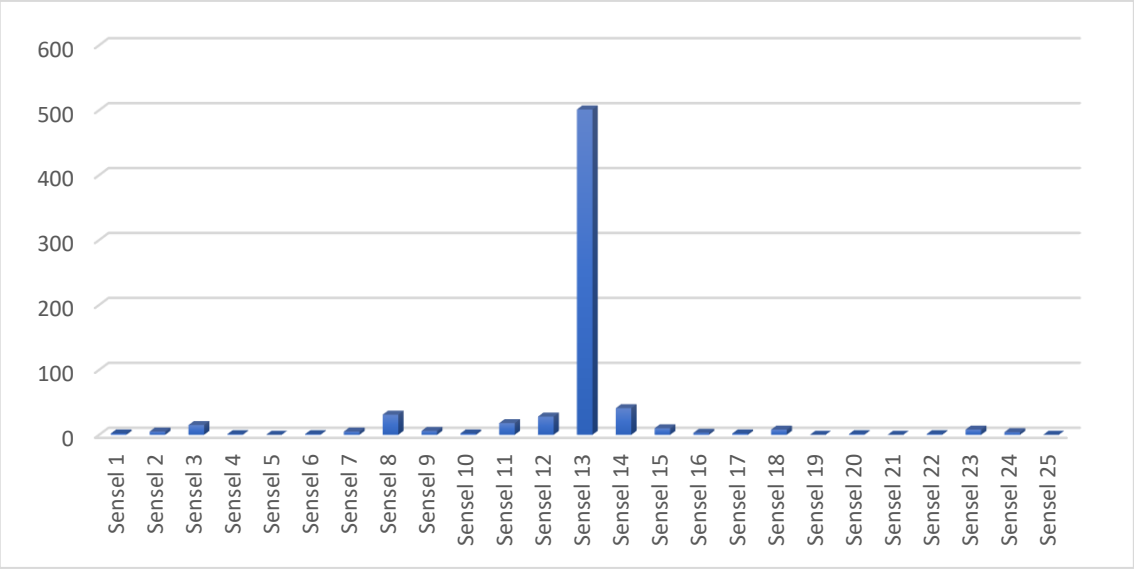

Figure 3.12. Loaded state of the sensor array

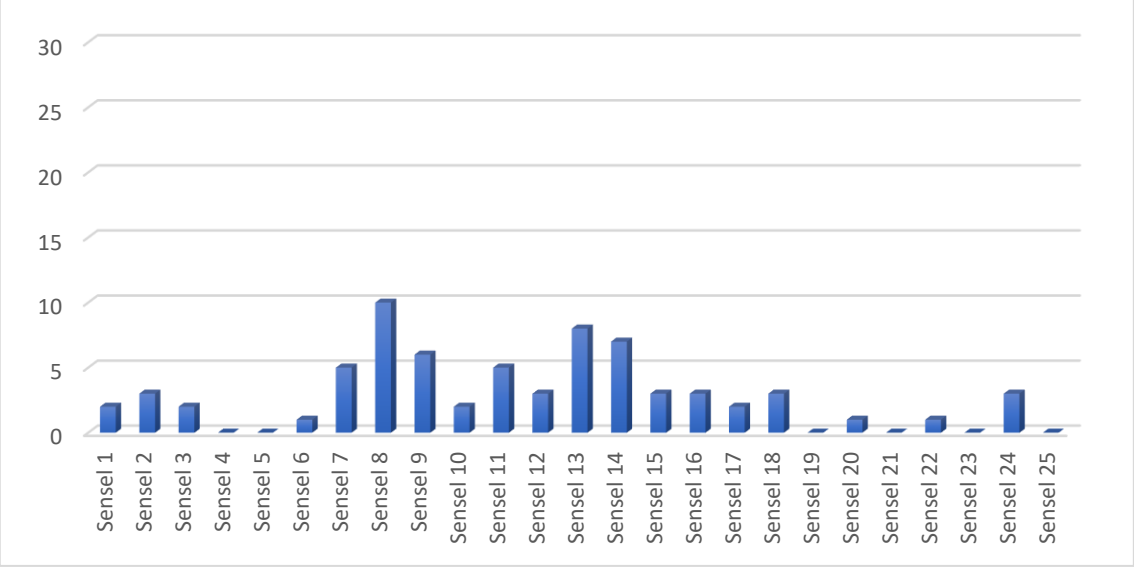

Figure 3.13. Unloaded state of the sensor array

The data in Figure 3.12 and Figure 3.13, are the mean values of the values read on the sensor at every single measurement cycle. In this thesis, measurements were taken for approximately 5 seconds, loaded state and unloaded state, at each of the 61 measurement points. And by averaging these obtained values, these average values were used in COP calculations and other analyzes. The unloaded states of the sensor can change at any time because the sensor can measure very precisely and the sensor can not be perfectly planar all the time (Figure 3.14-15), therefore sensel values can differ at every measurement. Two different unloaded state values are presented as an example, in Table 3.2. Likewise, in loaded states, due to the deformation of the piezoresistive material, the values read may vary slightly depending on the duration. Hence, a measurement of one loaded and one unloaded state on each point was taken for 5 seconds and the relative force change was calculated each time and used in the main experiments.

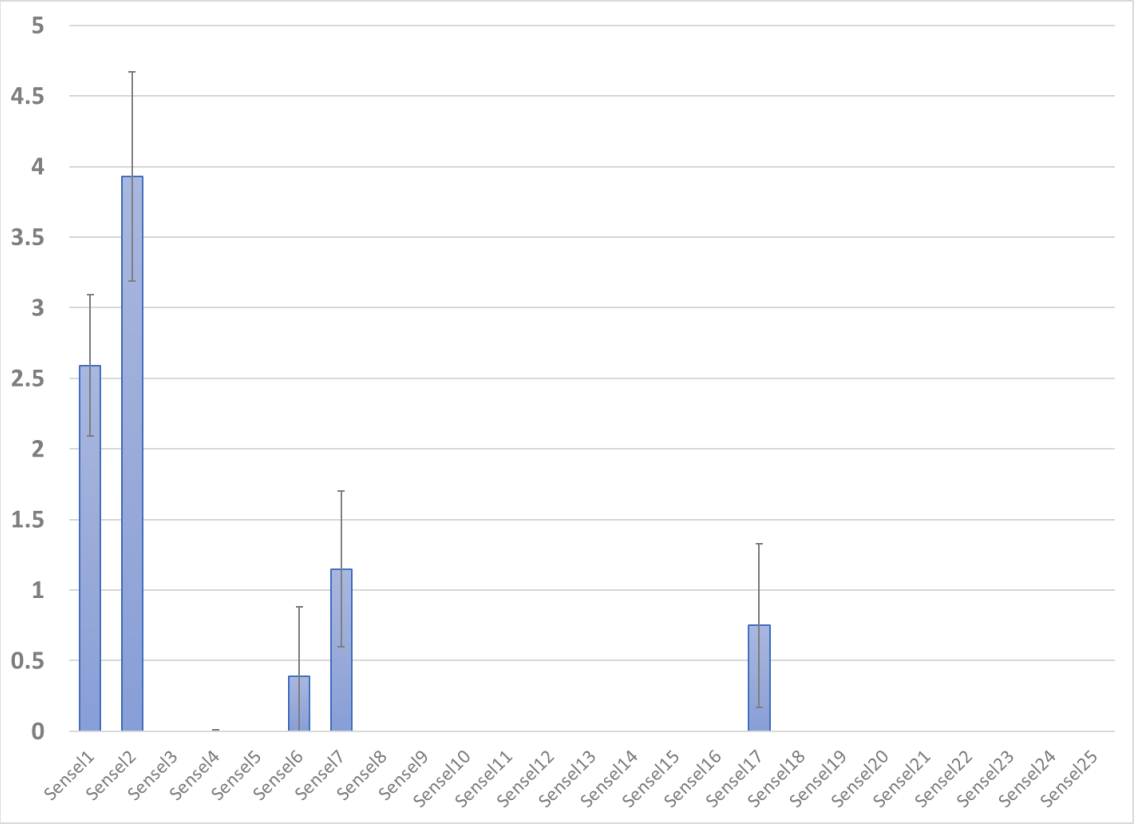

Figure 3.14. Unloaded state 1 sensor readings

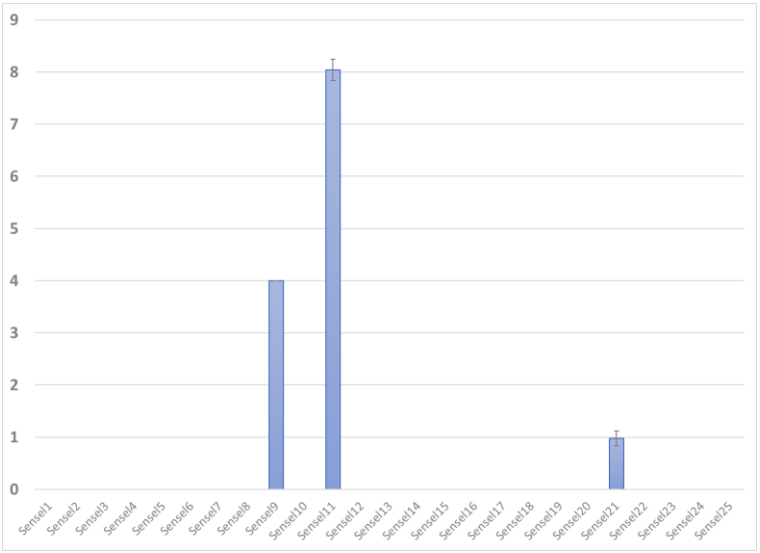

Figure 3.15. Unloaded state 2 sensor readings

Table 3.2. Different unloaded states sensor readings

Sensel #	**Unloaded State 1**				**Unloaded State 2**			
	Min	Max	Mean	Std Dev	Min	Max	Mean	Std Dev
Sensel1	0	4	2.59	0.5	0	0	0	0
Sensel2	0	6	3.93	0.74	0	0	0	0
Sensel3	0	0	0	0	0	0	0	0
Sensel4	0	1	0	0.01	0	0	0	0
Sensel5	0	0	0	0	0	0	0	0
Sensel6	0	1	0.39	0.49	0	0	0	0
Sensel7	0	2	1.15	0.55	0	0	0	0
Sensel8	0	0	0	0	0	0	0	0
Sensel9	0	0	0	0	4	4	4	0
Sensel10	0	0	0	0	0	0	0	0
Sensel11	0	0	0	0	8	9	8.04	0.20
Sensel12	0	0	0	0	0	0	0	0
Sensel13	0	0	0	0	0	0	0	0
Sensel14	0	0	0	0	0	0	0	0
Sensel15	0	0	0	0	0	0	0	0
Sensel16	0	0	0	0	0	0	0	0
Sensel17	0	2	0.75	0.58	0	0	0	0
Sensel18	0	0	0	0	0	0	0	0
Sensel19	0	0	0	0	0	0	0	0
Sensel20	0	0	0	0	0	0	0	0
Sensel21	0	0	0	0	0	1	0.98	0.14
Sensel22	0	0	0	0	0	0	0	0
Sensel23	0	0	0	0	0	0	0	0
Sensel24	0	0	0	0	0	0	0	0
Sensel25	0	0	0	0	0	0	0	0

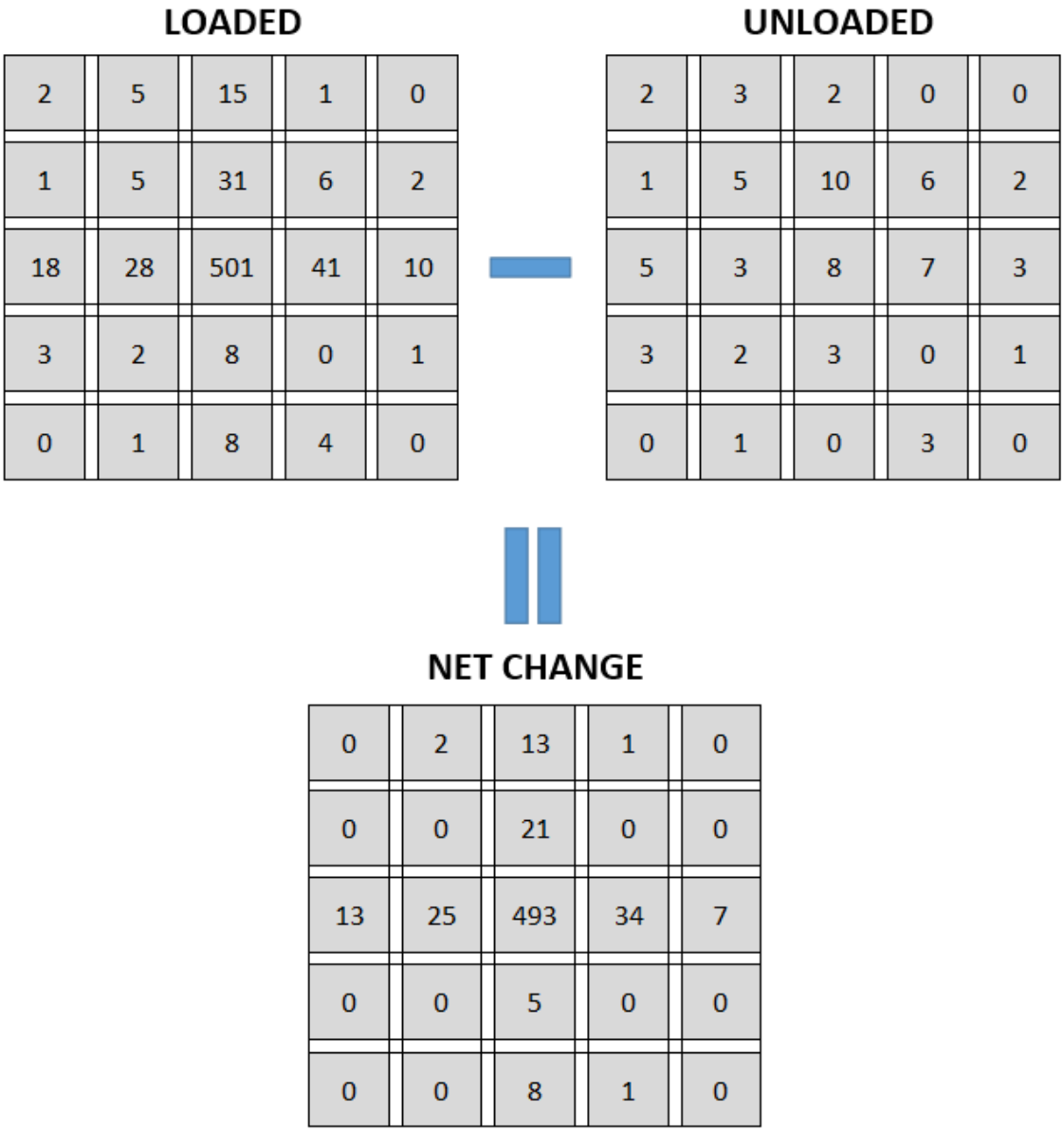

Figure 3.16. Difference between loaded & unloaded states

In this thesis, these operations were carried out through Python 3.10. The effect of each measuring point on the sensor array was recorded as loaded and unloaded, and COP calculations and other analyzes were performed by taking the difference between average values of them as depicted in Figure 3.16. In sections 3.3.1 and 3.3.2, an example COP calculation method of the point 31 is continued.

3.3.1. Finding COPx

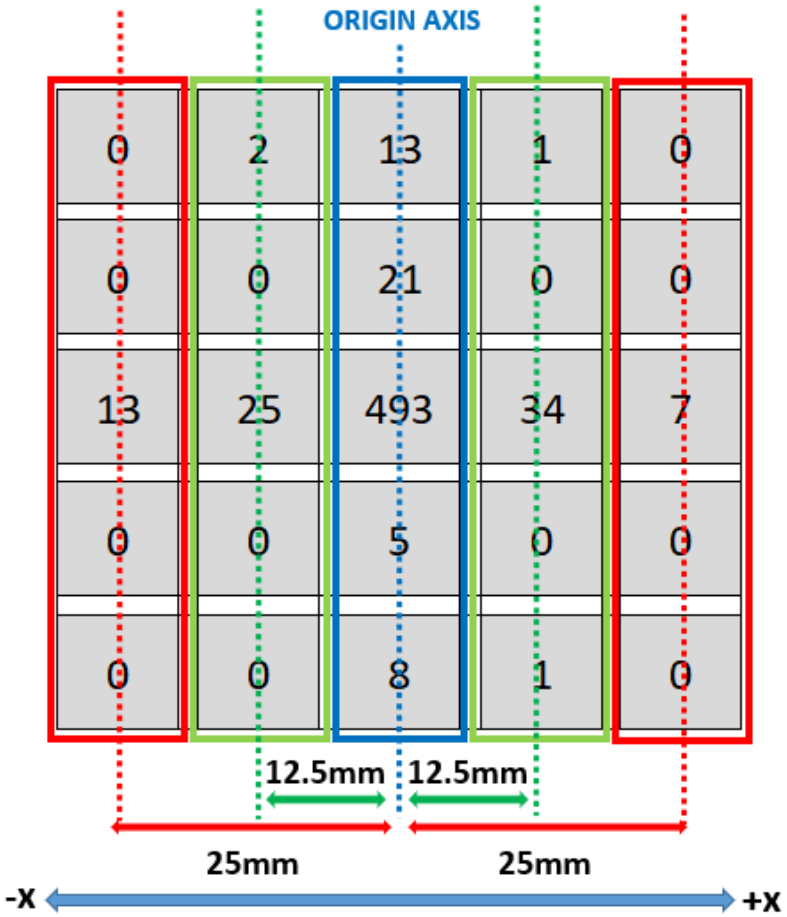

Figure 3.17. Sensel distances wrt origin in x axis

The active sensors can then be used to calculate the COP_x location using the following equation:

$$COP_x = \frac{\sum_1^n S_i \; x \; X_i}{\sum_1^n S_i} \tag{3.1}$$

Where Si is the value of each sensel, n is the number of sensels used in the PRTS, which is equal to 25 in the 5x5 case. Lastly, X_i is the distance from the origin in the x direction. Sensel distances to the origin axis wrt x axis can be seen in Figure 3.17.

3.3.2. Finding COPy

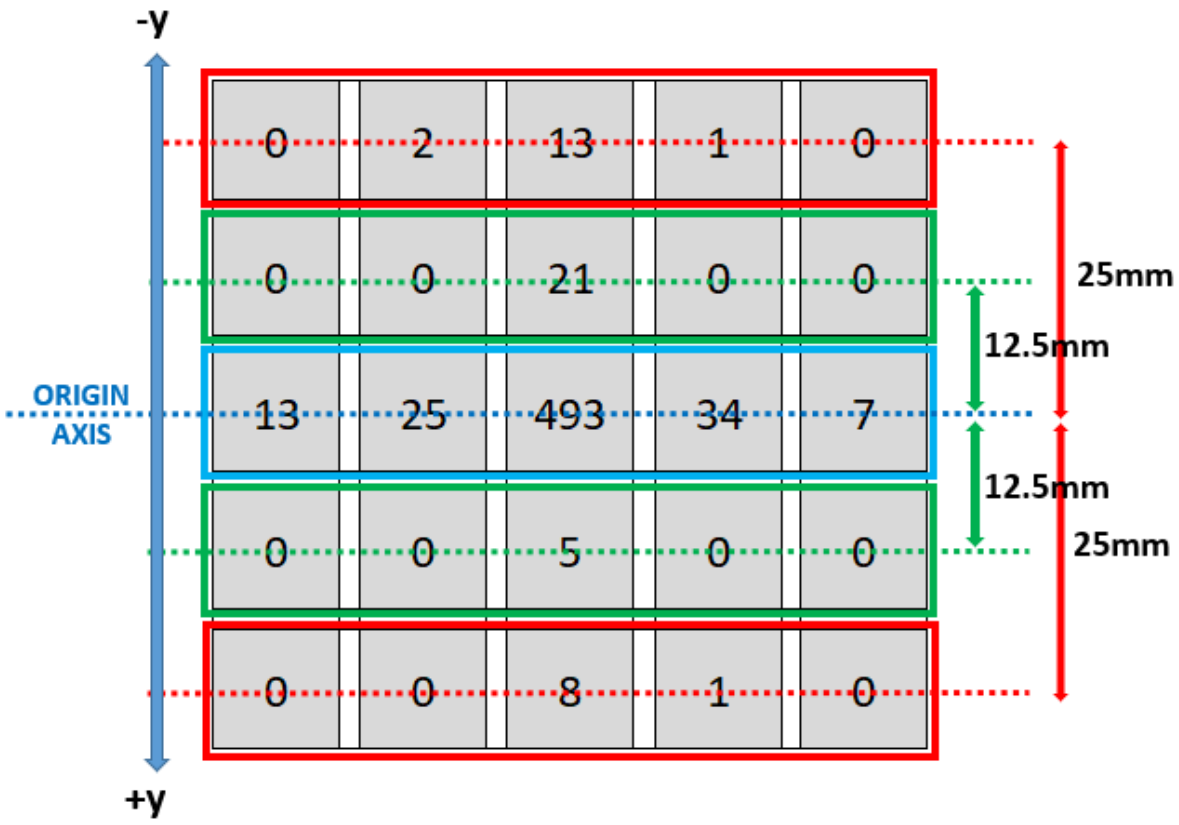

Figure 3.18. Sensel distances wrt origin in y axis

The active sensors can then be used to calculate the COP_x location using the following equation:

$$COP_y = \frac{\sum_1^n S_i \ x \ Y_i}{\sum_1^n S_i} \tag{3.2}$$

Where S_i is the value of each sensel, n is the number of sensels used in the PRTS, which is equal to 25 in the 5x5 case. Lastly, Y_i is the distance from origin in the y direction. Sensel distances to the origin axis wrt y axis can be seen in Figure 3.18.

Therefore according to calculations,

$$COP_x$$

$$= \frac{(0)x(-25) + (2)x(-12{,}5) + (13)x(0) + (1)x(12{,}5) + (0)x(25) + \cdots + (0)x(-25) + (0)x(-12{,}5) + (8)x(0) + (1)x(12{,}5) + (0)x(25)}{0 + 2 + 13 + 1 + 0 + \cdots + 0 + 0 + 8 + 1 + 0}$$

$$= -0.03\ mm$$

$$COP_y$$

$$= \frac{(0)x(25) + (2)x(25) + (13)x(25) + (1)x(25) + (0)x(25) + \cdots + (0)x(-25) + (0)x(-25) + (8)x(-25) + (1)x(-25) + (0)x(-25)}{0 + 2 + 13 + 1 + 0 + \cdots + 0 + 0 + 8 + 1 + 0}$$

$$= 0.3\ mm$$

As can be seen by the results, when a load considered to be homogenous exerts force on the sensor, the position of this force can be read by 25 sensors in the 5x5 case and can be computed by the sensor, together with the error margin. In the usual condition, the sensor system determined the exact location of the position (0, 0) as (-0.03 , 0.3) as depicted in Figure 3.19.

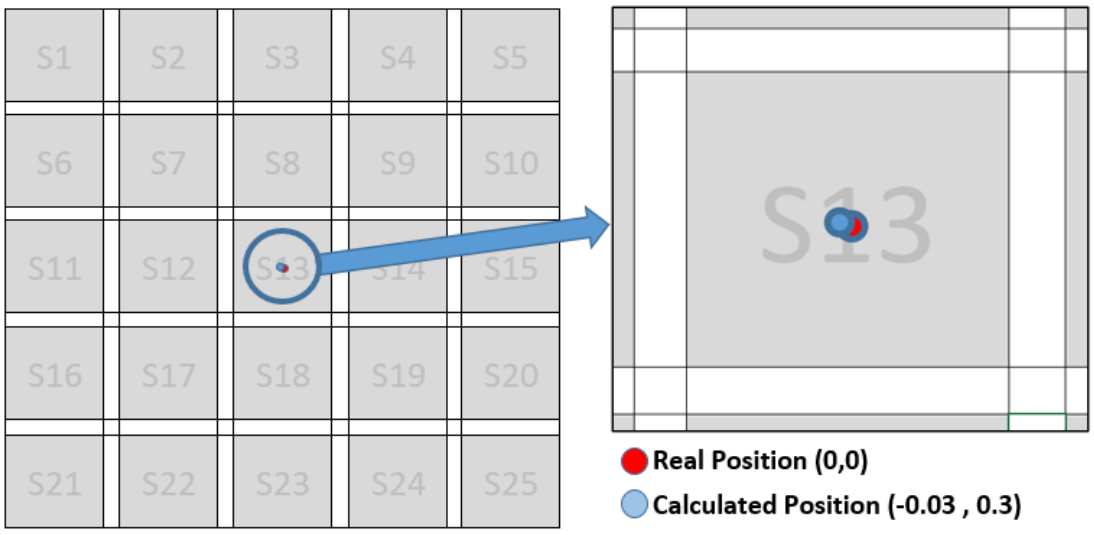

(a) (b)

Figure 3.19. (a) Sensor calculation result of point 31 and (b) zoomed result

3.4. Bias Resistor Selection with Preliminary Experiments

After determining the geometric design of the sensor and the characteristics of the load to be used in the sensor tests, there remains one last parameter to be selected. The issue of what the bias resistor value will be is one of the most important issues in piezoresistive sensor applications. In studies in the literature, this value is chosen to be between 150 Ohms and 10k Ohms. After the sensor decided in the thesis was produced, COP calculations were made using 50 grams of weight with different resistor values. 25 of 61 test points are used for resistor value determination (Figure 3.20).

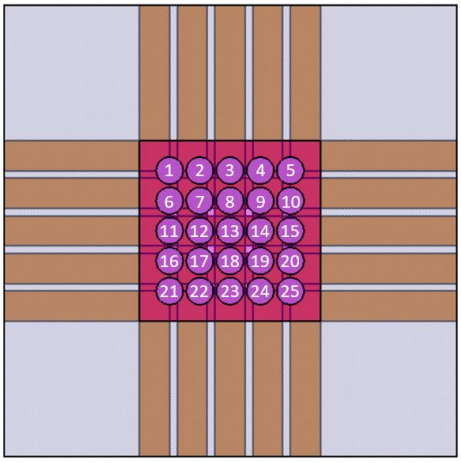

Figure 3.20. Test points for bias resistor determination

In the 5x5 (25 sensels) sensor array system, position error analysis is performed at three different resistance values (Figure 3.21) by placing 50 grams of load at 25 measuring points. Therefore, the performance of the three different bias resistor values tested are evaluated in terms of errors between the measured position and the actual position and the RMSE of the whole system.

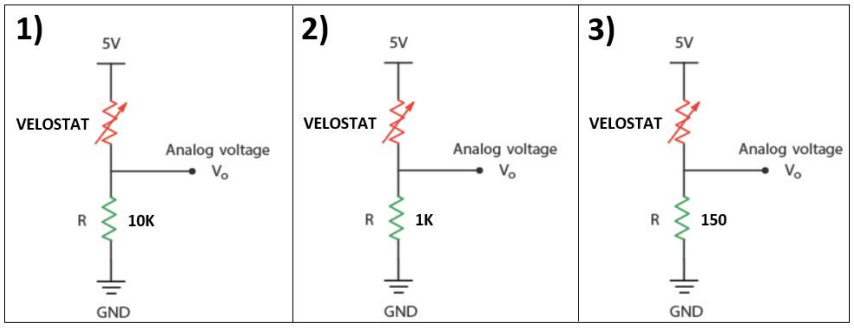

Figure 3.21. Voltage divider circuit with three different resistance values

3.4.1. 10k Ohm Results

In Figure 3.22, the COP values calculated by the sensor using the 10k Ohm resistor can be seen. The points indicated in red are the actual coordinates of the test points, while those indicated in blue are the values calculated by the sensor.

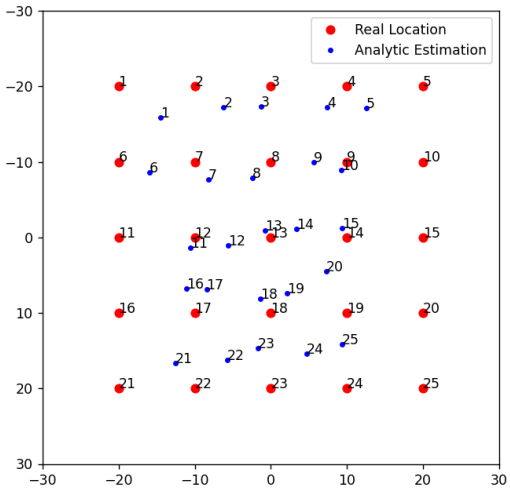

Figure 3.22. 10k Ohm COP results (graphical representation)

In Figure 3.23, the calculated values are presented numerically. The mean error value at 25 points in the system is 6.42 mm. The minimum error is 1.12 mm, the maximum error is 13.84 mm and the RMSE value of the system is 4.79 mm.

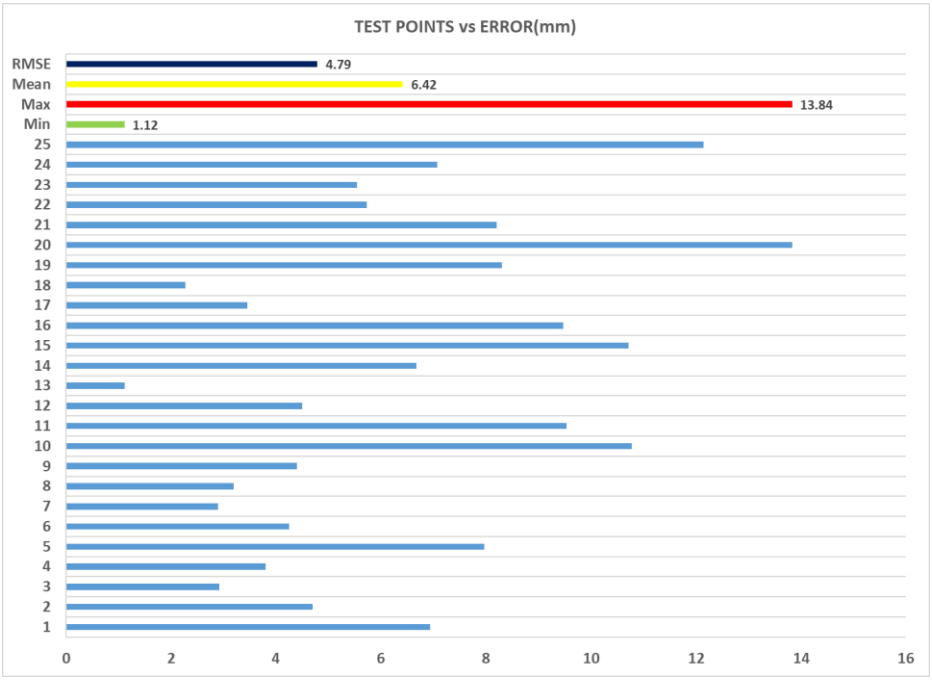

Figure 3.23. 10k Ohm COP results (numerical data)

3.4.2. 1k Ohm Results

Next, in Figure 3.24, the COP values calculated by the sensor using the 1k Ohm resistor can be seen. The points indicated in red are the actual coordinates of the test points, while those indicated in blue are the values calculated by the sensor.

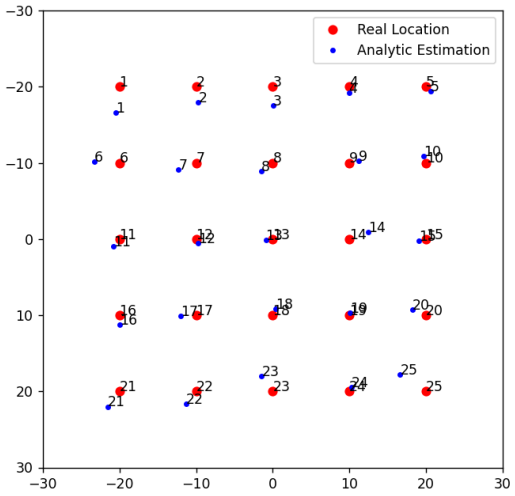

Figure 3.24. 1k Ohm COP results (graphical representation)

In Figure 3.25, the calculated values are presented numerically. The mean error value at 25 points in the system is 1.75 mm. The minimum error is 0.33 mm, the maximum error is 4.04 mm and the RMSE value of the system is 1.42 mm.

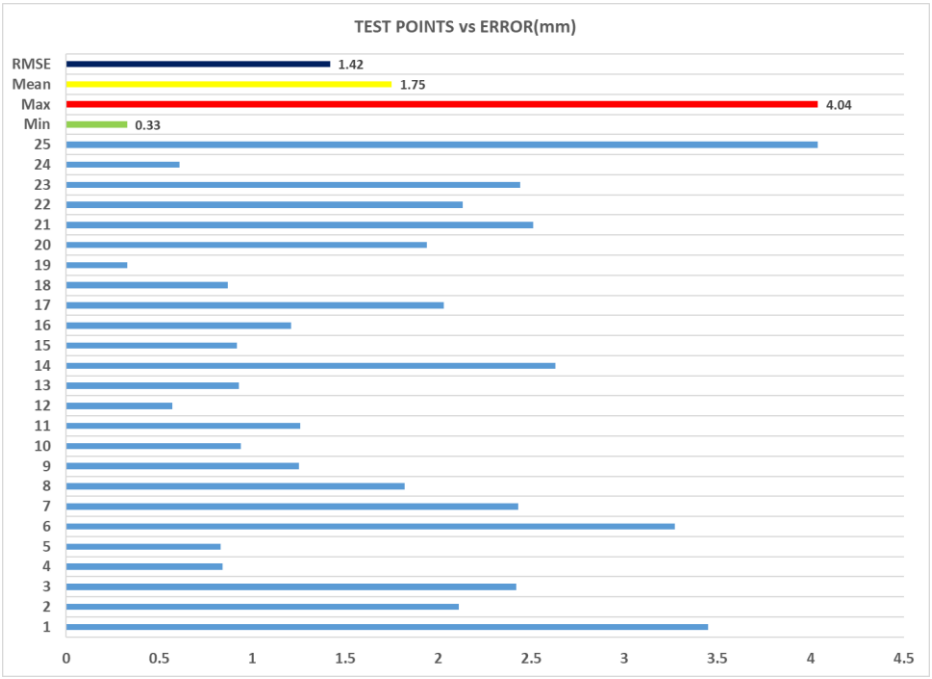

Figure 3.25. 1k Ohm COP results (numerical data)

3.4.3. 150 Ohm Results

Similarly, in Figure 3.26, the COP values calculated by the sensor using the 150 Ohm resistor can be seen. The points indicated in red are the actual coordinates of the test points, while those indicated in blue are the values calculated by the sensor.

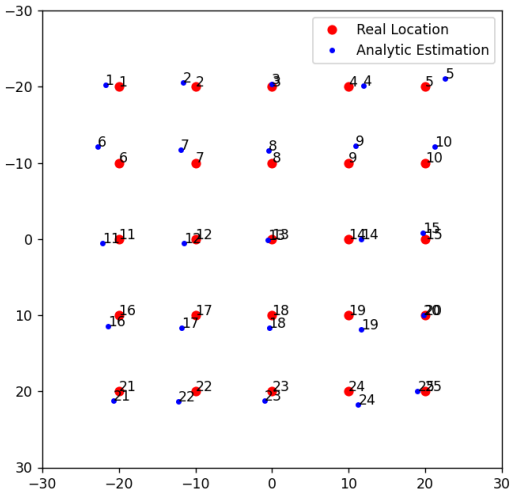

Figure 3.26. 150 Ohm COP results (graphical representation)

In Figure 3.27, the calculated values are presented numerically. The mean error value at 25 points in the system is 1.63 mm. The minimum error is 0.27 mm, the maximum error is 3.46 mm and the RMSE value of the system is 1.4 mm.

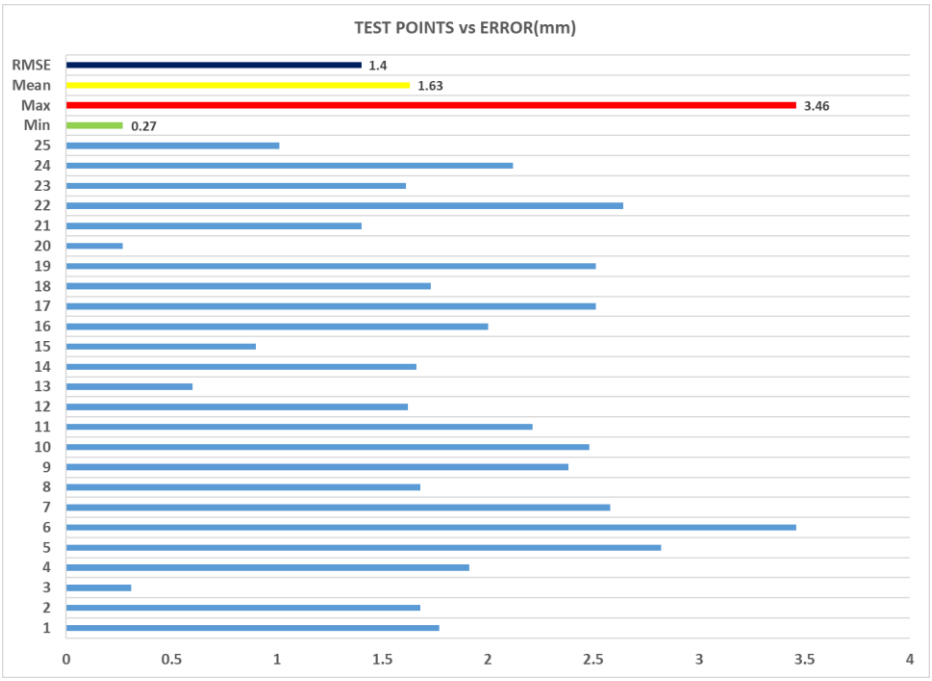

Figure 3.27. 150 Ohm COP results (numerical data)

3.4.4. Comparison of Resistance Performances

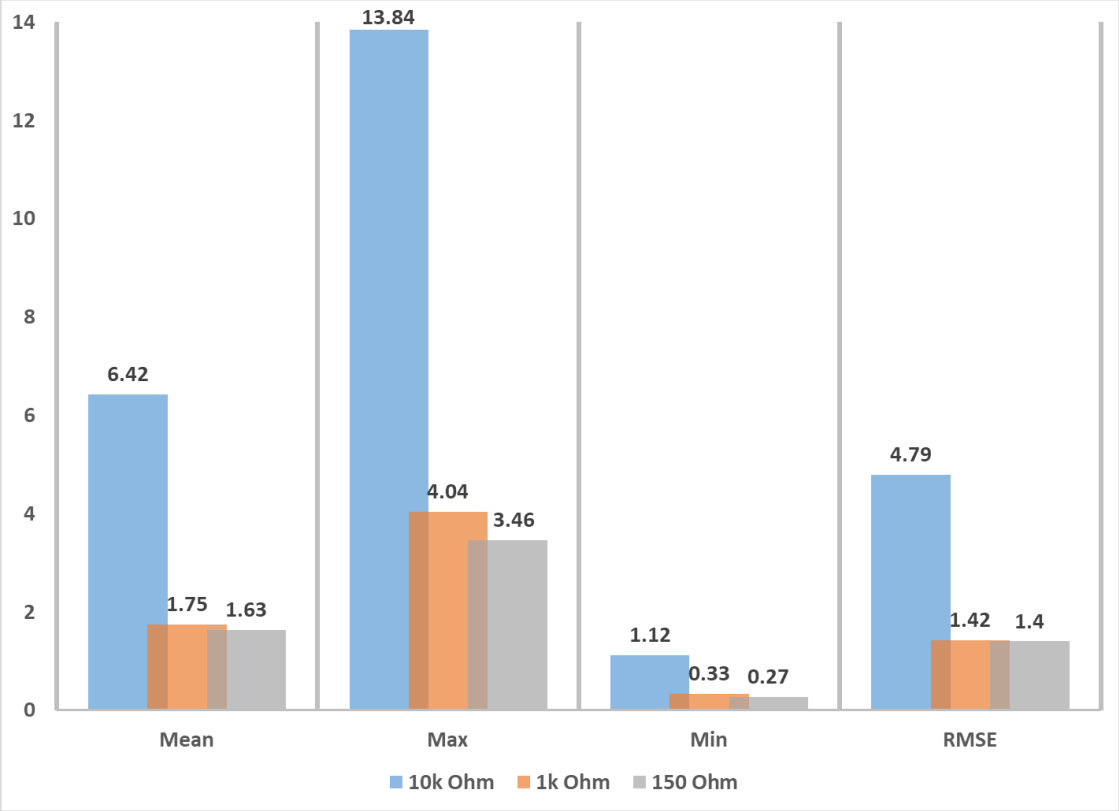

Figure 3.28. COP results of different resistance values

COP analysis is performed at 25 points determined in the 5x5 sensor array assembly, keeping all parameters constant except the bias resistor value. Minimum, maximum, average, and RMSE values of the 25-point system were calculated as depicted in Figure 3.28. When these values are compared with each other, the minimum error result in each value is 150 Ohm. Therefore, in the experimental studies in the thesis, a 150 Ohm value is used as the bias resistor. While the lower resistance value gives better results, the question of whether a value less than 150 Ohm can be chosen, but the 150 Ohm value is the best option in order not to exceed the 40 mA maximum current value offered by the Arduino Mega 2560 MCU.

3.5. Designating Main Experiments and Variations

According to the results obtained in the preliminary experiments, all parameters were determined by selecting the optimum resistance value to be used in the main experiments. However, at this stage, the question arises whether it is possible to improve the COP values. Instead of a single sensor array chosen, the design and construction of sensors in different configurations and the different forces and the extent to which the test results are affected became questionable after these first and preliminary experiments during this thesis study. And in the same 5x5 sensor assembly manufactured in the first stage, the tests of an additional 100 g were carried out at the same 25 points. Again, this new weight is designed in the Catia v5® software and had a contact diameter of 9 mm.

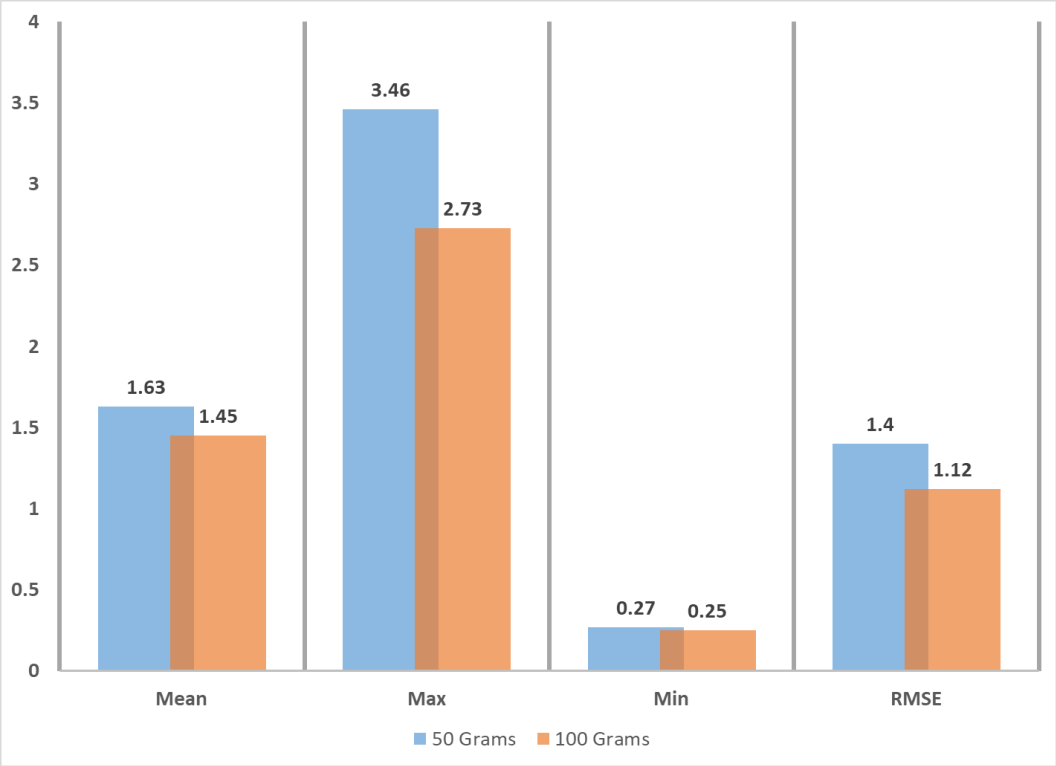

Figure 3.29. 50 g vs 100 g results

As can be seen in Figure 3.29, the measurement results of 100 g were better than all the 50 g measurement results. At this stage, the idea of designing a new sensor array emerged in the main experiments of the thesis study and the idea of using a total of three

different loads (Figure 3.31) in two different sensors, 5x5 and 7x7 sensor array (Figure 3.30), including 150 g of weight, emerged. Thus, more comprehensive and detailed analyzes can be made and it is aimed to obtain richer data in terms of comparison. It should be noted that copper strips passing through the origin are preserved (indicated in red rectangles in Figure 3.30) and by decreasing the distance between the strips the number of sensels is increased. Also, all of the 61 test points are identical on both sensors. In two sensors, 5 measurements are taken from each point for two sensor loads. In total, 305 (61x5) measurements/data values are obtained for each weight. Technical drawings of the sensors are provided in Appendix C, and weight's technical drawings can be found in Appendix B.

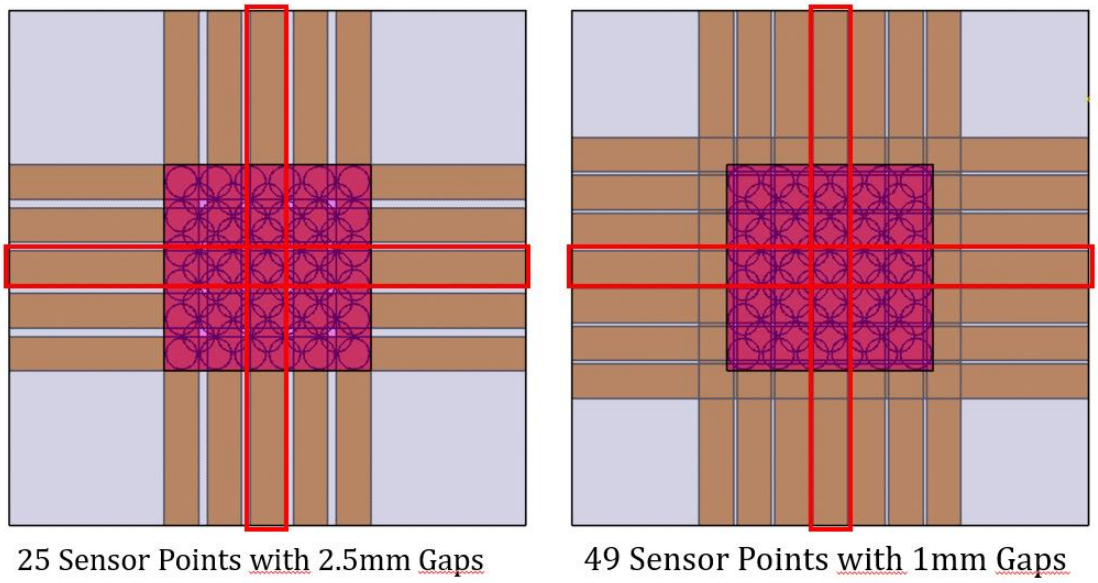

Figure 3.30. 5x5 vs 7x7 sensor array comparison

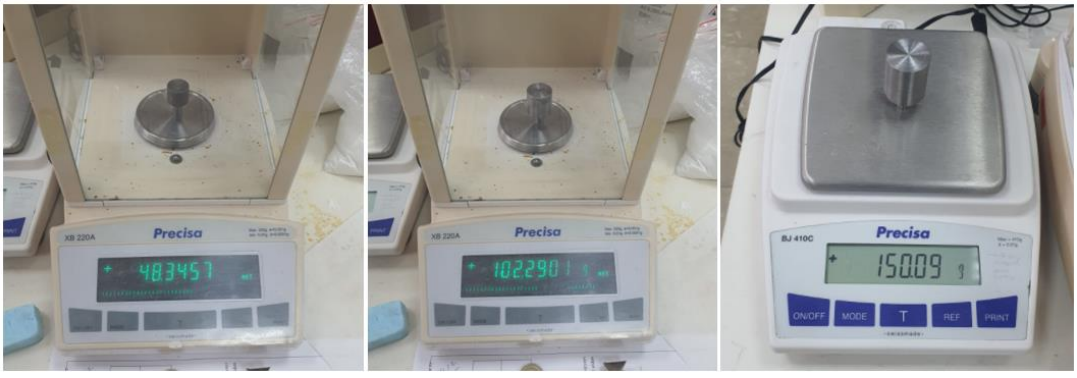

(a) (b) (c)

Figure 3.31. (a) 50 g, (b) 100 g and (c) 150 g

3.5.1. Contact Areas of the 61 Test Points

In Figures 3.32 and 3.33, the contact rate of the test points in the 5x5 and 7x7 sensor displacement to the sensels is given as a percentage, respectively. In Figure 3.34, these values are presented numerically and side by side. The purpose of extracting these values is to investigate the effect of contact areas at these test points on COP errors.

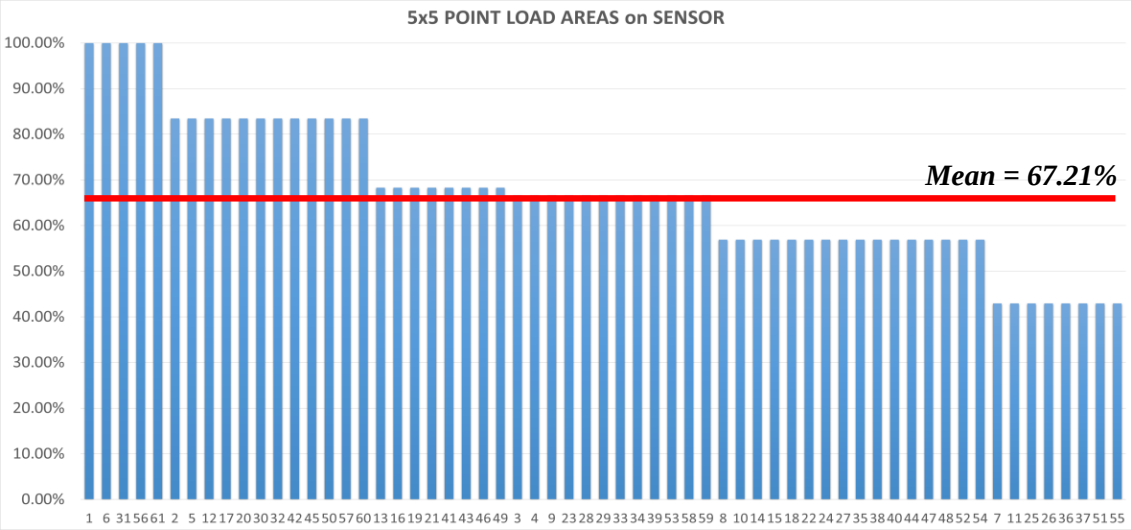

Figure 3.32. Test point's contact areas in 5x5 sensor array

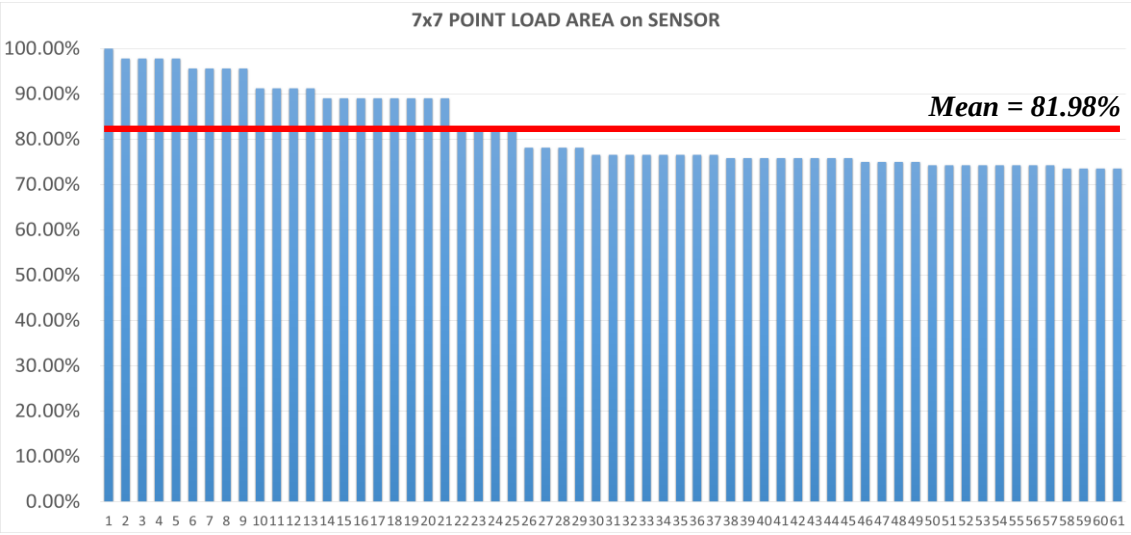

Figure 3.33. Test point's contact areas in 7x7 sensor array

INDEX	5x5	7x7
1	100.00%	78.15%
2	83.45%	76.56%
3	66.55%	75.83%
4	66.55%	75.83%
5	83.45%	76.56%
6	100.00%	78.15%
7	42.92%	82.56%
8	56.90%	89.05%
9	66.55%	91.23%
10	56.90%	89.05%
11	42.92%	82.56%
12	83.45%	76.56%
13	68.28%	74.97%
14	56.90%	74.24%
15	56.90%	74.24%
16	68.28%	74.97%
17	83.45%	76.56%
18	56.90%	89.05%
19	68.28%	95.63%
20	83.45%	97.82%
21	68.28%	95.63%

INDEX	5x5	7x7
22	56.90%	89.05%
23	66.55%	75.83%
24	56.90%	74.24%
25	42.92%	73.51%
26	42.92%	73.51%
27	56.90%	74.24%
28	66.55%	75.83%
29	66.55%	91.23%
30	83.45%	97.82%
31	100.00%	100.00%
32	83.45%	97.82%
33	66.55%	91.23%
34	66.55%	75.83%
35	56.90%	74.24%
36	42.92%	73.51%
37	42.92%	73.51%
38	56.90%	74.24%
39	66.55%	75.83%
40	56.90%	89.05%
41	68.28%	95.63%

INDEX	5x5	7x7
42	83.45%	97.82%
43	68.28%	95.63%
44	56.90%	89.05%
45	83.45%	76.56%
46	68.28%	74.97%
47	56.90%	74.24%
48	56.90%	74.24%
49	68.28%	74.97%
50	83.45%	76.56%
51	42.92%	82.56%
52	56.90%	89.05%
53	66.55%	91.23%
54	56.90%	89.05%
55	42.92%	82.56%
56	100.00%	78.15%
57	83.45%	76.56%
58	66.55%	75.83%
59	66.55%	75.83%
60	83.45%	76.56%
61	100.00%	78.15%

Figure 3.34. Test point's contact area values in 5x5 vs 7x7 sensor arrays

In 48 of the 61 test points, the test load with a diameter of 9 mm touches the sensel regions more in the case of the 7x7 sensor array, and in 13 of them it touches the sensel regions at a higher rate in the case of a 5x5 sensor array (Figure 3.35).

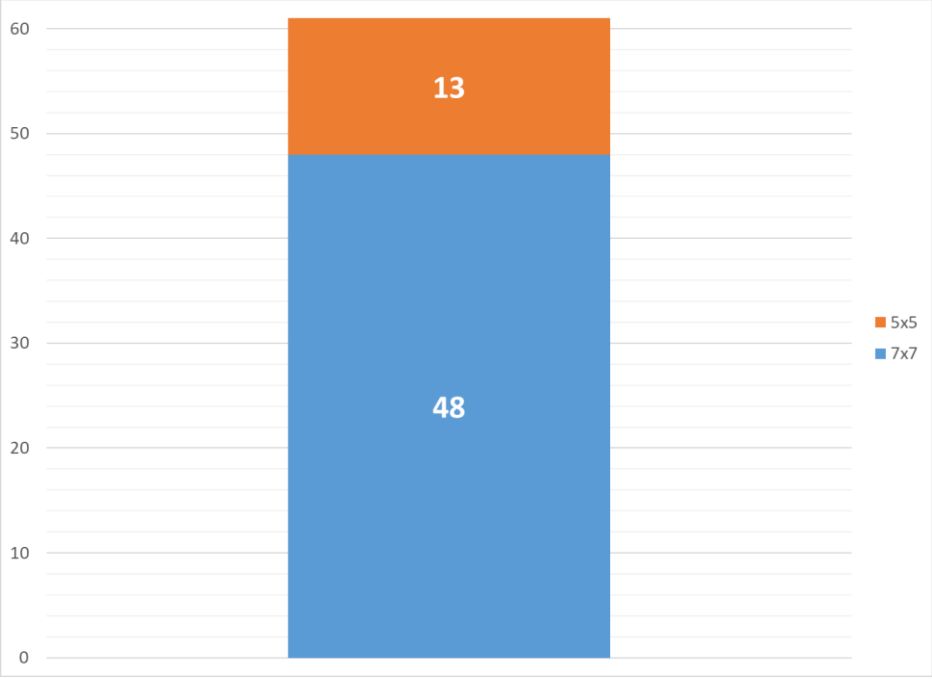

Figure 3.35. 5x5 & 7x7 contact area comparison

3.6. Kadane’s Algorithm Implementation

Ulf Grenander presented the maximum subarray issue for the first time in 1977 as a simple model for maximum likelihood estimation of patterns in digital images [81]. Later, Jay Kadane designed within a minute an O(n)-time algorithm which is as fast as possible [82]. This algorithm is also applicable for 2D subarray problems with $O(n^3)$-time. In numerous disciplines, such as genomic sequence analysis and computer vision, maximum subarray challenges emerge. Utilizing maximal subarray techniques, genomic sequence analysis identifies crucial biological regions of protein sequences [83]. Maximum-subarray techniques are applied to bitmap pictures in computer vision to identify the brightest part of an image [84]. Kadane's technique is a well-known solution to the maximum subarray problem based on dynamic programming. The most difficult aspect of addressing a problem with dynamic programming is locating the optimal subproblems. The maximum subarray problem entails locating the succession of contiguous array elements with the greatest sum.

```
Initialize:
    max_so_far = INT_MIN
    max_ending_here = 0

Loop for each element of the array
  (a) max_ending_here = max_ending_here + a[i]
  (b) if(max_so_far < max_ending_here)
            max_so_far = max_ending_here
  (c) if(max_ending_here < 0)
            max_ending_here = 0
return max_so_far
```

Figure 3.36. Kadane’s algorithm

By looking the algorithm in Figure 3.36, it can be seen that it’s needed to find the maximum subarray sum at every index of the array. Thus, the problem can be divided into n subproblems. It is possible to find the maximum sum at every index by iterating the array only once.

Kadane's Algorithm Example 1D:

For example, in the array shown in Figure 3.37, the colored subarray has the highest sum "6".

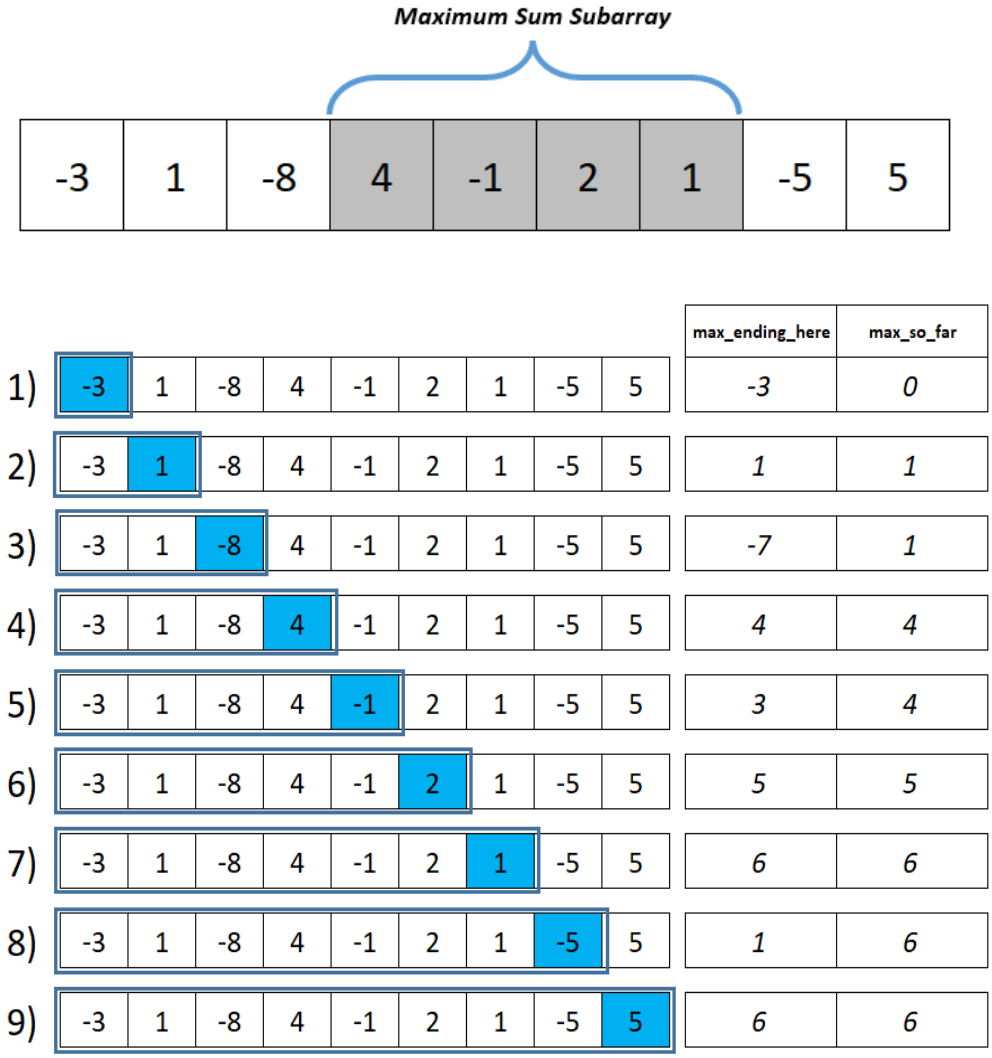

Figure 3.37. Kadane's algorithm 1D example

The highlighted element indicates the iteration's current element. At each index, the previously derived equation will be used to calculate a number for "max_ending_here". This helps us determine whether the current element should be included in the subarray or whether a new subarray should begin at this point. A second variable, "max_so_far", is used to hold the largest subarray sum discovered thus far throughout the loop. Once the last index has been traversed, max so far will contain the total of the maximum subarray. The time complexity of this algorithm is O(n), by brute force it would take $O(n^2)$ because of 2 "for loops".

Kadane's Algorithm Implemantation with Given Subarray Size 2D:

2	**4**	**5**	**6**
2	**3**	**1**	**4**
2	**0**	**2**	**1**

Figure 3.38. Kadane's algorithm 2D array

With Kadane's algorithm, it is possible to obtain maximum sum subarray at any given dimensions. In addition, with a few modifications, the position of the maximum sub array can be taken as output. Let's consider the given 2D array given in Figure 3.38. First, one should create the cumulative sum of the matrix. Cumulative_sum(i,j) is the sum of all the elements in the submatrix (0:i,0:j). One can calculate the cumulative sum matrix using equation 3.3 and the result can be seen in Figure 3.39.

cumulative_sum(i,j) = cumulative_sum(i-1,j) + cumulative_sum(i,j-1) - cumulative_sum(i-1,j-1) + matrix(i,j) (3.3)

2	**6**	**11**	**17**
4	**11**	**17**	**27**
6	**13**	**21**	**32**

Figure 3.39. Cumulative sum matrix

Using the cumulative sum matrix you can calculate sum of every sub-matrix:

calculating sum of submatrix (r1 ... r2 , c1 ... c2)
sum_sub = cumulative_sum(r2,c2) - cumulative_sum(r1-1,c2) - cumulative_sum(r2,c1-1) + cumulative_sum(r1-1,c1-1) (3.4)

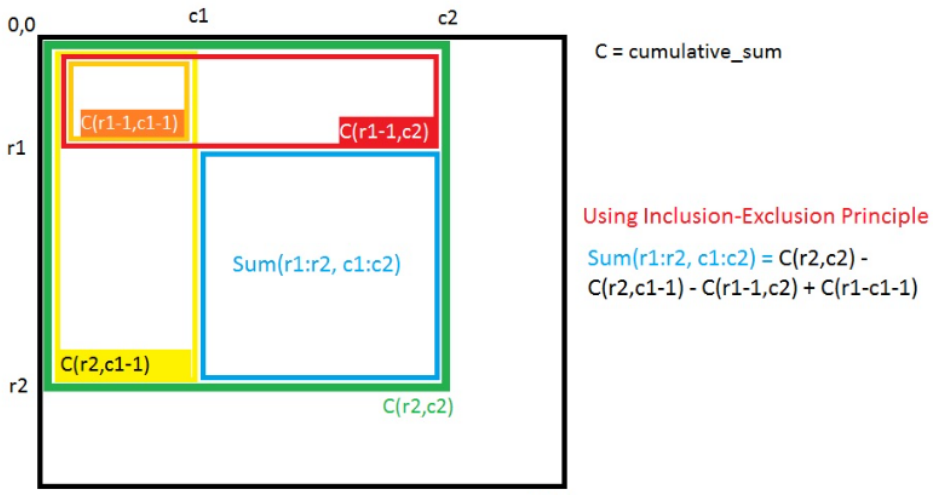

Figure 3.40. Cumulative sum matrix calculation method

Then using two loops one can put the top-left of any size rectangle on every point of the matrix and calculate the sum of that rectangle as depicted in Figure 3.40 and the corresponding algorithm to find the maximum 2D subarray can be seen in Figure 3.41. The time complexity of this algorithm is $O(n^3)$, brute force solution would have a time complexity of $O(n^6)$.

```
for r1=0->n_rows
   for c1=0->n_cols
       r2 = r1 + height - 1
       c2 = c1 + width - 1
       if valid(r1,c1,r2,c2) // doesn't exceed the original matrix
            sum_sub = ... // formula mentioned above
            best = max(sum_sub, best)
return best
```

Figure 3.41. Maximum subarray algorithm

Outputs of the algorithm according to desired subarray size, can be seen in Figure 3.42.

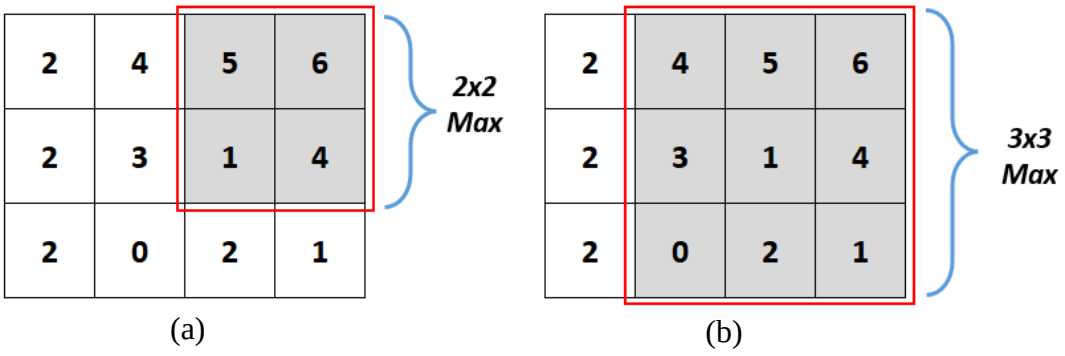

Figure 3.42. Outputs of the algorithm (a) 2x2 subarray and (b) 3x3 subarray

The idea of using this method has arisen from the question of whether there is an alternative solution to the crosstalk problem in piezoresistive sensors. Crosstalk occurs on the sensor in the directions where the current comes from and the voltage values are read. In the literature, there are many studies on this subject and complex circuit solutions are presented with using diodes at every intersection point or using zero voltage circuits [85-88].

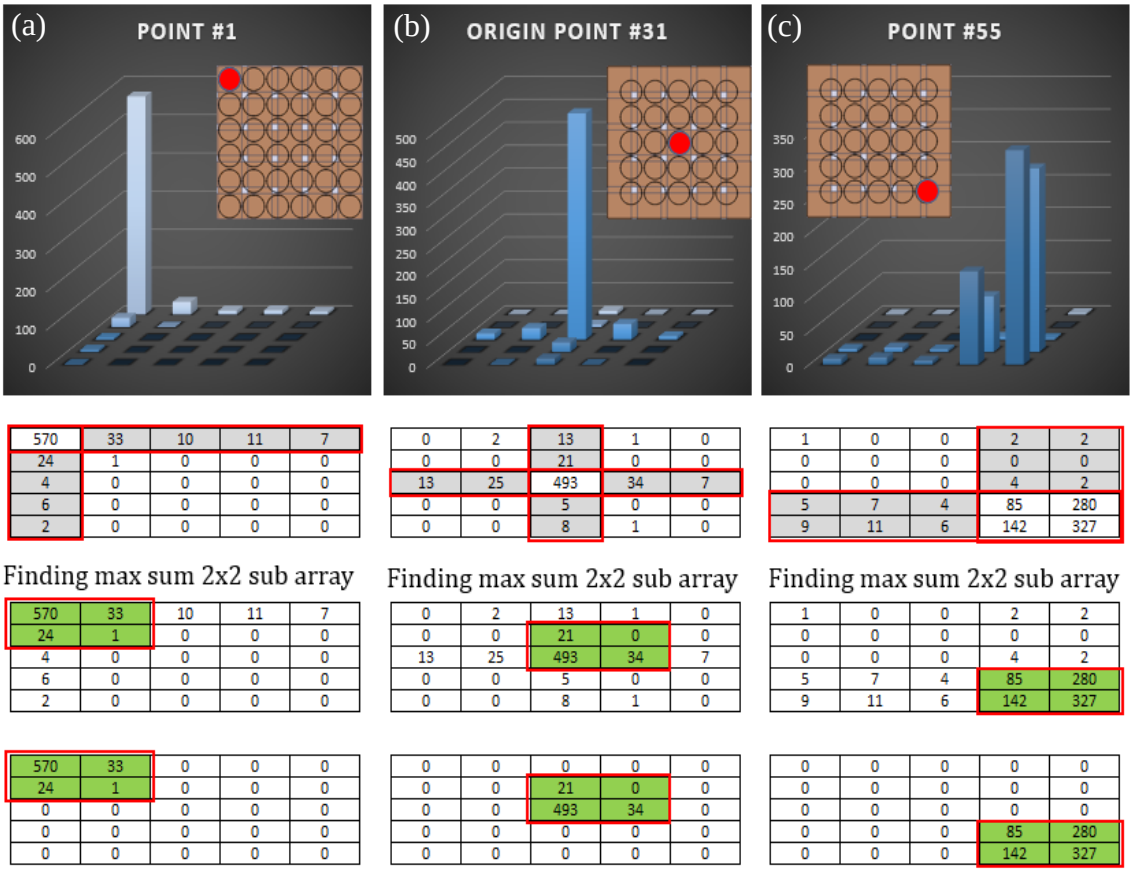

Figure 3.43. Kadane's algorithm implementation examples for the sensor data (a) point 1 , (b) point 31 and (c) point 55

When the load is placed on the test point number 1, that is, directly above the sensel point, the unwanted signals (crosstalk) are indicated in gray cells (Figure 3.43a). Through Kadane's algorithm, one can find the max subarray in desired shape and size. And by equating remaining elements to zero and using this relatively clean matrix in the COP calculations, error can be reduced. Other examples can be seen in Figure 3.43b for point 31and in Figure 3.43c for point 55. In this thesis, it is considered to use and try Kadane's algorithm as a simple but effective method and it aimed to use this algorithm as a noise filter to reduce errors. Further visual representations are provided in Appendix E.

3.7. Least Squares Circle Fit

Circular regression involves finding the "best circle" describing a set of points. In a situation where the data points x, y are distributed in a ring-shape on an x-y plane, the least-squares regression can be used to find the circle equation that best fits the data points. Archaeology, with the problem of megalith circles [89], and geodesy [90] were the initial uses. Circular regression is also utilized for the measurement of geometric flaws in produced items (such as with a three-dimensional measuring machine), specifically circularity and cylindricality [91]. In the literature, there are so many circle fitting algorithms however, least-squares fitting of circles, which works efficiently [92].

The point cloud is given by n points with coordinates x_i, y_i. The aim is to estimate x_c, y_c, and r, the parameters of the circle that fit the best the points where:

- x_c is the x-coordinate of the circle center
- y_c is the y-coordinate of the circle center
- r is the radius of the circle

The equation of the ideal circle is given by:

$$(x_i - x_c)^2 + (y_i - y_c)^2 = r^2 \tag{3.5}$$

The previous equation is rewritten as:

$$x_i{}^2 + x_c{}^2 - 2x_i x_c + y_i{}^2 + y_c{}^2 - 2y_i y_c = r^2 \tag{3.6}$$

then:

$$2x_i x_c + 2y_i y_c + r^2 - y_c{}^2 - x_c{}^2 = x_i{}^2 + y_i{}^2 \tag{3.7}$$

and:

$$ax_i + by_i + c = x_i{}^2 + y_i{}^2 \tag{3.8}$$

where:

$$a = 2x_c\,,\ b = 2y_c,\ c = r^2 - y_c{}^2 - x_c{}^2$$

The whole system(for all the points) can be rewritten as:

$$\begin{aligned} ax_1 + by_1 + c &= {x_1}^2 + {y_1}^2 \\ ax_2 + by_2 + c &= {x_2}^2 + {y_2}^2 \\ &\dots \\ ax_n + by_n + c &= {x_n}^2 + {y_n}^2 \end{aligned} \tag{3.9}$$

The matrix form of the system is given by:

$$\begin{bmatrix} x_1 & y_1 & 1 \\ x_2 & y_2 & 1 \\ \dots & \dots & \dots \\ x_n & y_n & 1 \end{bmatrix} . \begin{bmatrix} a \\ b \\ c \end{bmatrix} = \begin{bmatrix} {x_1}^2 + {y_1}^2 \\ {x_2}^2 + {y_2}^2 \\ {x_n}^2 + {y_n}^2 \end{bmatrix} \tag{3.10}$$

Let's define A,B and X:

$$A = \begin{bmatrix} x_1 & y_1 & 1 \\ x_2 & y_2 & 1 \\ \dots & \dots & \dots \\ x_n & y_n & 1 \end{bmatrix}, \qquad X = \begin{bmatrix} a \\ b \\ c \end{bmatrix}, \qquad B = \begin{bmatrix} {x_1}^2 + {y_1}^2 \\ {x_2}^2 + {y_2}^2 \\ {x_n}^2 + {y_n}^2 \end{bmatrix}$$

The system is now given by:

$$A.X = B \tag{3.11}$$

The optimal solution is given by:

$$\hat{x} = A^{+}.B = A^{T}(A.A^{T})^{-1}.B \tag{3.12}$$

Where A^{+} is the pseudoinverse of A. It can be computed with the following formula:

$$A^{+} = A^{T}(A.A^{T})^{-1} \tag{3.13}$$

As there has been a change of variables, it only remains to calculate x_c, y_c and r:

$$x_c = \frac{a}{2}, \; y_c = \frac{b}{2} \; and \; r = \frac{\sqrt{4c + a^2 + b^2}}{2}$$

And one can get the parameters of the circle as shown in Figure 3.44:

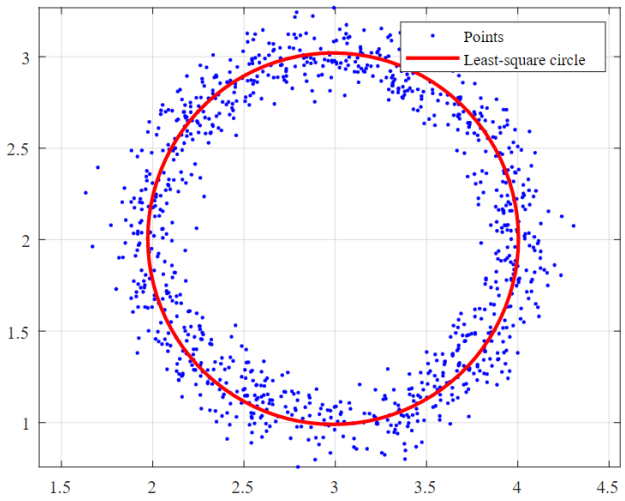

Figure 3.44. Circle fit example

In this thesis, the idea of applying this method emerged from the goal of observing how far the center of the theoretical circle formed by 305 measuring points is from the point of origin (0,0). Since the 61 test points are located symmetrically around the origin, it is thought that the proximity of the circle center formed by the 305 measurement results to the origin can be concluded that the active measuring area of the sensor works relatively homogeneously. In other words, it is intended to discover that the theoretical circle center formed by all measurements in the system does not constantly slip in a certain direction. An example from this thesis can be seen in Figure 3.45.

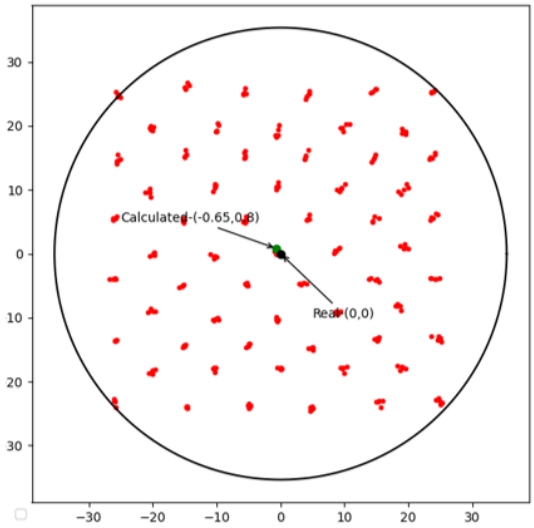

Figure 3.45. Circle fit method implementation for the sensor measurements

3.8. Multivariate Linear Regression

Multivariate linear regression is used to investigate the relationship between a dependent variable and multiple independent variables. The structure of the multiple regression equation is $\hat{y} = a + b_1x_1 + b_2x_2 + \ldots + b_kx_k$. The true relationship between multiple variables is described by $\hat{y} = a + b_1x_1 + b_2x_2 + \ldots + b_kx_k + e$, where e is the error term. The idealized equation that describes the true regression model is $\hat{y} = a + b_1x_1 + b_2x_2 + \ldots + b_kx_k$. Coefficients in multiple regression characterize relationships that are net with respect to the independent variables included in the model but gross with respect to all omitted independent variables. Forecasting with a multiple regression equation is similar to forecasting with a single variable linear model. However, instead of entering only one value for a single independent variable such as in section 3.7, this time more variables are used as input values for each of the independent variables.

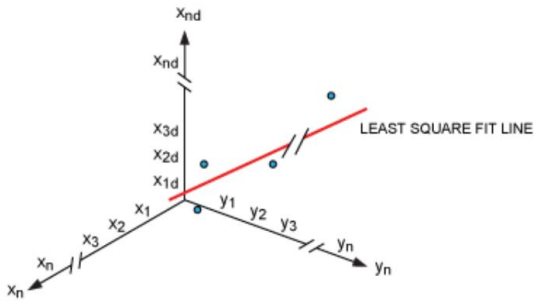

Figure 3.46. Multivariate linear regression method

A generalized form of the sets of equations will look like the following:

$$\begin{aligned} x_{1d} &= x_1 A + y_1 B + C \\ x_{2d} &= x_2 A + y_2 B + C \\ x_{3d} &= x_3 A + y_3 B + C \\ &\ldots \\ x_{nd} &= x_n A + y_n B + C \end{aligned} \tag{3.14}$$

$$\begin{aligned} y_{1d} &= x_1 D + y_1 E + F \\ y_{2d} &= x_2 D + y_2 E + F \\ y_{3d} &= x_3 D + y_3 E + F \\ &\ldots \\ y_{nd} &= y_n D + y_3 E + F \end{aligned} \tag{3.15}$$

Where, $(x_{1d}, y_{1d})...(x_{nd}, y_{nd})$ are coordinates calculated by the sensor; $(x_1, y_1)...(x_n, y_n)$ are the real coordinate values (for n points) as depicted in Figure 3.46. The goal is to determine the coefficients using these values. In the equation 3.14 and 3.15 there are three unknowns, A, B, and C, but the set of coordinates is more than three. This implies that there are more equations than unknowns. Therefore, in this instance it makes sense to use the least square fit to utilize all the points and derive an average value of the coefficients. This also means that more test points would help lower errors. The least square fit is represented in Figure. The same technique will be applied for determining the unknowns D, E, and F for the y values.

Equation sets 3.14 and 3.15 can be written in matrix form, as shown:

$$\begin{bmatrix} x_{1d} \\ x_{2d} \\ x_{3d} \\ \dots \\ x_{nd} \end{bmatrix} = Z \times \begin{bmatrix} A \\ B \\ C \end{bmatrix} \qquad \begin{bmatrix} y_{1d} \\ y_{2d} \\ y_{3d} \\ \dots \\ y_{nd} \end{bmatrix} = Z \times \begin{bmatrix} D \\ E \\ F \end{bmatrix} \qquad \text{Where, } Z = \begin{bmatrix} x_1 & y_1 & 1 \\ x_2 & y_2 & 1 \\ x_3 & y_3 & 1 \\ \dots & & \\ x_{nd} & y_{nd} & 1 \end{bmatrix}$$

By using the least square fit in this matrix form as in the section 3.7, the coefficients are given by the equations below:

$$\begin{bmatrix} A \\ B \\ C \end{bmatrix} = (Z^T \times Z)^{-1} \times Z^T \begin{bmatrix} x_{1d} \\ x_{2d} \\ x_{3d} \\ \dots \\ x_{nd} \end{bmatrix} \quad (3.16) \qquad \begin{bmatrix} D \\ E \\ F \end{bmatrix} = (Z^T \times Z)^{-1} \times Z^T \begin{bmatrix} y_{1d} \\ y_{2d} \\ y_{3d} \\ \dots \\ y_{nd} \end{bmatrix} \quad (3.17)$$

The idea of using this method in this thesis emerged as a result of researching studies in the literature. Most resistive touch systems require a calibration step as one of the first steps in integration because proper calibration is important for touch accuracy [93]. With the 3, 5, 9, 16 and 25 point options, the regression equation obtained from these points improves the position accuracy of the system. In this thesis, 36 of the 61 test points in both 5x5 and 7x7 sensor array systems were determined as a kind of calibration point and tested with the values of the remaining 25 points. The aim here is to estimate the errors of the 25 tested points calculated by the system through 36 training points.

CHAPTER 4

RESULTS AND DISCUSSION

In this chapter, the results of all the analysis and tests of two different meshed sensors under three different weights in this thesis are presented in detail.

4.1. 5x5 Sensor Array COP Results

4.1.1. 50 g

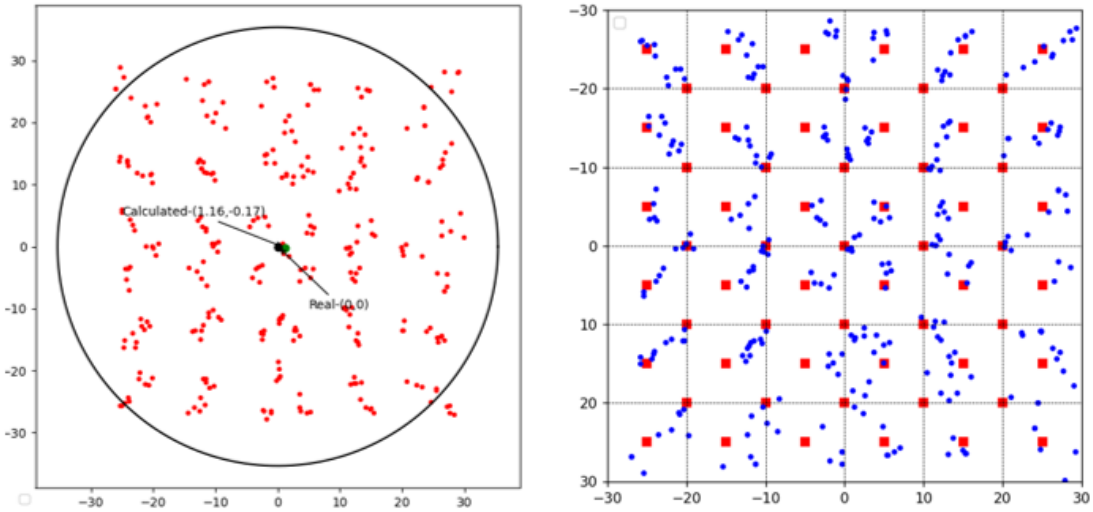

(a) (b)

Figure 4.1. 50 g results (5x5) (a) center of data points and (b) COP measurements

The first results are obtained according to the data collected with a weight of 50 g at 61 measuring points determined in a 5x5 sensor array. In Figure 4.1a, the circle center formed by a total of 305 points obtained as a result of 5 measurements taken from each point is seen. In this graph, the red dots are the result cloud of the 305 points measured. In Figure 4.1b, the points indicated by the red squares are the actual coordinates of the test points. Blue circles are the results obtained from the sensor data. The circle center formed by 305 measurements came out of the origin with a offset of 1.16 mm in the x axis and 0.17 mm in the y axis. In COP analyses, the mean error in 305 measurement results are found as 2.31 mm, the largest error as 7.63 mm, the smallest error as 0.12 mm and finally the RMSE value of the system as 1.84 mm.

4.1.2. 100 g

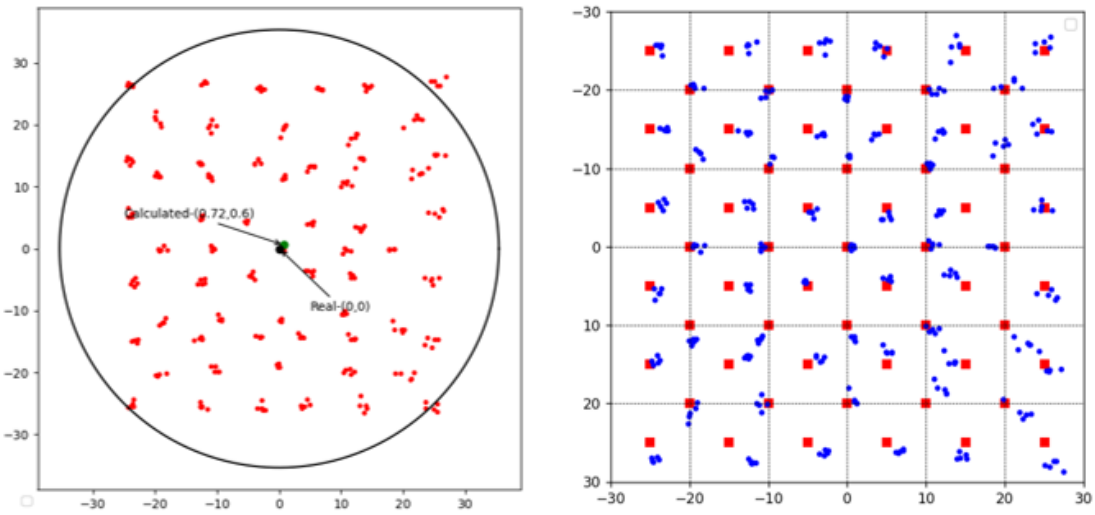

(a) (b)

Figure 4.2. 100 g results (5x5) (a) center of data points and (b) COP measurements

Results in this section are obtained according to the data collected with a weight of 100 g at same 61 measuring points determined in a 5x5 sensor array. The circle center formed by 305 measurements came out of the origin point with a offset of 0.72 mm in the x axis and 0.6 mm in the y axis (Figure 4.2a). In COP analyses, the mean error in 305 measurement results are found as 1.69 mm, the largest error as 4.15 mm, the smallest error as 0.05 mm and finally the RMSE value of the system as 1.32 mm (Figure 4.2b).

4.1.3. 150 g

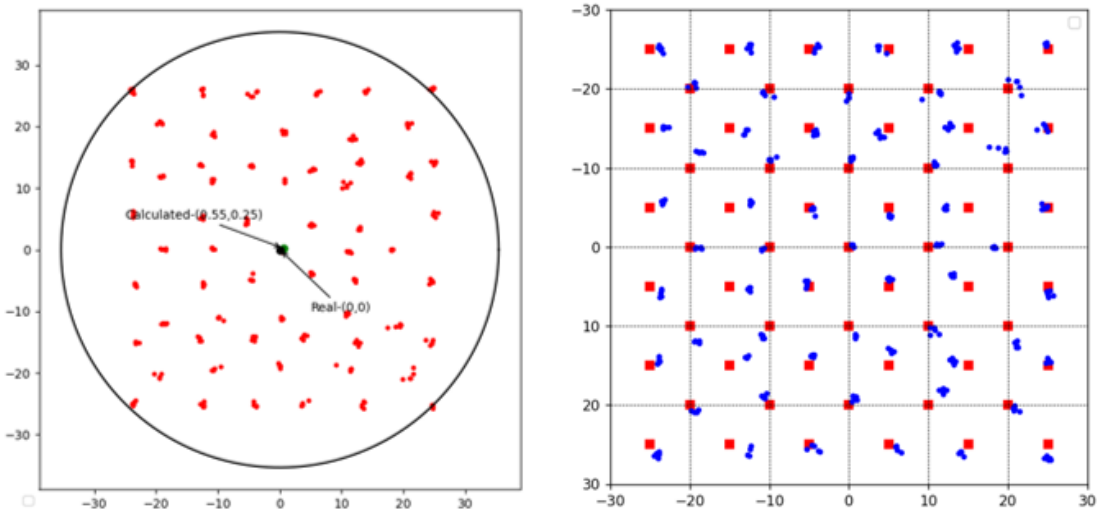

(a) (b)

Figure 4.3. 150 g results (5x5) (a) center of data points and (b) COP measurements

Similarly, the circle center formed by 305 measurements came out of the origin point with a offset of 0.55 mm in the x axis and 0.25 mm in the y axis (Figure 4.3a). In COP analyses, the mean error in 305 measurement results are found as 1.49 mm, the largest error as 3.73 mm, the smallest error as 0.12 mm and finally the RMSE value of the system as 1.15 mm (Figure 4.3b).

According to the circle fit results, the circle center offset obtained from the measurement results of 3 different weights, minimum error is obtained for 150 g as euclidean distance as depicted in Figure 4.4.

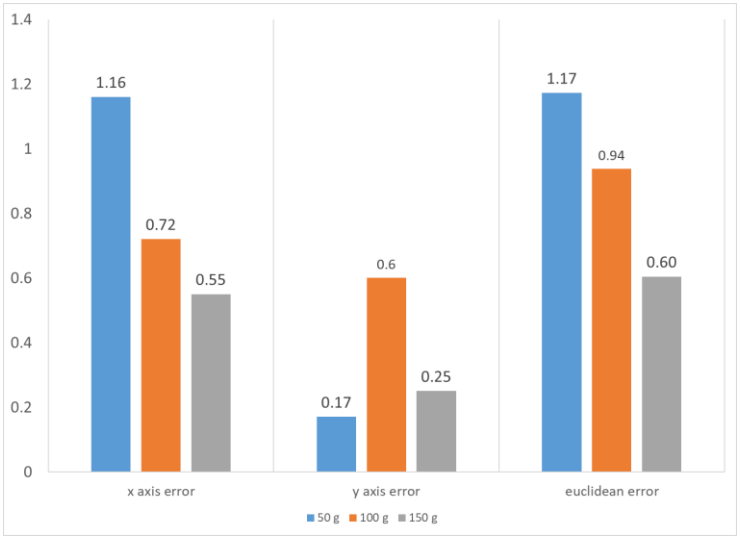

Figure 4.4. Circle fit results for 5x5 sensor array

The COP results in the 5x5 sensor array are shared in Figure 4.5. Accordingly, the minimum errors were similar for three different weights, but the maximum error, average error and RSME values decreased in parallel with the weight increase.

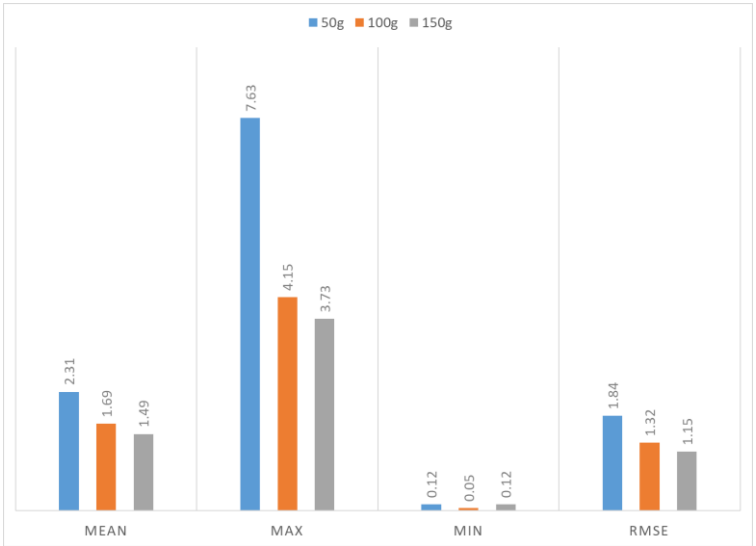

Figure 4.5. COP results comparison wrt different weights (5x5)

4.2. 7x7 Sensor Array COP Results

4.2.1. 50 g

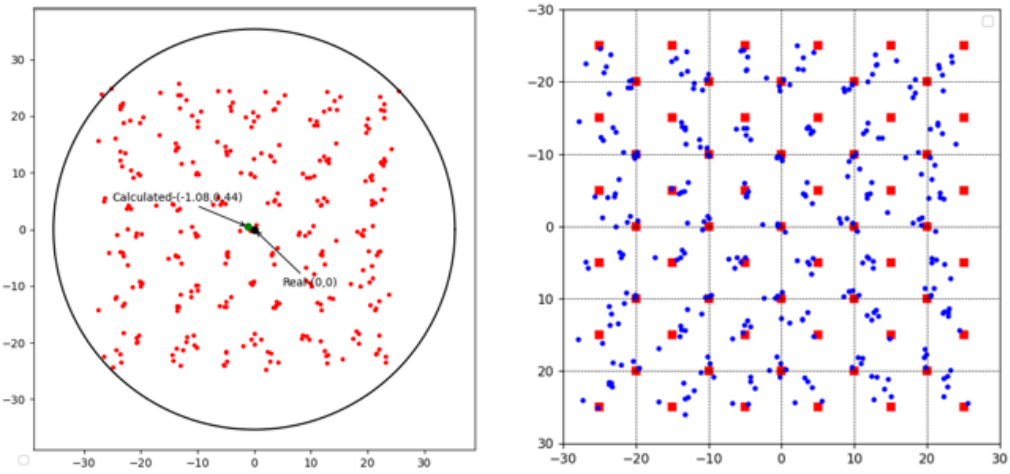

(a) (b)

Figure 4.6. 50 g results (7x7) (a) center of data points and (b) COP measurements

In this section, results are obtained according to the data collected with a weight of 50 g at 61 measuring points determined in a 7x7 sensor array. The circle center formed by 305 measurements came out of the origin point with a offset of 1.08 mm in the x axis and 0.44 mm in the y axis (Figure 4.6a). In COP analyses, the mean error in 305 measurement results are found as 2.12 mm, the largest error as 5.11 mm, the smallest error as 0.07 mm and finally the RMSE value of the system as 1.72 mm (Figure 4.6b).

4.2.2. 100 g

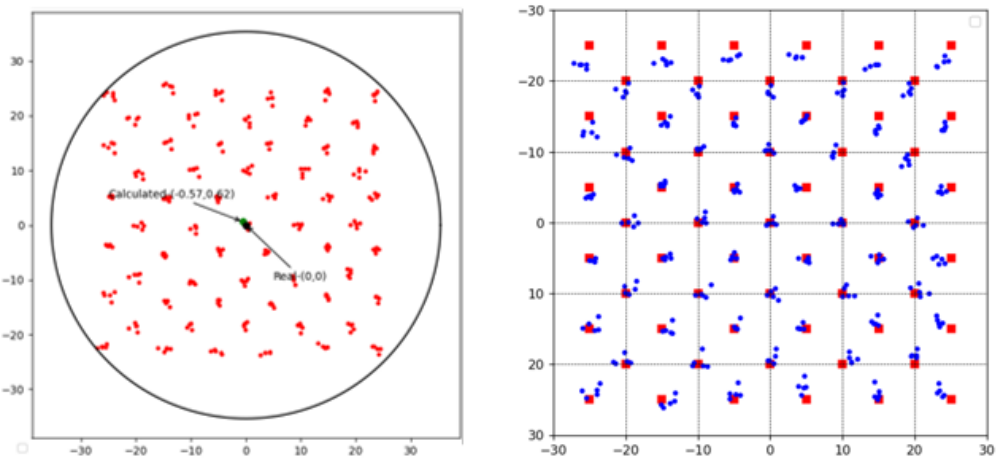

(a) (b)

Figure 4.7. 100 g results (7x7) (a) center of data points and (b) COP measurements

Similarly, the circle center formed by 305 measurements came out of the origin point with a offset of 0.57 mm in the x axis and 0.62 mm in the y axis (Figure 4.7a). In COP analyses, the mean error in 305 measurement results are found as 1.3 mm, the largest error as 3.88 mm, the smallest error as 0.12 mm and finally the RMSE value of the system as 1.05 mm (Figure 4.7b).

4.2.3. 150 g

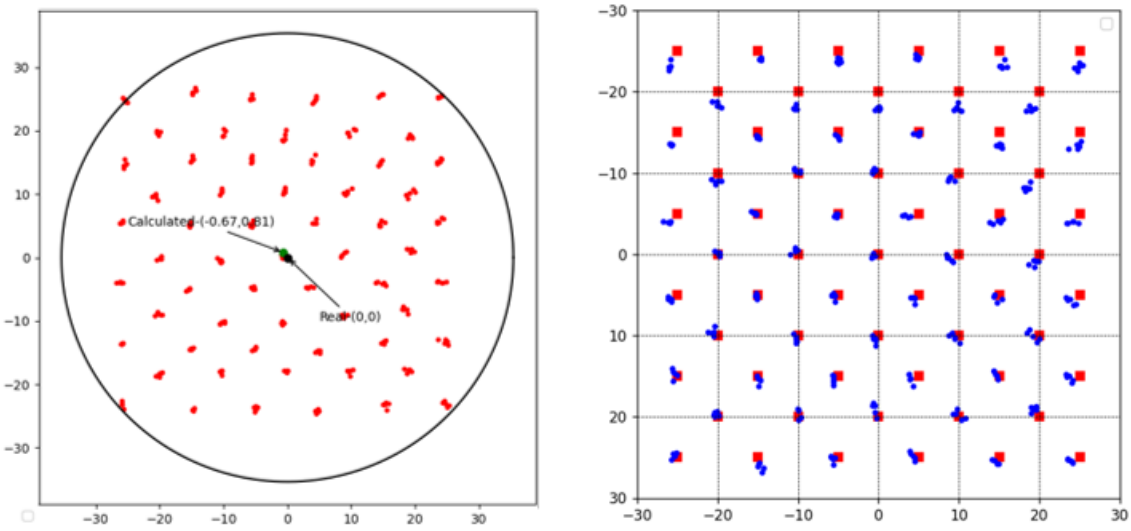

(a) (b)

Figure 4.8. 150 g results (7x7) (a) center of data points and (b) COP measurements

Lastly, the circle center formed by 305 measurements came out of the origin point with a offset of 0.67 mm in the x axis and 0.81 mm in the y axis (Figure 4.8a). In COP analyses, the mean error in 305 measurement results are found as 1.12 mm, the largest error as 2.98 mm, the smallest error as 0.06 mm and finally the RMSE value of the system as 0.89 mm (Figure 4.8b).

According to the circle fit results, the circle center offset obtained from the measurement results of 3 different weights, minimum error is obtained for 100 g as euclidean distance as depicted in Figure 4.9. Although, results are similar to each other, results of 100 g is slightly better.

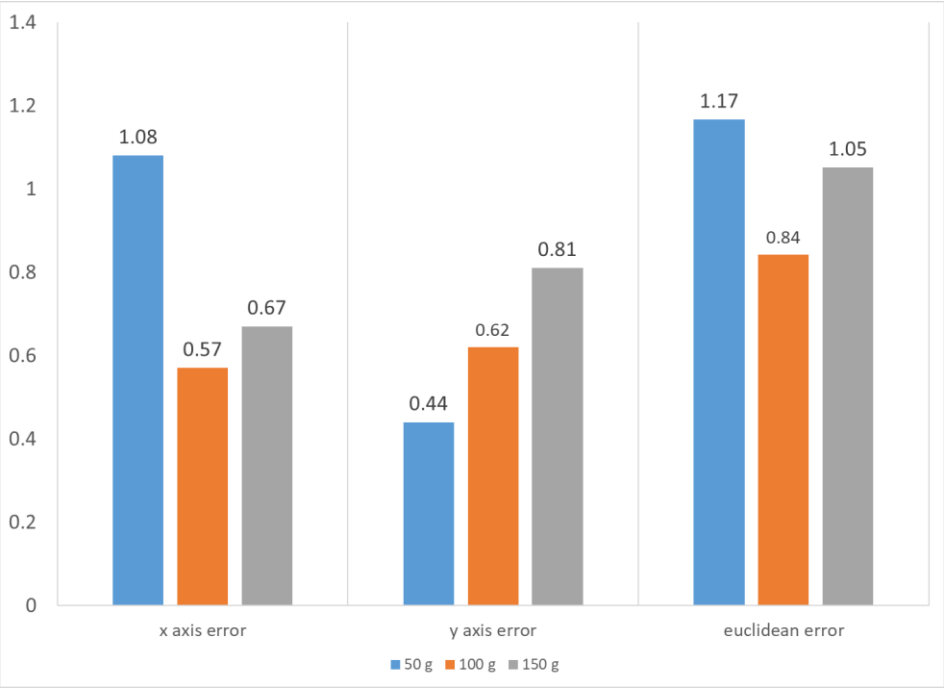

Figure 4.9. Circle fit results for 7x7 sensor array

The COP results in the 7x7 sensor array are shared in Figure 4.10. Accordingly, in this case, the minimum error, the maximum error, average error and RSME values decreased in parallel with the weight increase.

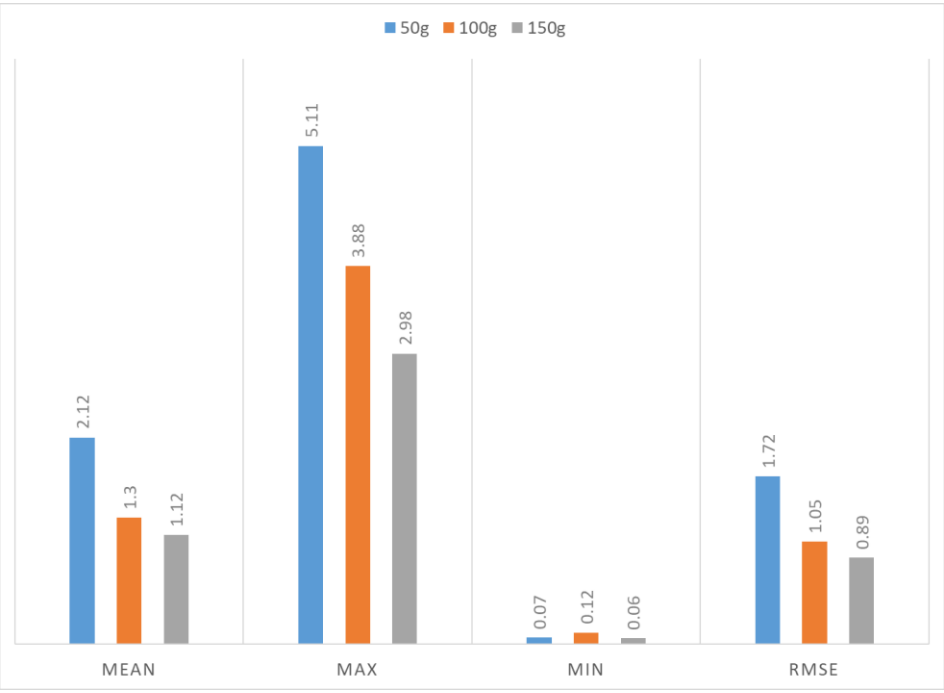

Figure 4.10. COP results comparison wrt different weights (7x7)

4.3. Improved Results with Kadane's Algorithm

In this section, the results of the maximum sum subarray finding method recommended in section 3.6 are shared comparatively.

4.3.1. 5x5 Results

4.3.1.1. 50 g

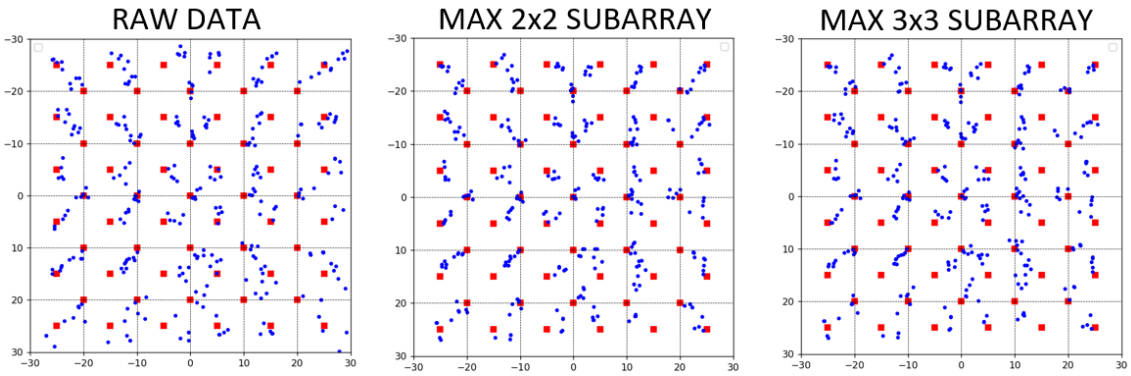

Figure 4.11. 5x5 COP results comparison for 50 g (a) raw data, (b) max 2x2 subarray and (c) max 3x3 subarray

In this section, the COP values obtained by taking all the values in 25 sensels (Figure 4.11a) of the load placed on the sensor, taking only 4 sensel values (Figure 4.11b) and using 9 sensel values (Figure 4.11c) are shared comparatively. The results obtained by using 2x2 and 3x3 maximum sum subarray values are lower than the results obtained by using raw data. The lowest error values are obtained with 2x2 subarray values. An improvement of 0.42 mm is achieved in the mean error and 0.32 mm in the RMSE value of the system. The percentage reduction of errors is presented in Table 4.1.

Table 4.1. Error change with Kadane's algorithm for 50 g (5x5)

50 g	Raw Data	2x2 Subarray	% Change
Mean Error	2.31	1.89	-18.2%
Max Error	7.63	5.42	-29.0%
Min Error	0.12	0.08	-33.3%
RMSE	1.84	1.52	-17.4%

4.3.1.2. 100 g

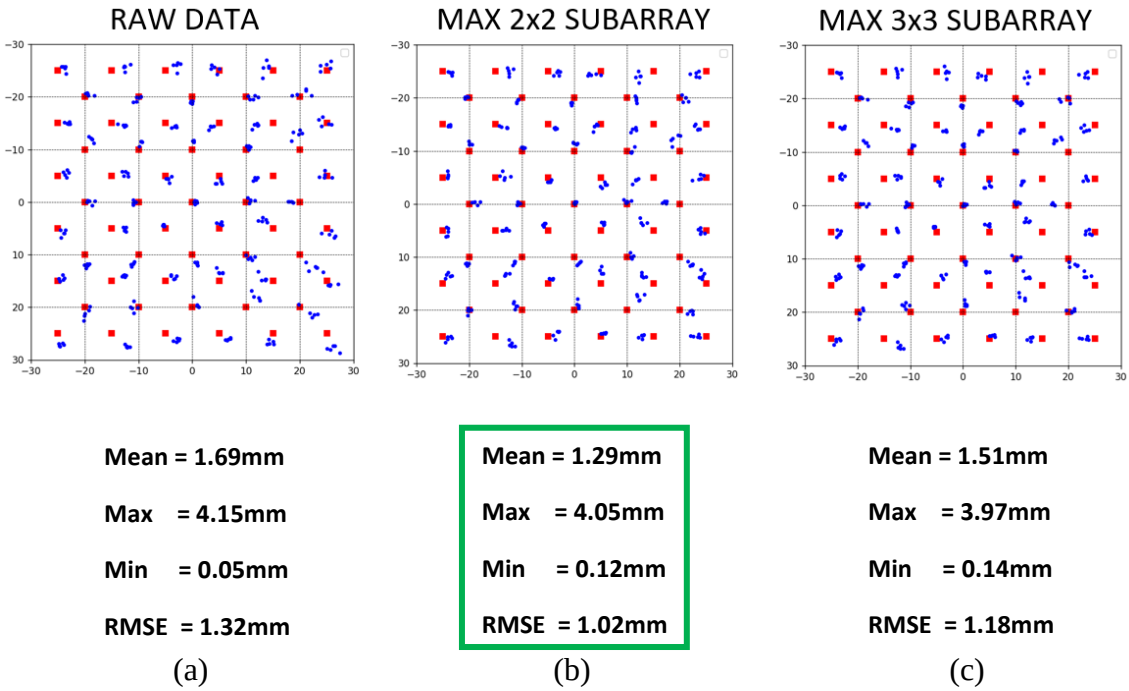

(a) (b) (c)

Figure 4.12. 5x5 COP results comparison for 100 g (a) raw data, (b) max 2x2 subarray and (c) max 3x3 subarray

In this section, the same analyzes are made for 100 g. The values obtained by using the 3x3 subarray (Figure 4.12c) were higher than the error values obtained by using raw data (Figure 4.12a). Again, the lowest error values are obtained with 2x2 subarray values (Figure 4.12b). An improvement of 0.4 mm is achieved in the mean error and 0.3 mm in the RMSE value of the system. The percentage reduction of errors is presented in Table 4.2.

Table 4.2. Error change with Kadane's algorithm for 100 g (5x5)

100 g	Raw Data	2x2 Subarray	% Change
Mean Error	1.69	1.29	-23.7%
Max Error	4.15	4.05	-2.4%
Min Error	0.05	0.12	140.0%
RMSE	1.32	1.02	-22.7%

4.3.1.3. 150 g

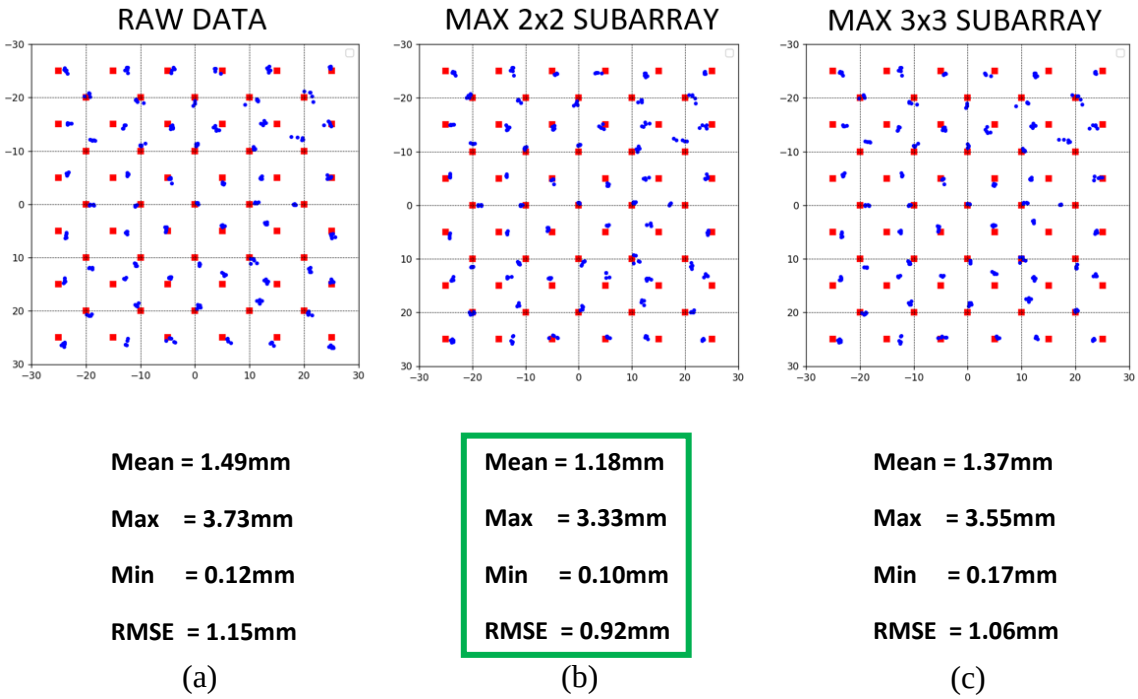

Figure 4.13. 5x5 COP results comparison for 150 g (a) raw data, (b) max 2x2 subarray and (c) max 3x3 subarray

In this section, the same analyzes are made for 150 g. Again, the values obtained by using the 3x3 subarray (Figure 4.13c) were higher than the error values obtained by using raw data (Figure 4.13a). Again, the lowest error values are obtained with 2x2 subarray values (Figure 4.13b). An improvement of 0.31 mm is achieved in the mean error and 0.23 mm in the RMSE value of the system. The percentage reduction of errors is presented in Table 4.3.

Table 4.3. Error change with Kadane's algorithm for 150 g (5x5)

150 g	Raw Data	2x2 Subarray	% Change
Mean Error	1.49	1.18	-20.8%
Max Error	3.73	3.33	-10.7%
Min Error	0.12	0.1	-16.7%
RMSE	1.15	0.92	-20.0%

4.3.2. 7x7 Results

4.3.2.1. 50 g

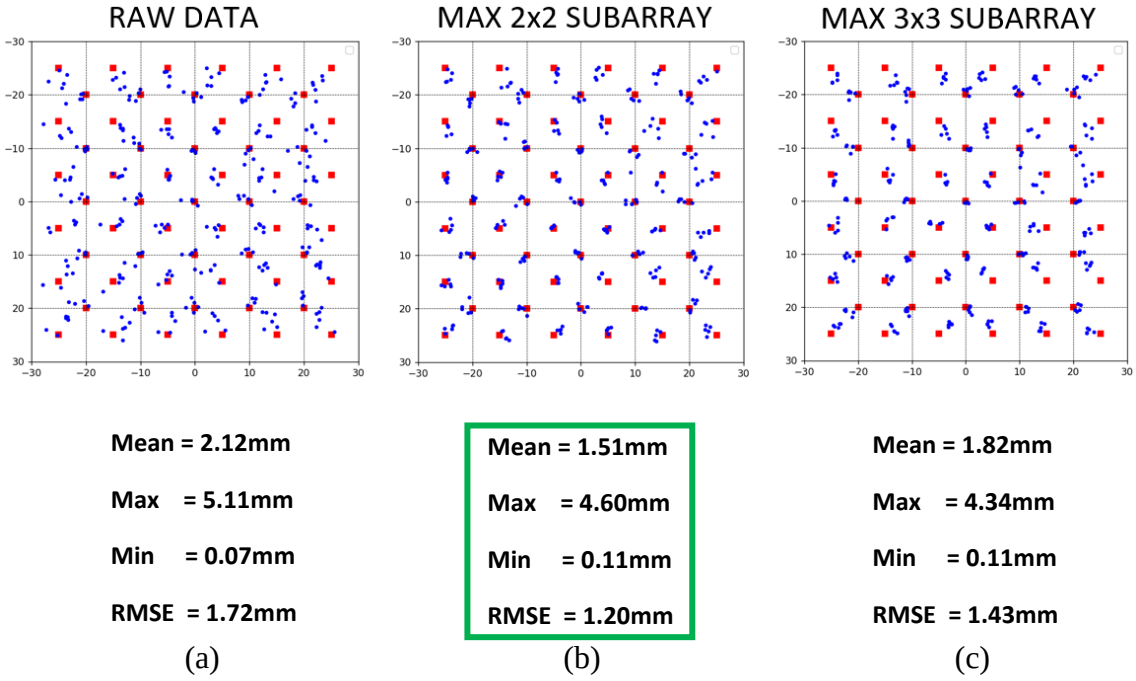

(a) (b) (c)

Figure 4.14. 7x7 COP results comparison for 50 g (a) raw data, (b) max 2x2 subarray and (c) max 3x3 subarray

In this section, the COP values obtained by taking all the values in 49 sensels (Figure 4.14a) of the load placed on the sensor, taking only 4 sensel values (Figure 4.14b) and using 9 sensel values (Figure 4.14c) are shared comparatively. The lowest error values are again obtained with 2x2 subarray values. An improvement of 0.61 mm is achieved in the mean error and 0.52 mm in the RMSE value of the system. The percentage reduction of errors is presented in Table 4.4.

Table 4.4. Error change with Kadane's algorithm for 50 g (7x7)

50 g	Raw Data	2x2 Subarray	% Change
Mean Error	2.12	1.51	-28.8%
Max Error	5.11	4.6	-10.0%
Min Error	0.07	0.11	57.1%
RMSE	1.72	1.2	-30.2%

4.3.2.2. 100 g

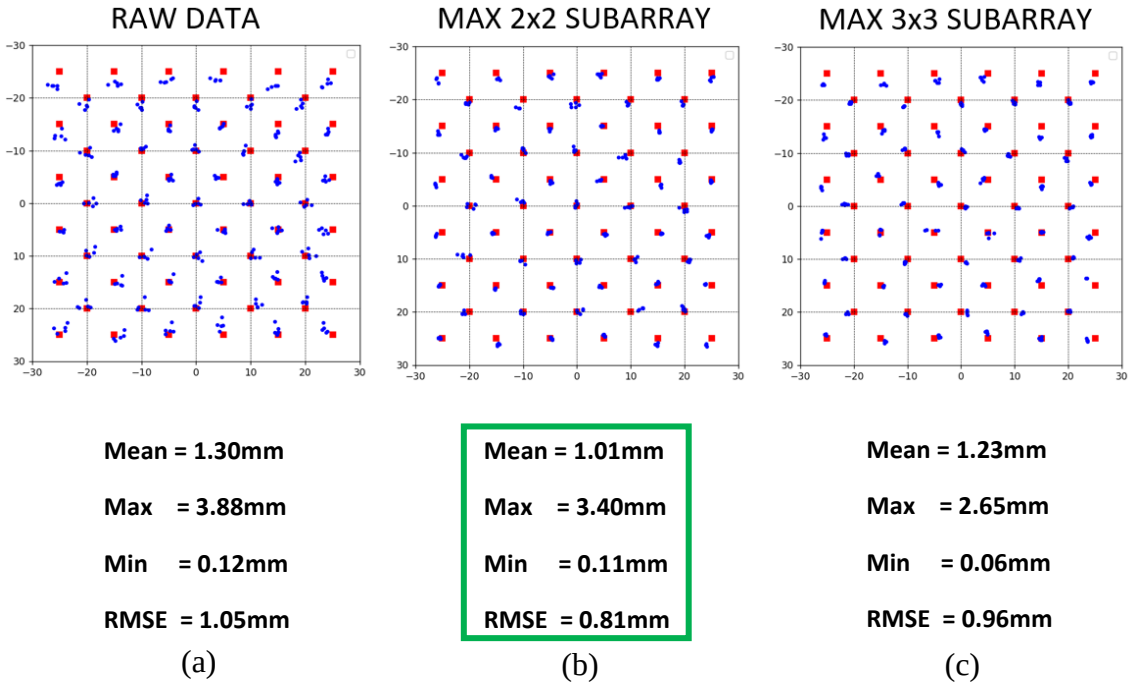

Figure 4.15. 7x7 COP results comparison for 100 g (a) raw data, (b) max 2x2 subarray and (c) max 3x3 subarray

In this section, the same analyzes are made for 100 g. Again, the lowest error values are obtained with 2x2 subarray values (Figure 4.15b). An improvement of 0.29 mm is achieved in the mean error and 0.24 mm in the RMSE value of the system. The percentage reduction of errors is presented in Table 4.5.

Table 4.5. Error change with Kadane's algorithm for 100 g (7x7)

100 g	Raw Data	2x2 Subarray	% Change
Mean Error	1.3	1.01	-22.3%
Max Error	3.88	3.4	-12.4%
Min Error	0.12	0.11	-8.3%
RMSE	1.05	0.81	-22.9%

4.3.2.3. 150 g

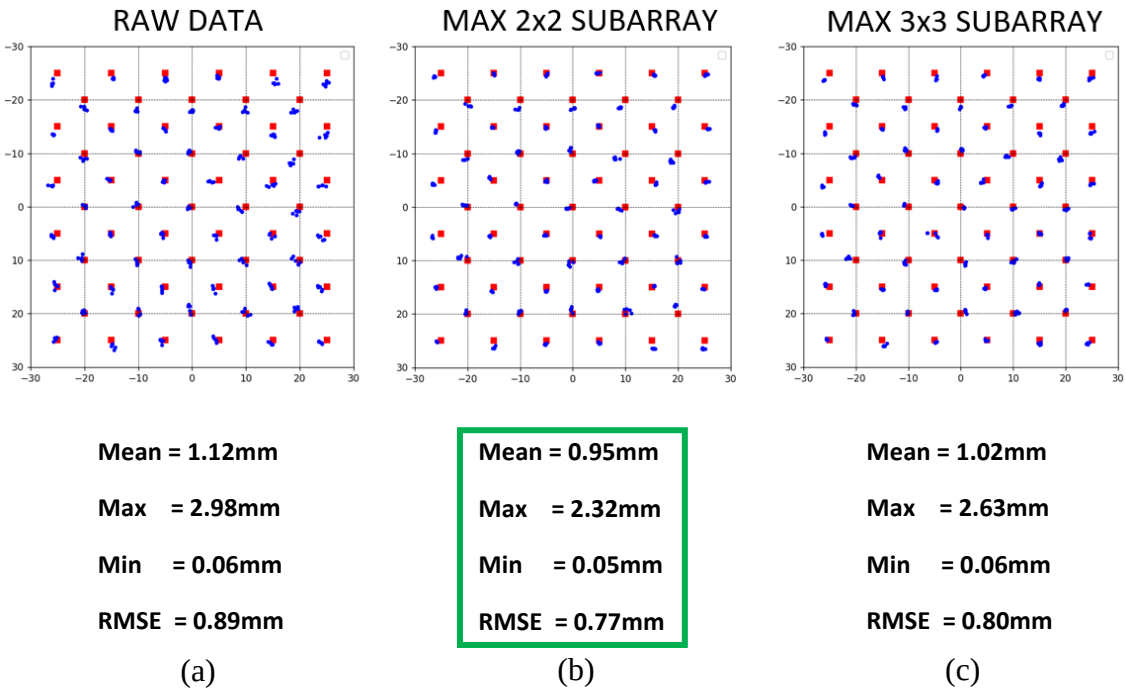

Figure 4.16. 7x7 COP results comparison for 150 g (a) raw data, (b) max 2x2 subarray (c) max 3x3 subarray

Lastly, the same analyzes are made for 150 g. Again, the lowest error values are obtained with 2x2 subarray values (Figure 4.16b). An improvement of 0.17 mm is achieved in the mean error and 0.12 mm in the RMSE value of the system. The percentage reduction of errors is presented in Table 4.6.

Table 4.6. Error change with Kadane's algorithm for 150 g (7x7)

150 g	Raw Data	2x2 Subarray	% Change
Mean Error	1.12	0.95	-15.2%
Max Error	2.98	2.32	-22.1%
Min Error	0.06	0.05	-16.7%
RMSE	0.89	0.77	-13.5%

Looking at the results obtained, the 2x2 subarray method in both 5x5 and 7x7 sensor arrays provided a significant improvement in position errors. The minimum error values have not changed much since they are already low values, but the maximum error, average error and RMSE values of the system have decreased by 10-35% percentage.

4.3.3. Circle Fit Results

The distance of the theoretical circle center, which passes through these 305 measurements, to the origin is examined. Although the different measurements at each point are different from each other, the imaginary circle center formed by 305 point clouds is a maximum of 1.17 mm away from the point of origin. This leads to the conclusion that the 2D sensor array measured homogeneously over an area of 60 mm x 60 mm. If this displacement was too much in one direction specifically, it could result in the sensor measuring more incorrectly at some certain points. In Table 4.7, the distances of the center point to the origin are shared in millimeters as euclidean distance. It is observed that Kadane's algorithm results are again lower than the raw data results. (Figure 4.17)

Table 4.7. Circle fit results of the experiments

Matrix	Weight	Data	Distance to the origin (mm)
5x5	50 g	2x2 subarray	0.05
5x5	150 g	2x2 subarray	0.1
5x5	100 g	2x2 subarray	0.26
5x5	150 g	Raw data	0.6
7x7	150 g	2x2 subarray	0.66
7x7	50 g	2x2 subarray	0.73
7x7	100 g	2x2 subarray	0.79
7x7	100 g	Raw data	0.84
5x5	100 g	Raw data	0.94
7x7	150 g	Raw data	1.05
7x7	50 g	Raw data	1.17
5x5	50 g	Raw data	1.17

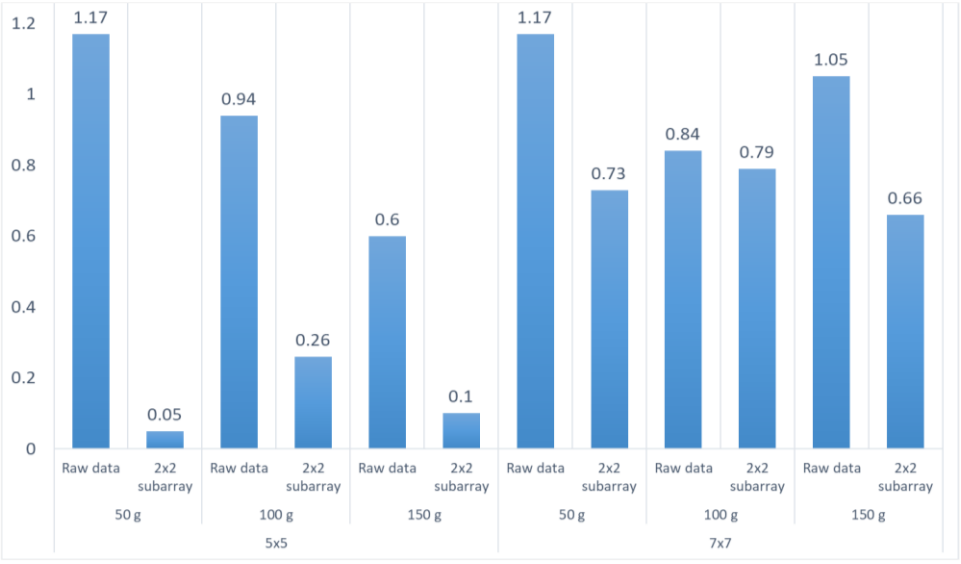

Figure 4.17. Visual comparison of circle fit results

4.4. 5x5 & 7x7 Sensor Arrays Comparison

Comparing the performance of the 5x5 and 7x7 sensor arrays at the same test points can reveal the effect of pixels per inch (PPI) variable. COP analyses of 61 test points in the same measuring area of 60 mm x 60 mm in both configurations are performed using 25 sensels in the 5x5 sensor array and 49 sensels in the 7x7 sensor array. Table 4.8 presents the performance results obtained using raw data of two different sensor configurations. A graphical representation of these values can be seen in Figure 4.18. All values are given in millimeters.

Table 4.8. Comparison of 5x5 & 7x7 sensor arrays (raw data)

RAW DATA	50 g		100 g		150 g	
	5x5	7x7	5x5	7x7	5x5	7x7
Max	7.63	5.11	4.15	3.88	3.73	2.98
Min	0.12	0.07	0.05	0.12	0.12	0.06
Mean	2.31	2.12	1.69	1.3	1.49	1.12
RMSE	1.84	1.72	1.32	1.05	1.15	0.89

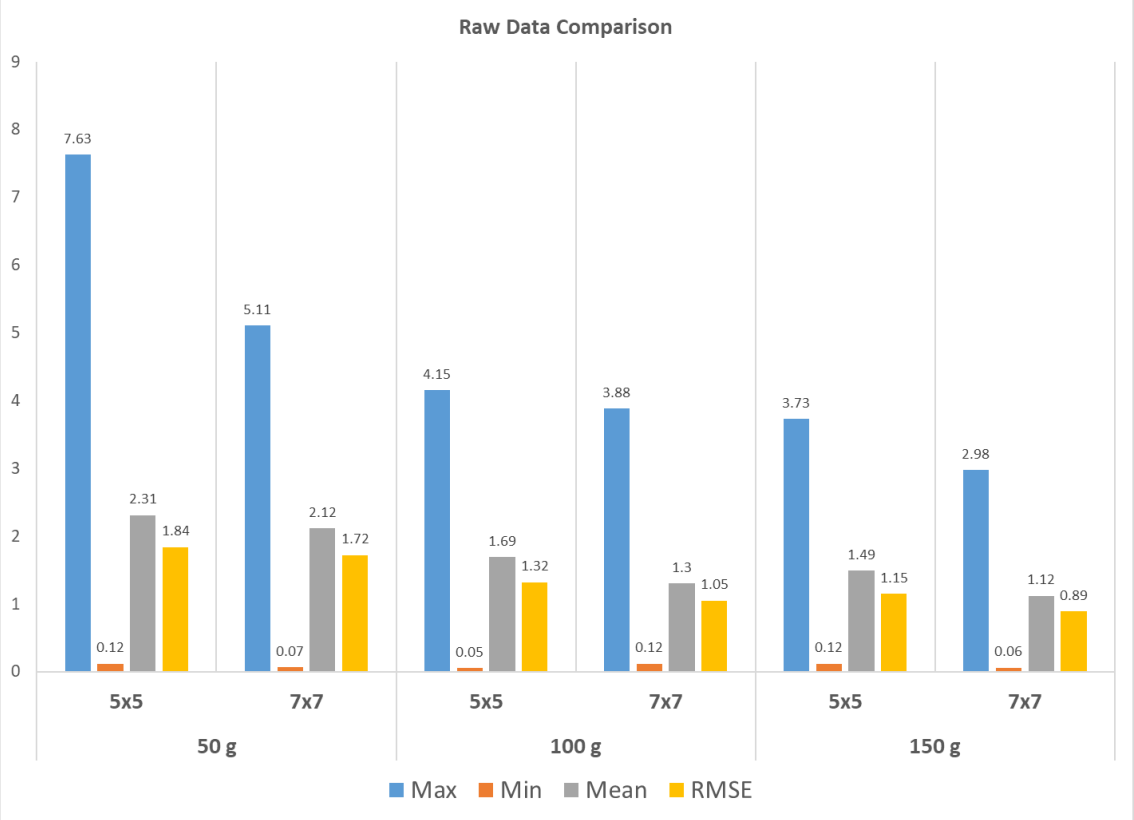

Figure 4.18. Visual comparison of 5x5 & 7x7 sensor arrays (raw data)

The comparison results with the 2x2 subarray data that give the lowest error results in the COP calculations can be seen in Table 4.9. Also, a graphical representation of these values can be seen in Figure 4.19.

Table 4.9. Comparison of 5x5 & 7x7 sensor arrays (2x2 subarray)

2x2 Subarray	50 g		100 g		150 g	
	5x5	7x7	5x5	7x7	5x5	7x7
Max	5.42	4.6	4.05	3.4	3.33	2.32
Min	0.08	0.11	0.12	0.11	0.1	0.05
Mean	1.89	1.51	1.29	1.01	1.18	0.95
RMSE	1.52	1.2	1.02	0.81	0.92	0.77

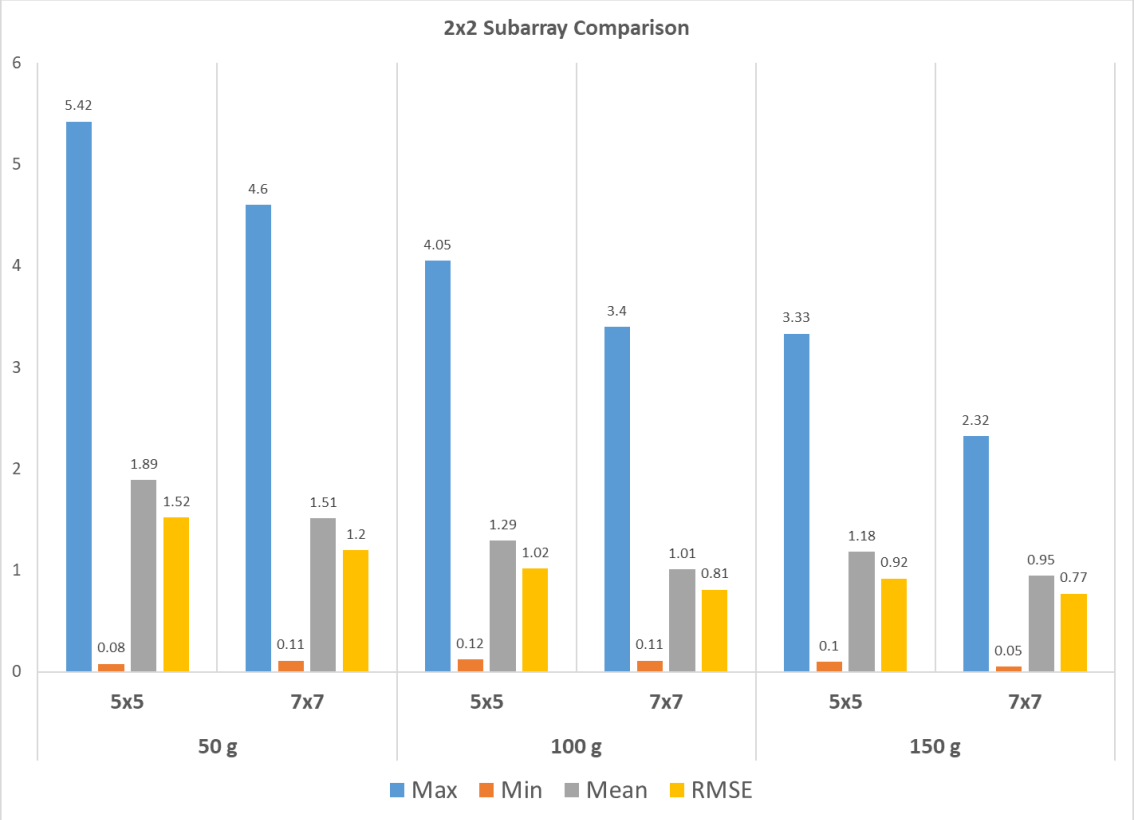

Figure 4.19. Visual comparison of 5x5 & 7x7 sensor arrays (2x2 subarray)

When looking at both the raw data and the 2x2 subarray results, the error values at the same test points were lower in the 7x7 sensor array. In other words, according to the results, the sensor assembly with a higher PPI value (Section 3.5.1) gives more accurate results in terms of position measurement. In addition, for all different weights in both 5x5 and 7x7 sensor arrays, Kadane's Algorithm provided more successful results in all error metrics compared in the system. (Figure 4.20-22)

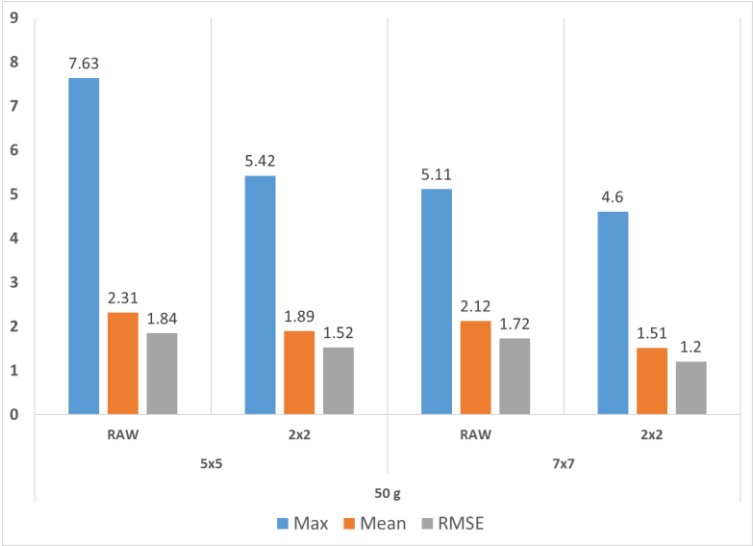

Figure 4.20. Raw data vs Kadane's algorithm results (50 g)

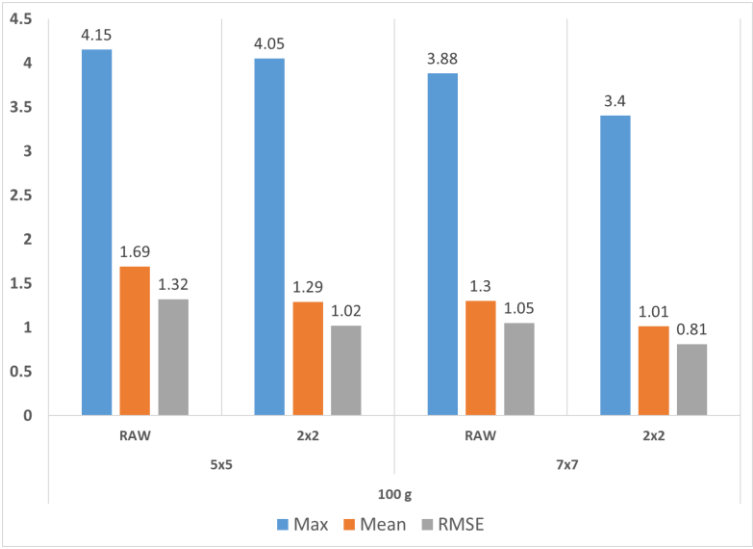

Figure 4.21. Raw data vs Kadane's algorithm results (100 g)

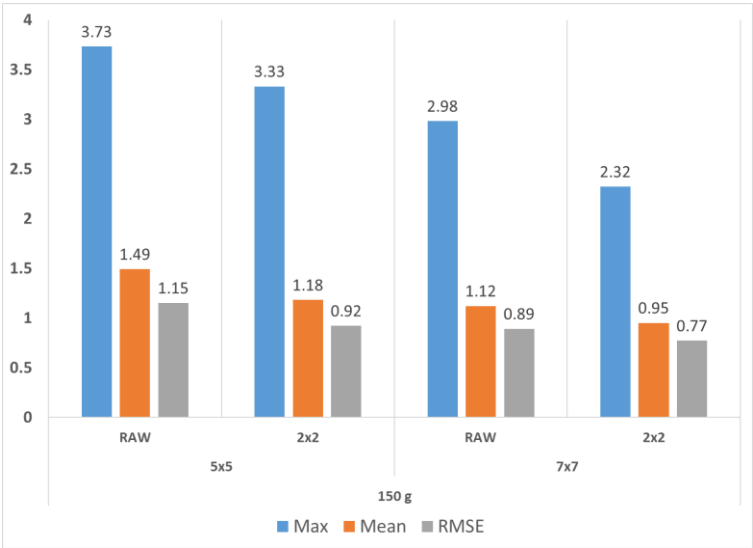

Figure 4.22. Raw data vs Kadane's algorithm results (150 g)

4.5. Regression Analysis

In this section, the regression models using 150 g results in the 7x7 sensor array are discussed for further analyses. In real life applications, multivariate linear regression method is used for calibration, especially in resistive touch panels [93]. Touch panels usually have a calibration equation of the system by specifying 9, 16 and 25 points. The error values of these points, calculated by the sensor, are tried to be converged to the target value, that is, their actual coordinates. Therefore, in this thesis, first 36 test points are selected as training points (aka calibration points), and remaining 25 test points are selected as test points arbitrarily as depicted in Figure 4.23.

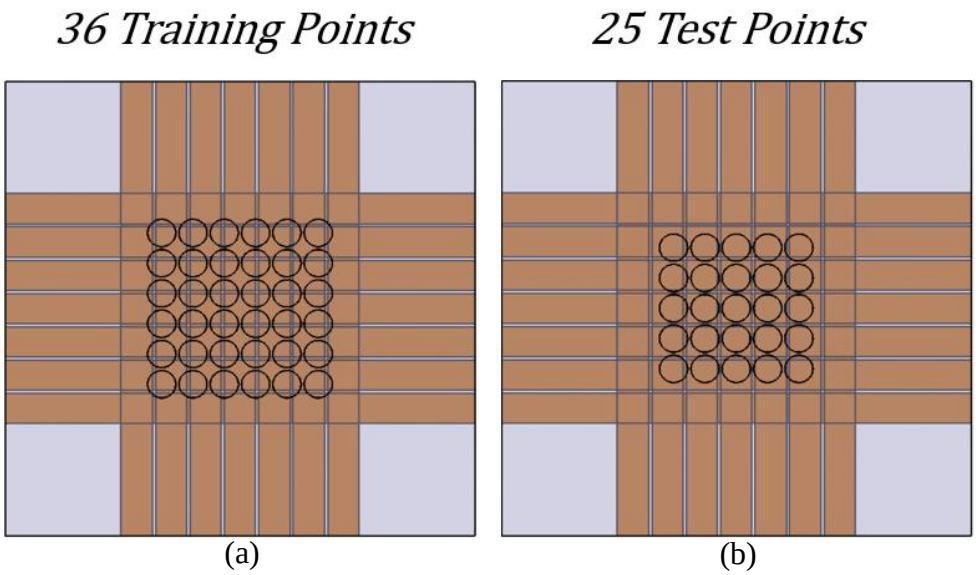

(a) (b)

Figure 4.23. 7x7 regression analysis for 150 g (a) training points, (b) test points

Normally, the RMSE value of 150 g load according to raw data is 0.89 mm. This value is calculated based on a total of 305 measurement results by taking 5 measurements from each of the 61 points. Now we can divide this data set into 36 training points (180 measurements) and 25 test points (125 measurements). The RMSE values of this separated data, training and test data, can be seen separately in Table 4.10.

Table 4.10. 7x7 sensor array 150 g raw data splitted RMSE values

7x7 150 g Raw Data	Whole System (61 points)	Training Data (36 points)	Test Data (25 points)
RMSE	0.89	0.85	0.96

Now using 180 data points, regression equation of the system can be calculated. In table 4.11, first 5 data points of 180 training points is shown. In the regression model, by using 2 input values “X_Predict” and “Y_Predict”, it is possible to have 2 regression equation for 2 output features. “X_Predict” and “Y_Predict” values are values calculated by sensor array. With these regression equations, the values calculated by the sensor will be tried to be converged to the actual coordinate values.

Table 4.11. First 5 sample points of the training data set

	OUTPUT 1	**OUTPUT 2**	**INPUTS**	
POINT	**X_REAL**	**Y_REAL**	**X_PREDICT**	**Y_PREDICT**
1	-25	-25	-25.64172336	-23.86243386
1	-25	-25	-25.94086957	-23.23391304
1	-25	-25	-25.95598007	-23.12375415
1	-25	-25	-25.9875	-22.64166667
1	-25	-25	-25.95580589	-23.01993068

When the sensor results of 180 training data are calculated as input (X_Predict & Y_Predict) and the actual coordinates as output (X_Real & Y_Real), a total of 2 equations are obtained. The first of these equations is for the "x" coordinate, and the second is for the "y" coordinate. In Table 4.12 and 4.13, regression coefficients can be seen.

Table 4.12. Coefficients for the Output 1 (X_Real)

	Coefficients	*Standard Error*	*t Stat*	*P-value*
Intercept	0.514001932	0.039589845	12.98317606	1.64702E-27
X_PREDICT	1.002316857	0.002321788	431.7003592	1.8172E-269
Y_PREDICT	0.007855682	0.002369644	3.315131562	0.001111189

Table 4.13. Coefficients for the Output 2 (Y_Real)

	Coefficients	*Standard Error*	*t Stat*	*P-value*
Intercept	-0.678384683	0.040493695	-16.75284704	2.34296E-38
X_PREDICT	-0.006995245	0.002374796	-2.945619939	0.003656636
Y_PREDICT	1.022946521	0.002423744	422.0522101	9.8901E-268

Now, we have 2 equations obtained from 180 training data points.

1) $X_{New_{Output}} = 0.514001932 + \mathrm{X_{Predict}} * \ 1.002316857 + \mathrm{Y_{Predict}} * 0.007855682$

2) $Y_{New_{Output}} = -0.678384683 + \mathrm{X_{Predict}} * \ -0.006995245 + \mathrm{Y_{Predict}} * 1.022946521$

Now, it is possible use these equations for the 125 test data points. And by putting the "predicted" values of these 125 test points calculated by the sensor into these equations, the new output coordinates can be calculated.

Table 4.14. First 5 sample points of the test data set & new values

X_PREDICT	Y_PREDICT	X_New_Output 1	Y_New_Output 2
-19.98744395	-18.79372197	-19.66738757	-19.76354011
-20.63061224	-18.7	-20.31130975	-19.66316843
-19.62476008	-18.16794626	-19.29894752	-19.12594208
-20.02061856	-18.31958763	-19.69691439	-19.27829397
-19.95348837	-18.28003876	-19.62931799	-19.23830718

The new values of all the test data, which are estimated by means of regression equations, can be calculated. In Table 4.14, the new values of the first 5 points of the test dataset can be seen. The results of all test data and the RMSE values of the regression equations applied to all data can be seen in Table 4.15. According to the new predicted values obtained using the regression equations, the RMSE value of the 25 test points decreases from 0.96 to 0.69. When all the measurement values, i.e., 305 point regression equations, are subjected, the RMSE value of the system decreases from 0.89 to 0.6. When these results are looked at using the system equations derived from the randomly chosen measurement points, the sensor outputs of the other points on the system can be predicted and the error metrics on the system can be reduced.

Table 4.15. Regression results of 150 g raw data (7x7)

7x7 150 g Raw Data	Whole System (61 points)	Training Data (36 points)	Test Data (25 points)	Test Data with Regression	Whole System with Regression
RMSE	0.89	0.85	0.96	0.69	0.60

After examining the results obtained in the first regression analysis, the training and test points in the regression analysis are then selected in such a way that they are opposite. The 25 points that were determined as test points in the previous experiment are selected as training points this time, and 36 points that were determined as training points are selected as test points in this new regression analysis.

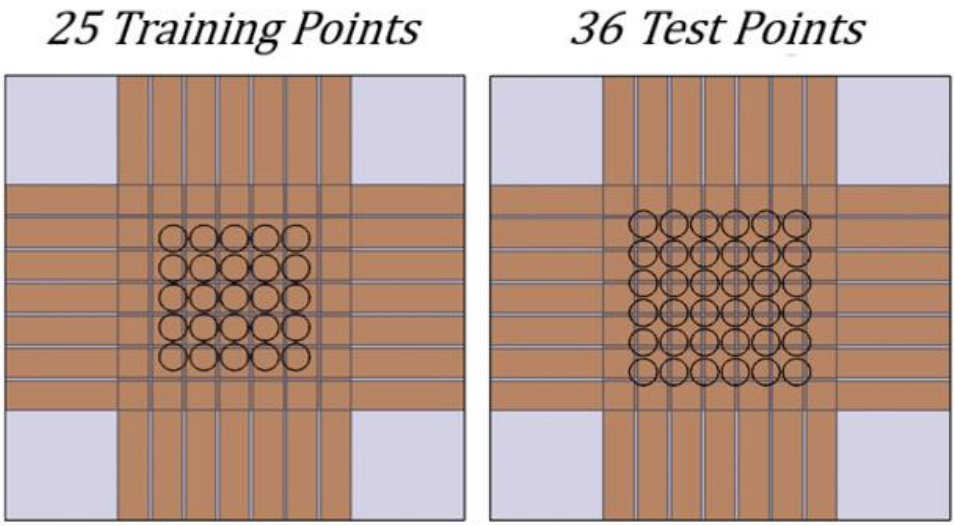

(a) (b)

Figure 4.24. Second regression analysis (a) 25 training points, (b) 36 test points

Table 4.16. Second regression results of 150 g raw data (7x7)

7x7 150 g Raw Data	Whole System (61 points)	Training Data (25 points)	Test Data (36 points)	Test Data with Regression	Whole System with Regression
RMSE	0.89	0.96	0.85	0.72	0.66

The results of all test data and the RMSE values of the regression equations applied to all data can be seen in Table 4.16. According to the new predicted values obtained using the regression equations, the RMSE value of the 36 test points decreases from 0.85 to 0.72. When all the measurement values, i.e., 305 point regression equations, are subjected, the RMSE value of the system decreases from 0.89 to 0.66. Again, when these data are examined using the system equations derived from the randomly selected measurement points, the sensor outputs of other points on the system may be anticipated and the error metrics on the system can be lowered.

In the next stage, regression analysis is performed with COP values (7x7 sensor array and 150 g) calculated using the 2x2 subarray that gave the lowest RMSE value in the system. The results can be seen in Table 4.17 and Table 4.18.

Table 4.17. Regression results of 2x2 subarray with 36 training points

7x7 150 g 2x2 Subarray	Whole System (61 points)	Training Data (36 points)	Test Data (25 points)	Whole System with Regression
RMSE	0.77	0.64	0.93	0.76

Table 4.18. Regression results of 2x2 subarray with 25 training points

7x7 150 g 2x2 Subarray	Whole System (61 points)	Training Data (25 points)	Test Data (36 points)	Whole System with Regression
RMSE	0.77	0.93	0.64	0.75

In the regression analyzes performed using 2x2 subarray COP data, it is observed that the RMSE value in the system decreased slightly. Looking at these results, the issue of determining the points used in obtaining the regression equations is critical. Regression equations differ according to the location and number of points selected, and it is observed that these variables can have a significant impact on the analysis of the whole system.

Unlike regression analysis on touch screens, a third independent variable can be defined in the analysis. In the final regression analysis performed with the data (150 g raw data) collected in the 7x7 sensor assembly, 915 (305 x 3) measurement points obtained by using three different weights were used. In Table 4.19, the first 15 of the 915 samples can be seen. Accordingly, in predicting errors in the system, the load variable may also be taken into account. Similarly, it was observed that the RMSE value of the system decreased from 0.89 to 0.66 by introducing the new input.

Table 4.19. Regression analysis with 3 input variables

First 15 samples		Output 1	Output 2	Input 1	Input 2	Input 3
SAMPLE	**POINT**	**X_REAL**	**Y_REAL**	**X_PREDICT**	**Y_PREDICT**	**LOAD**
1	1	-25	-25	-25.64172336	-23.86243386	150
2	1	-25	-25	-25.94086957	-23.23391304	150
3	1	-25	-25	-25.95598007	-23.12375415	150
4	1	-25	-25	-25.9875	-22.64166667	150
5	1	-25	-25	-25.95580589	-23.01993068	150
6	1	-25	-25	-27.02792141	-22.4663909	100
7	1	-25	-25	-26.18360656	-22.16830601	100
8	1	-25	-25	-26.19168591	-22.22863741	100
9	1	-25	-25	-25.31111111	-21.67777778	100
10	1	-25	-25	-25.42006615	-22.27894157	100
11	1	-25	-25	-26.5174538	-22.42915811	50
12	1	-25	-25	-23.64212679	-22.02249489	50
13	1	-25	-25	-24.85185185	-24.28148148	50
14	1	-25	-25	-24.35852373	-21.28471002	50
15	1	-25	-25	-23.41284404	-23.39266055	50

4.6. Discussion

In section 4.1, COP calculations for three distinct weights were performed at 61 test points in the 5x5 sensor array, with five measurements per test point, and the results are discussed. In section 4.2, COP calculations were performed within the 7x7 sensor array. In addition to these measurements, the "Circle Fitting" method is proposed and examined to find the center of the circle theoretically formed by 305 measurements. The aim was to examine whether the center of all measurement points had a deviation in any specific direction. According to the first results, it is observed that the system's error metrics decreased as the load on the 5x5 and 7x7 arrays increased. Additionally, it has been observed that the RMSE of the entire system has decreased. In section 4.3, in contrast to the literature's complex error reduction solutions, the results of the improvement method proposed for the first time in this thesis are presented, which is the Kadane's Algorithm. Using this method, COP calculations based on maximum 2x2 and 3x3 subarray values in whole arrays were calculated and compared to COP measurements based on raw data. According to these results, the measurements utilizing 2x2 subarray values provided the most efficient reduction in error metrics. In section 4.4, the 5x5 and 7x7 sensor arrays are compared to each other. Other than their respective sensel numbers, the remaining parameters of these two distinct experimental setups are identical. The objective was to observe how the number of sensels or sensor resolution in the system (PPI) affected the error measurements at the same test points. According to the findings, the errors in all weights were smaller in the 7x7 assembly than in the 5x5 experimental setup for both raw data and 2x2 subarray data. In section 4.5, the results of experimental regression for 7x7 sensor arrays are discussed. In the 7x7 sensor array using raw data of 150 g, 36 training points and 25 test points were determined. Later, the regression analysis was performed by selecting the points in the opposite way. Based on these results, it is clear that regression can also be used to reduce errors. Finally, the regression analysis was performed with 3 independent inputs by including the weight variable. According to the results, it was again observed that the RMSE value in the system could be lowered again.

CHAPTER 5

CONCLUSION

The main aim of this thesis was to conduct studies and obtain determinations about error analysis and characterization in piezoresistive array touch sensors. However, as I get into it, I have discovered and experienced that there are a lot of variables related to these sensor types. It has been a challenging and enjoyable journey to select sensor materials, determine the circuit diagram of the sensor, choose a suitable weight of the load to be used on the sensor, and discover what tests can be performed on the sensors when the test setups are constructed. As the studies and conducted experiments are examined, the aims of this study are revised and become much clearer. As I learned more about the subject, I came up with the following goals for this thesis: design and build a tactile sensor that can detect forces similar to those applied by human fingers and fingertip sizes; measure and test the performance characteristics of the sensor on a flat surface for static position accuracy; compare the performance of different meshed sensors; look for ways to improve the process and reduce error metrics; and finally, discover ways to make the sensor more accurate.

According to the experience obtained in the preliminary experiments, first of all, the issue of determining the force to be applied and the contact area of the force touching the sensor has gained priority. Accordingly, when the literature was reviewed on these subjects, the minimum forces in the different types of gestures that human fingers apply to touch screens and the optimal contact area were selected in the first place for the testing of the sensors to be designed and manufactured in this experiment. This load was selected as 50 g with a 9 mm diameter and designed in the CAD software Catia v5®. It was also manufactured in the machine shop within the university. The first sensor setup is also designed by means of the Catia v5® software so that the test load touches at least one sensel in the sensor. Then, the sensor was hand-built from scratch with the simplest possible and easy-to-supply materials, which are much cheaper than the comparable sensors in commercially available products on the market. After first trials, it was decided that testing two different sensor configurations (5x5 and 7x7) in terms of static position sensitivity with three different weights to increase diversity would be a great choice for

this thesis's studies. 61 test points within the 60 mm x 60 mm area are set for the comparison of the measurement results of these same points in two different sensor configurations. The Arduino MCU's own IDE provided the data stream from the sensors used in the tests. The Python 3.10 software was used to record and analyze this data.

In the main experiments, it was observed that as the test load increased, the error metrics in the system decreased. In addition, it was observed that the 7x7 sensor array gave more successful results than the 5x5 sensor array at the same test points. Kadane's Algorithm, which is normally used in many other applications, was introduced and implemented in experiments aimed to reduce the error values. As a result, success was achieved, and it can be stated that there is no precedent for this application in the literature. This achievement can be considered one of the most important contributions of this thesis to the literature. Furthermore, with another proposed method, "Circle Fitting", the centers of the theoretical circle formed by 305 (61x5) measurements were found, and it was examined whether the sensor measurements were considered as homogeneous. In other words, in each case, the levels of decentralization did not vary much. Finally, the equations of the system were found by means of the selected points determined by Least Squares Regression and the predictability of the points in terms of position precision were studied. When these results are examined through the system equations obtained from the randomly selected measurement points, it is seen that both the sensor outputs of the other points on the system can be predicted and the error metrics on the system can be reduced.

To conclude, in this thesis, experiments were conducted on two different sensor arrays on flat surfaces, and the goals were achieved. However, as material and manufacturing technology advance, sensors with extremely complex circuits are being manufactured at high quality and at a rapid pace. Hence, a lot of progress is also being made regarding "crosstalk," one of the biggest issues with such sensors. In order to solve the crosstalk issue, a maximum subarray solution has been proposed in this thesis as an alternative to the complex solutions in the literature. In the future, similar analyses can be performed on curved surfaces. Moreover, conductive strips of different thicknesses can be used, and sensel sizes can be differentiated. In addition, loads can be placed on multiple test points at the same time and COP analyses can be performed for multi-touch applications. In addition to these, regression analyses can be performed using different points and the necessary optimization studies can be done to make the system work with minimum errors.

REFERENCES

[1] Webster, John G. *The measurement, instrumentation and sensors handbook*. Vol. 14. CRC press, 1998.

[2] Lee, Da-Huei, Cheng-Hsin, Chuang, Muhammad Omar, Shaikh, Yong-Syuan, Dai, Shao-Yu, Wang, Zhi-Hong, Wen, Chung-Kun, Yen, Chien-Feng, Liao, and Cheng-Tang, Pan. "Flexible Piezoresistive Tactile Sensor Based on Polymeric Nanocomposites with Grid-Type Microstructure". *Micromachines* 12, no.4 (2021): 452.

[3] Nicholls, Howard R, and Mark H, Lee. "A survey of robot tactile sensing technology". *The International Journal of Robotics Research* 8, no.3 (1989): 3–30.

[4] Najarian, Siamak, Javad Dargahi, Ali Abouei Mehrizi. *Artificial Tactile Sensing in Biomedical Engineering*. McGraw-Hill Biophotonics. New York, NY: McGraw-Hill Professional, 2009.

[5] Lee, Mark H, and Howard R, Nicholls. "Review Article Tactile sensing for mechatronics—a state of the art survey". *Mechatronics* 9, no.1 (1999): 1–31.

[6] Siciliano, Bruno, Oussama, Khatib, and Torsten, Kroger. *Springer handbook of robotics*. Vol. 200. Springer, 2008.

[7] Fraden, Jacob. "Handbook of modern sensors: physics, designs, and applications." (2007).

[8] Martinez, Uriel. "Autonomous active exploration for tactile sensing in robotics." PhD diss., University of Sheffield, 2014.

[9] Harmon, Leon D. "Automated tactile sensing". *The International Journal of Robotics Research* 1, no.2 (1982): 3–32.

[10] Schmidt, Peer A, Eric, Mael, and Rolf P, Würtz. "A sensor for dynamic tactile information with applications in human–robot interaction and object exploration". *Robotics and Autonomous Systems* 54, no.12 (2006): 1005–1014.

[11] Muhammad, HB, CM, Oddo, Lucia, Beccai, Carmine, Recchiuto, CJ, Anthony, MJ, Adams, MC, Carrozza, DWL, Hukins, and MCL, Ward. "Development of a bioinspired MEMS based capacitive tactile sensor for a robotic finger". *Sensors and Actuators A: Physical* 165, no.2 (2011): 221–229.

[12] Schmitz, Alexander, Perla, Maiolino, Marco, Maggiali, Lorenzo, Natale, Giorgio, Cannata, and Giorgio, Metta. "Methods and technologies for the implementation of large-scale robot tactile sensors". *IEEE Transactions on Robotics* 27, no.3 (2011): 389–400.

[13] Lee, Yong S, and Kensall D, Wise. "A batch-fabricated silicon capacitive pressure transducer with low temperature sensitivity". *IEEE transactions on electron devices* 29, no.1 (1982): 42–48.

[14] Webster, John G. *Tactile sensors for robotics and medicine*. John Wiley & Sons, Inc., 1988.

[15] Snyder, Wesley E, and Joseph St, Clair. "Conductive elastomers as sensor for industrial parts handling equipment". *IEEE Transactions on Instrumentation and Measurement* 27, no.1 (1978): 94–99.

[16] Briot, Maurice, and others. "The utilization of an artificial skin sensor for the identification of solid objects". In *9th Int. Symp. on Industrial Robots* (pp. 13–15), 1979.

[17] Russell, R. "Compliant-skin tactile sensor". In *Proceedings. 1987 IEEE International Conference on Robotics and Automation* (pp. 1645–1648), 1987.

[18] Beebe, David J, Arthur S, Hsieh, Denice D, Denton, and Robert G, Radwin. "A silicon force sensor for robotics and medicine". *Sensors and Actuators A: Physical* 50, no.1-2 (1995): 55–65.

[19] Kerpa, Oliver, Karsten, Weiss, and Heinz, Worn. "Development of a flexible tactile sensor system for a humanoid robot". In *Proceedings 2003 IEEE/RSJ International Conference on Intelligent Robots and Systems (IROS 2003)(Cat. No. 03CH37453)* (pp. 1–6), 2003.

[20] Weiss, Karsten, and Heinz, Woern. "Tactile sensor system for an anthropomorphic robotic hand". In *IEEE International conference on manipulation and grasping IMG*, 2004.

[21] Yousef, Hanna, Mehdi, Boukallel, and Kaspar, Althoefer. "Tactile sensing for dexterous in-hand manipulation in robotics—A review". *Sensors and Actuators A: physical* 167, no.2 (2011): 171–187.

[22] Begej, Stefan. "Planar and finger-shaped optical tactile sensors for robotic applications". *IEEE Journal on Robotics and Automation* 4, no.5 (1988): 472–484.

[23] Yamada, Yoji, Tetsuya, Morizono, Yoji, Umetani, and Hitoshi, Takahashi. "Highly soft viscoelastic robot skin with a contact object-location-sensing capability". *IEEE Transactions on Industrial electronics* 52, no.4 (2005): 960–968.

[24] Heo, Jin-Seok, Jong-Ha, Chung, and Jung-Ju, Lee. "Tactile sensor arrays using fiber Bragg grating sensors". *Sensors and Actuators A: Physical* 126, no.2 (2006): 312–327.

[25] Hsiao, Kaijen, Paul, Nangeroni, Manfred, Huber, Ashutosh, Saxena, and Andrew Y, Ng. "Reactive grasping using optical proximity sensors". In *2009 IEEE International Conference on Robotics and Automation* (pp. 2098–2105), 2009.

[26] Kinoshita, G, T, Hajika, and K, Hattori. "Multifunctional tactile sensors with multi-elements for fingers". In *Proceedings of the International Conference on Advanced Robotics* (pp. 195–202), 1983.

[27] Nowlin, William C. "Experimental results on Bayesian algorithms for interpreting compliant tactile sensing data". In *Proceedings. 1991 IEEE International Conference on Robotics and Automation* (pp. 378–383), 1991.

[28] Pearson, Martin J, Anthony G, Pipe, Chris, Melhuish, Ben, Mitchinson, and Tony J, Prescott. "Whiskerbot: A robotic active touch system modeled on the rat whisker sensory system". *Adaptive Behavior* 15, no.3 (2007): 223–240.

[29] Prescott, Tony J, Martin J, Pearson, Ben, Mitchinson, J Charles W, Sullivan, and Anthony G, Pipe. "Whisking with robots". *IEEE robotics & automation magazine* 16, no.3 (2009): 42–50.

[30] Pugh, A. "Robot Sensors: Tactile and Non-Vision, Vol. 2." (1986).

[31] Jayawant, BV. "Tactile sensing in robotics". *Journal of Physics E: Scientific Instruments* 22, no.9 (1989): 684.

[32] Dahiya, Ravinder S, Giorgio, Metta, Maurizio, Valle, and Giulio, Sandini. "Tactile sensing—from humans to humanoids". *IEEE transactions on robotics* 26, no.1 (2009): 1–20.

[33] Grahn, Allen R, and Lynn, Astle. "Robotic ultrasonic force sensor arrays". *Robot sensors* 2 (1986): 297–315.

[34] Yamada, Yoji, and Mark R, Cutkosky. "Tactile sensor with 3-axis force and vibration sensing functions and its application to detect rotational slip". In *Proceedings of the 1994 IEEE International Conference on Robotics and Automation* (pp. 3550–3557), 1994.

[35] Dario, Paolo, and Danilo, De Rossi. "Tactile sensors and the gripping challenge: Increasing the performance of sensors over a wide range of force is a first step toward robotry that can hold and manipulate objects as humans do". *IEEE spectrum* 22, no.8 (1985): 46–53.

[36] Tang, Keison, Arjun, Kumar, Muhammad, Nadeem, and Issam, Maaz. "CNN-based smart sleep posture recognition system". *IoT* 2, no.1 (2021): 119–139.

[37] Fatema, Anis, Surya, Poondla, Rishabh B, Mishra, and Aftab M, Hussain. "A low-cost pressure sensor matrix for activity monitoring in stroke patients using artificial intelligence". *IEEE Sensors Journal* 21, no.7 (2021): 9546–9552.

[38] Dzedzickis, Andrius, Ernestas, Sutinys, Vytautas, Bucinskas, Urte, Samukaite-Bubniene, Baltramiejus, Jakstys, Arunas, Ramanavicius, and Inga, Morkvenaite-Vilkonciene. "Polyethylene-carbon composite (Velostat®) based tactile sensor". *Polymers* 12, no.12 (2020): 2905.

[39] Khong Duc, Chien, Van-Phuc, Hoang, Duy, Tien Nguyen, and Toan, Thanh Dao. "A low-cost, flexible pressure capacitor sensor using polyurethane for wireless vehicle detection". *Polymers* 11, no.8 (2019): 1247.

[40] Ahmadizadeh, Chakaveh, and Carlo, Menon. "Investigation of regression methods for reduction of errors caused by bending of FSR-based pressure sensing systems used for prosthetic applications". *Sensors* 19, no.24 (2019): 5519.

[41] Spreeuwers, Luuk, and Haitao, Wang. "A high resolution pressure sensor for measurement of grip force". In *40th WIC Symposium on Information Theory in the Benelux 2019*, 2019.

[42] Pizarro, Francisco, Piero, Villavicencio, Daniel, Yunge, Mauricio, Rodriguez, Gabriel, Hermosilla, and Ariel, Leiva. "Easy-to-build textile pressure sensor". *Sensors* 18, no.4 (2018): 1190.

[43] Ferreira, AG, Andre P, Catarino, Joao L, Monteiro, and Ana M, Rocha. "Textile-based pressure sensors for step detection: a preliminary assessment". In *IOP Conference Series: Materials Science and Engineering* (pp. 012041), 2018.

[44] Ramalingame, Rajarajan, Zheng, Hu, Carina, Gerlach, Dhivakar, Rajendran, Tatiana, Zubkova, Reinhard, Baumann, and Olfa, Kanoun. "Flexible piezoresistive sensor matrix based on a carbon nanotube PDMS composite for dynamic pressure distribution measurement". *Journal of Sensors and Sensor Systems* 8, no.1 (2019): 1–7.

[45] Valle-Lopera, Diego Andres, Andrés Felipe, Castaño-Franco, Jonathan, Gallego-Londono, and Alher Mauricio, Hernández-Valdivieso. "Test and fabrication of piezoresistive sensors for contact pressure measurement". *Revista Facultad de Ingenieria Universidad de Antioquia*, no.82 (2017): 47–52.

[46] Ahmad, Jawad, Henrik, Andersson, and Johan, Siden. "Sitting posture recognition using screen printed large area pressure sensors". In *2017 Ieee Sensors* (pp. 1–3), 2017.

[47] Suprapto, SS, AW, Setiawan, H, Zakaria, W, Adiprawita, and B, Supartono. "Low-cost pressure sensor matrix using velostat". In *2017 5th International Conference on Instrumentation, Communications, Information Technology, and Biomedical Engineering (ICICI-BME)* (pp. 137–140), 2017.

[48] Zhou, Bo, Carlos Andres, Velez Altamirano, Heber, Cruz Zurian, Seyed Reza, Atefi, Erik, Billing, Fernando, Seoane Martinez, and Paul, Lukowicz. "Textile pressure mapping sensor for emotional touch detection in human-robot interaction". *Sensors* 17, no.11 (2017): 2585.

[49] Giovanelli, Davide, and Elisabetta, Farella. "Force sensing resistor and evaluation of technology for wearable body pressure sensing". *Journal of Sensors* 2016 (2016).

[50] Lin, Xiaoyou, and Boon-Chong, Seet. "A linear wide-range textile pressure sensor integrally embedded in regular fabric". *IEEE Sensors Journal* 15, no.10 (2015): 5384–5385.

[51] Barba, Ricardo, Angel P, Madrid, and Jesus G, Boticario. "Development of an inexpensive sensor network for recognition of sitting posture". *International Journal of Distributed Sensor Networks* 11, no.8 (2015): 969237.

[52] Lee, Byung Woo, and Hangsik, Shin. "Feasibility study of sitting posture monitoring based on piezoresistive conductive film-based flexible force sensor". *IEEE Sensors Journal* 16, no.1 (2015): 15–16.

[53] Vega-Barbas, Mario, Ivan, Pau, Javier, Ferreira, Evelyn, Lebis, and Fernando, Seoane. "Utilizing smart textiles-enabled sensorized toy and playful interactions for assessment of psychomotor development on children". *Journal of Sensors* 2015 (2015).

[54] Carrozzino, Marcello, Giovanni, Avveduto, Franco, Tecchia, Pavel, Gurevich, and Benjamin, Cohen. "Navigating immersive virtual environments through a foot controller". In *Proceedings of the 20th ACM symposium on virtual reality software and technology* (pp. 23–26), 2014.

[55] Low, Jin Huat, Khin Phone, May, and Chen Hua, Yeow. "Redistribution of plantar pressure with pneumatic insole". In *Proceedings of the international Convention on Rehabilitation Engineering & Assistive Technology* (pp. 1–4), 2014.

[56] Harris, Luke. "Design and fabrication of a piezoresistive fabric sensor for ergonomic analyses." PhD diss., University of Guelph, 2014.

[57] Janczak, Daniel, Marcin, Sloma, Grzegorz, Wroblewski, Anna, Mlozniak, and Malgorzata, Jakubowska. "Screen-printed resistive pressure sensors containing graphene nanoplatelets and carbon nanotubes". *Sensors* 14, no.9 (2014): 17304–17312.

[58] Salibindla, Sravan, Brice, Ripoche, Daniel TH, Lai, and Simon, Maas. "Characterization of a new flexible pressure sensor for body sensor networks". In *2013 IEEE eighth international conference on intelligent sensors, sensor networks and information processing* (pp. 27–31), 2013.

[59] Kalantari, Masoud, Javad, Dargahi, Jozsef, Kovecses, Mahmood Ghanbari, Mardasi, and Shahrzad, Nouri. "A new approach for modeling piezoresistive force sensors based on semiconductive polymer composites". *IEEE/ASME Transactions on Mechatronics* 17, no.3 (2011): 572–581.

[60] Donselaar, Rik, and Wei, Chen. "Design of a smart textile mat to study pressure distribution on multiple foam material configurations". In *Proceedings of the 4th International Symposium on Applied Sciences in Biomedical and Communication Technologies* (pp. 1–5).2011.

[61] Fairman, Evart, and Dwight, Santimore. "The Smart Vest." PhD diss., Worcester Polytechnic Institute, 2011.

[62] Jeong, Eunseok, Jaehong, Lee, and DaeEun, Kim. "Finger-gesture recognition glove using velostat (ICCAS 2011)". In *2011 11th International Conference on Control, Automation and Systems* (pp. 206–210), 2011.

[63] Del Prete, Z, L, Monteleone, and R, Steindler. "A novel pressure array sensor based on contact resistance variation: Metrological properties". *Review of Scientific Instruments* 72, no.2 (2001): 1548–1553.

[64] Perner-Wilson, Hannah, and Mika, Satomi. "DIY Wearable technology". In *ISEA 15th International Symposium on Electronic Art*, 2009.

[65] Meier, Urs. "Carbon fiber-reinforced polymers: modern materials in bridge engineering". *Structural engineering international* 2, no.1 (1992): 7–12.

[66] Barbadillo, Guillermo, K, Dautenhahn, and Luke, Wood. "Using FSR sensors to provide tactile skin to the humanoid robot KASPAR". University of Hertfordshire, 2011.

[67] Duhamel, Pierre-Emile J, Castor O, Perez-Arancibia, Geoffrey L, Barrows, and Robert J, Wood. "Biologically inspired optical-flow sensing for altitude control of flapping-wing microrobots". *IEEE/ASME Transactions on Mechatronics* 18, no.2 (2012): 556–568.

[68] Lian, Kuang-Yow, Sung-Jung, Hsiao, and Wen-Tsai, Sung. "Intelligent multi-sensor control system based on innovative technology integration via ZigBee and Wi-Fi networks". *Journal of network and computer applications* 36, no.2 (2013): 756–767.

[69] Saxena, RS, RK, Bhan, and A, Aggrawal. "Reducing readout complexity of large resistive sensor arrays". *IEEE Sensors Journal* 8, no.11 (2008): 1862–1863.

[70] Zumbrunn, Thomas, Bruce A, MacWilliams, and Barbara A, Johnson. "Evaluation of a single leg stance balance test in children". *Gait & posture* 34, no.2 (2011): 174–177.

[71] Gray, Vicki L, Tanya D, Ivanova, and S Jayne, Garland. "Reliability of center of pressure measures within and between sessions in individuals post-stroke and healthy controls". *Gait & posture* 40, no.1 (2014): 198–203.

[72] Schmit, Jennifer M, Michael A, Riley, Arif, Dalvi, Alok, Sahay, Paula K, Shear, Kevin D, Shockley, and Raymund YK, Pun. "Deterministic center of pressure patterns characterize postural instability in Parkinson's disease". *Experimental brain research* 168, no.3 (2006): 357–367.

[73] Dixit, Snehil, A, Maiya, and others. "Diabetic peripheral neuropathy and its evaluation in a clinical scenario: a review". *Journal of postgraduate medicine* 60, no.1 (2014): 33.

[74] Laroche, Davy, Alexandre, Kubicki, Paul J, Stapley, Vincent, Gremeaux, Katia, Mazalovic, J-F, Maillefert, and Paul, Ornetti. "Test–retest reliability and responsiveness of centre of pressure measurements in patients with hip osteoarthritis". *Osteoarthritis and cartilage* 23, no.8 (2015): 1357–1366.

[75] Buckley, John G, Dan, O'Driscoll, and Simon J, Bennett. "Postural sway and active balance performance in highly active lower-limb amputees". *American journal of physical medicine & rehabilitation* 81, no.1 (2002): 13–20.

[76] Dillon, Michael P, Stefania, Fatone, and Andrew H, Hansen. "Effect of prosthetic design on center of pressure excursion in partial foot prostheses". *Journal of Rehabilitation Research & Development* 48, no.2 (2011).

[77] Bartlett, Roger, Jon, Wheat, and Matthew, Robins. "Is movement variability important for sports biomechanists?". *Sports biomechanics* 6, no.2 (2007): 224–243.

[78] Dandekar, Kiran, Balasundar I, Raju, and Mandayam A, Srinivasan. "3-D finite-element models of human and monkey fingertips to investigate the mechanics of tactile sense". *J. Biomech. Eng.* 125, no.5 (2003): 682–691.

[79] Parhi, Pekka, Amy K, Karlson, and Benjamin B, Bederson. "Target size study for one-handed thumb use on small touchscreen devices". In *Proceedings of the 8th conference on Human-computer interaction with mobile devices and services* (pp. 203–210), 2006.

[80] Asakawa, Deanna S, George H, Crocker, Adam, Schmaltz, and Devin L, Jindrich. "Fingertip forces and completion time for index finger and thumb touchscreen gestures". *Journal of Electromyography and Kinesiology* (2017) 6-13.

[81] Bentley, Jon. "Programming pearls: algorithm design techniques". *Communications of the ACM* 27, no.9 (1984): 865–873.

[82] Gries, David. "A note on a standard strategy for developing loop invariants and loops". *Science of Computer Programming* 2, no.3 (1982): 207–214.

[83] Alves, Carlos ER, Edson N, Caceres, and Siang W, Song. "BSP/CGM algorithms for maximum subsequence and maximum subarray". In *European Parallel Virtual Machine/Message Passing Interface Users' Group Meeting* (pp. 139–146), 2004.

[84] Aghajan, Hamid Karbalai. *Subspace techniques for image understanding and computer vision*. Stanford University, 1995.

[85] Kim, Jong-Seok, Dae-Yong, Kwon, and Byong-Deok, Choi. "High-accuracy, compact scanning method and circuit for resistive sensor arrays". *Sensors* 16, no.2 (2016): 155.

[86] Lopez, José A Hidalgo, Oscar, Oballe-Peinado, and José A, Sánchez-Durán. "A proposal to eliminate the impact of crosstalk on resistive sensor array readouts". *IEEE Sensors Journal* 20, no.22 (2020): 13461–13470.

[87] Manapongpun, Pattawut, and Dahmmaet, Bunnjaweht. "An Enhanced Measurement Circuit for Piezoresistive Pressure Sensor Array". In *2020 17th International Conference on Electrical Engineering/Electronics, Computer, Telecommunications and Information Technology (ECTI-CON)* (pp. 105– 108), 2020.

[88] Medrano-Sanchez, Carlos, Raul, Igual-Catalán, Victor H, Rodriguez-Ontiveros, and Inmaculada, Plaza-Garcia. "Circuit analysis of matrix-like resistor networks for eliminating crosstalk in pressure sensitive mats". *IEEE Sensors Journal* 19, no.18 (2019): 8027–8036.

[89] Thom, Alexander. "A statistical examination of the megalithic sites in Britain". *Journal of the Royal Statistical Society. Series A (General)* 118, no.3 (1955): 275–295.

[90] Robinson, Stephen M. "Fitting spheres by the method of least squares". *Communications of the ACM* 4, no.11 (1961): 491.

[91] Cox, Maurice G, and Alistair B, Forbes. "Strategies for testing form assessment software", 1999.

[92] Coope, Ian D. "Circle fitting by linear and nonlinear least squares". *Journal of Optimization theory and applications* 76, no.2 (1993): 381–388.

[93] TN0074 Technical note, STM. Calibration procedure for a resistive touchscreen system based on the STMPE811.

[94] Tekscan. How Does a Force Sensing Resistor (FSR) Work? https://www.tekscan.com/blog/flexiforce/how-does-force-sensing-resistor-fsr-work

[95] Interlink Electronics. FSR 400 Series Data Sheet. https://files.seeedstudio.com/wiki/GroveRound_Force_Sensor_FSR402/res/FSR402.pdf

APPENDICES

APPENDIX A

SENSOR ARDUINO CODE

```
#define numRows 5
#define numCols 5
#define sensorPoints numRows*numCols
#include<SPI.h>
int rows[] = {A0, A2, A4, A6, A8};
int cols[] = {23, 27 ,31, 35, 39};
int incomingValues[sensorPoints] = {};

void setup() {
Serial.begin(9600);
 // set all rows and columns to INPUT (high impedance):
  for (int i = 0; i < numRows; i++) {
    pinMode(rows[i], INPUT);}
  for (int i = 0; i < numCols; i++) {
    pinMode(cols[i], INPUT);}
}

 void loop() {
   for (int colCount = 0; colCount < numCols; colCount++) {
      pinMode(cols[colCount], OUTPUT); // set as OUTPUT
      digitalWrite(cols[colCount], HIGH); // set HIGH
      for (int rowCount = 0; rowCount < numRows; rowCount++) {
        incomingValues[colCount * numRows + rowCount] = analogRead(rows[rowCount]); // read INPUT
        }// end rowCount
      pinMode(cols[colCount], INPUT); // set back to INPUT
   }// end colCount
   // Print the incoming values of the grid
   for (int i = 0; i < sensorPoints; i++) {
     Serial.print(incomingValues[i]);
     if (i < sensorPoints - 1) Serial.print("\t");
   }
   Serial.println();
   delay(10);
 }
```

APPENDIX B

TECHNICAL DRAWINGS OF TEST WEIGHTS

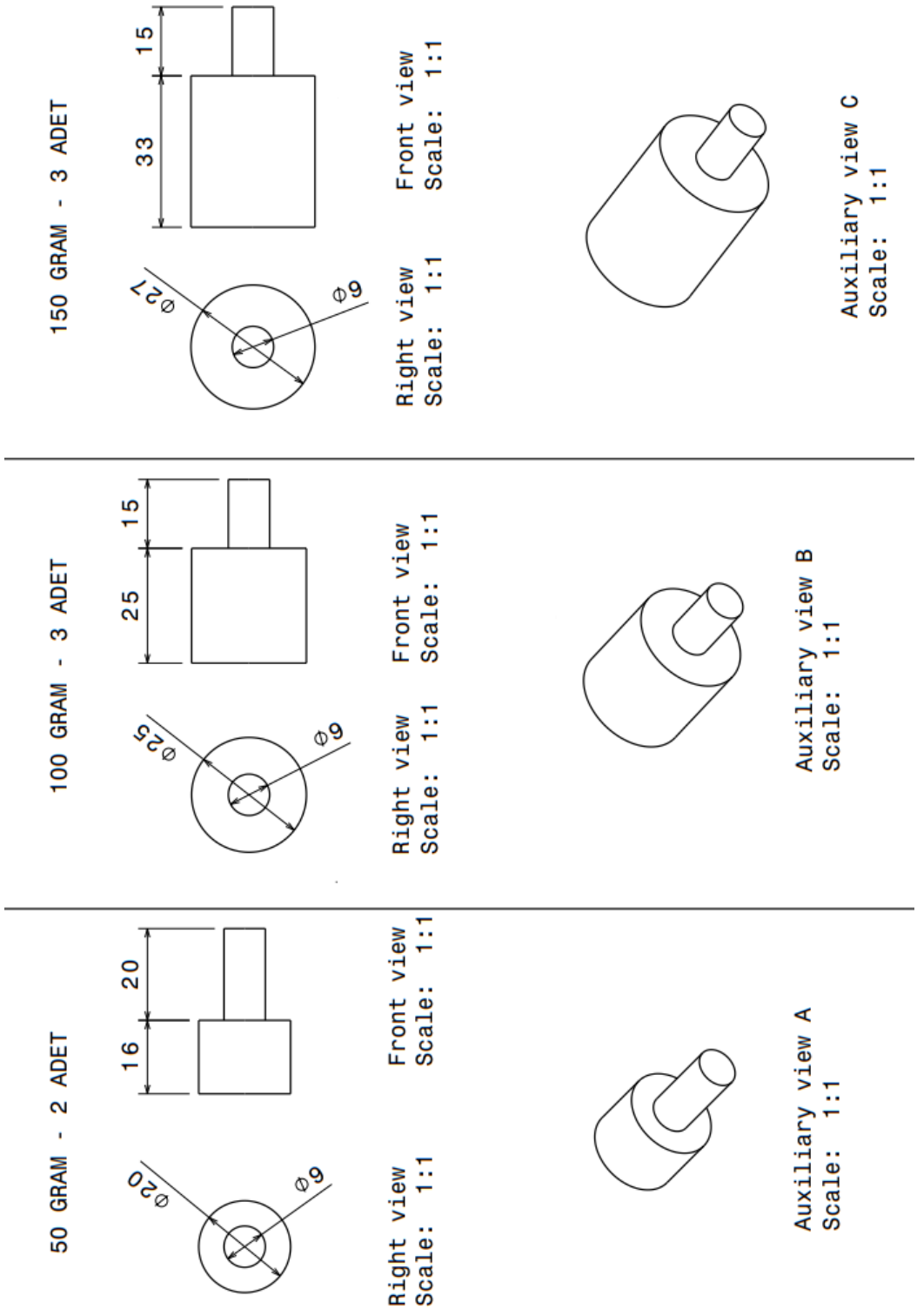

APPENDIX C

TECHNICAL DRAWINGS OF SENSORS

5x5 (25 SENSELS)

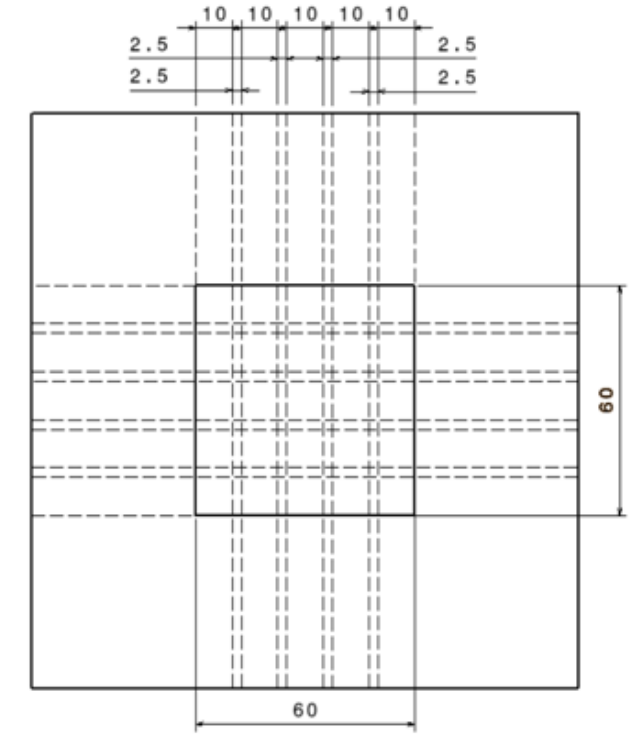

7x7 (49 SENSELS)

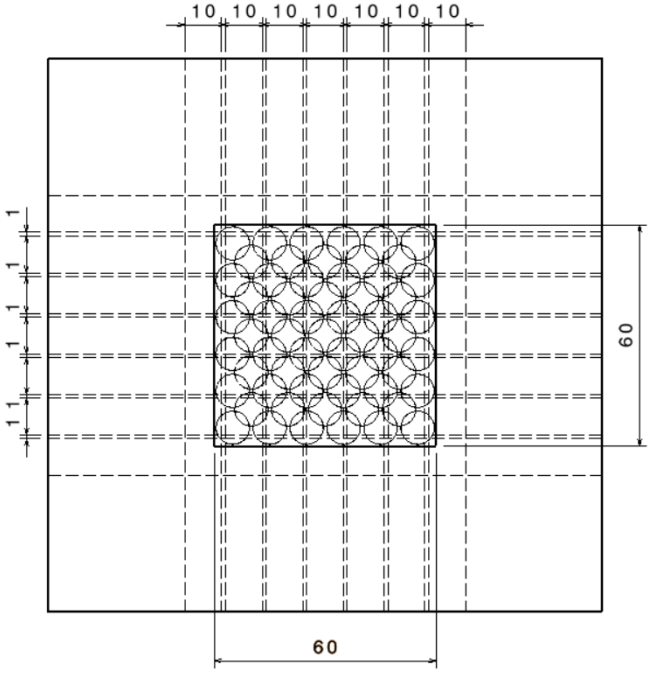

APPENDIX D

COORDINATES OF THE 61 TEST POINTS

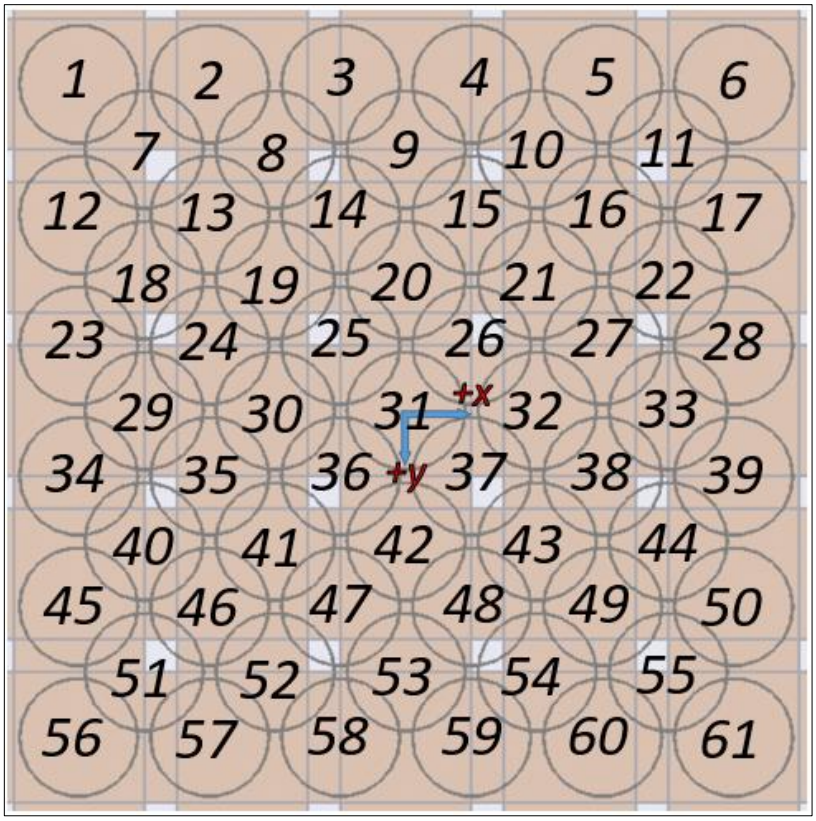

31: [0, 0], ORIGIN			
1: [-25, -25],	*16: [15, -15],*	*32: [10, 0],*	*47: [-5, 15],*
2: [-15, -25],	*17: [25, -15],*	*33: [20, 0],*	*48: [5, 15],*
3: [-5, -25],	*18: [-20, -10],*	*34: [-25, 5],*	*49: [15, 15],*
4: [5, -25],	*19: [-10, -10],*	*35: [-15, 5],*	*50: [25, 15],*
5: [15, -25],	*20: [0, -10],*	*36: [-5, 5],*	*51: [-20, 20],*
6: [25, -25],	*21: [10, -10],*	*37: [5, 5],*	*52: [-10, 20],*
7: [-20, -20],	*22: [20, -10],*	*38: [15, 5],*	*53: [0, 20],*
8: [-10, -20],	*23: [-25, -5],*	*39: [25, 5],*	*54: [10, 20],*
9: [0, -20],	*24: [-15, -5],*	*40: [-20, 10],*	*55: [20, 20],*
10: [10, -20],	*25: [-5, -5],*	*41: [-10, 10],*	*56: [-25, 25],*
11: [20, -20],	*26: [5, -5],*	*42: [0, 10],*	*57: [-15, 25],*
12: [-25, -15],	*27: [15, -5],*	*43: [10, 10],*	*58: [-5, 25],*
13: [-15, -15],	*28: [25, -5],*	*44: [20, 10],*	*59: [5, 25],*
14: [-5, -15],	*29: [-20, 0],*	*45: [-25, 15],*	*60: [15, 25],*
15: [5, -15],	*30: [-10, 0],*	*46: [-15, 15],*	*61: [25, 25],*

APPENDIX E

KADANE'S ALGORITHM IMPLEMENTATION

5x5 (25 SENSELS)

5x5 Raw Data

Sensel 1	Sensel 2	Sensel 3	Sensel 4	Sensel 5
Sensel 8	Sensel 9	Sensel 10	Sensel 11	Sensel 12
Sensel 15	Sensel 16	Sensel 17	Sensel 18	Sensel 19
Sensel 22	Sensel 23	Sensel 24	Sensel 25	Sensel 26
Sensel 29	Sensel 30	Sensel 31	Sensel 32	Sensel 33

25 sensel values are used

5x5 Max 2x2 Subarray

0	0	0	0	0
0	0	Sensel 10	Sensel 11	0
0	0	Sensel 17	Sensel 18	0
0	0	0	0	0
0	0	0	0	0

4 sensel values are used

5x5 Max 3x3 Subarray

0	0	0	0	0
0	Sensel 9	Sensel 10	Sensel 11	0
0	Sensel 16	Sensel 17	Sensel 18	0
0	Sensel 23	Sensel 24	Sensel 25	0
0	0	0	0	0

9 sensel values are used

7x7 (49 SENSELS)

7x7 Raw Data

Sensel 1	Sensel 2	Sensel 3	Sensel 4	Sensel 5	Sensel 6	Sensel 7
Sensel 8	Sensel 9	Sensel 10	Sensel 11	Sensel 12	Sensel 13	Sensel 14
Sensel 15	Sensel 16	Sensel 17	Sensel 18	Sensel 19	Sensel 20	Sensel 21
Sensel 22	Sensel 23	Sensel 24	Sensel 25	Sensel 26	Sensel 27	Sensel 28
Sensel 29	Sensel 30	Sensel 31	Sensel 32	Sensel 33	Sensel 34	Sensel 35
Sensel 36	Sensel 37	Sensel 38	Sensel 39	Sensel 40	Sensel 41	Sensel 42
Sensel 43	Sensel 44	Sensel 45	Sensel 46	Sensel 47	Sensel 48	Sensel 49

49 sensel values are used

7x7 Max 2x2 Subarray

0	0	0	0	0	0	0
0	0	0	0	0	0	0
0	0	0	Sensel 18	Sensel 19	0	0
0	0	0	Sensel 25	Sensel 26	0	0
0	0	0	0	0	0	0
0	0	0	0	0	0	0
0	0	0	0	0	0	0

4 sensel values are used

7x7 Max 3x3 Subarray

0	0	0	0	0	0	0
0	0	0	Sensel 11	Sensel 12	Sensel 13	0
0	0	0	Sensel 18	Sensel 19	Sensel 20	0
0	0	0	Sensel 25	Sensel 26	Sensel 27	0
0	0	0	0	0	0	0
0	0	0	0	0	0	0
0	0	0	0	0	0	0

9 sensel values are used